8-2022

Understanding Liquid Dynamics using the Van Hove function from Inelastic Neutron Scattering Measurements

Yadu Krishnan Sarathchandran
ysarathc@vols.utk.edu

To the Graduate Council:

I am submitting herewith a dissertation written by Yadu Krishnan Sarathchandran entitled "Understanding Liquid Dynamics using the Van Hove function from Inelastic Neutron Scattering Measurements." I have examined the final electronic copy of this dissertation for form and content and recommend that it be accepted in partial fulfillment of the requirements for the degree of Doctor of Philosophy, with a major in Physics.

Dr. Takeshi Egami, Major Professor

We have read this dissertation and recommend its acceptance:

Dr. Michael Fitzsimmons, Dr. Steven Johnston, Dr. Cristian Batista, Dr. Thomas Papenbrock

Accepted for the Council:

Dixie L. Thompson

Vice Provost and Dean of the Graduate School

(Original signatures are on file with official student records.)

Understanding Liquid Dynamics using the Van Hove function from Inelastic Neutron Scattering Measurements

A Dissertation Presented for the

Doctor of Philosophy

Degree

The University of Tennessee, Knoxville

Yadu Krishnan Sarathchandran

August 2022

DEDICATION

To my father, who nurtured my interest in science. To my mother for teaching me how to be kind to others and to myself. To my sister for always having belief in me. To my wife for her unconditional support. To my grandparents, two of whom passed away while I was continents away during the last two years, for their love.

ACKNOWLEDGEMENTS

I have received a great deal of support and assistance throughout my dissertation research. I would first like to thank my research supervisor, Prof. Takeshi Egami, whose contribution was invaluable in formulating my Ph.D. research. Thank you for your unwavering support and constant motivation, and above all, for being kind and considerate to me throughout the time we worked together. Prof. Egami provided invaluable guidance and feedback to help me carry out my research projects. I have found myself entering his office countless times seeking help and left buoyed and motivated by his words of wisdom to solve challenging problems in research and in my personal life. I admire how effortlessly he explains complex concepts to people, while being kind and respectful. I would like to thank Dr. Yuya Shinohara and Dr. Wojciech Dmowski for their mentorship, which helped me persevere and accomplish my research objectives. I thank Yuya for strengthening my data analysis and programming ability, which has opened new avenues of opportunities in my professional life. I would like to thank my committee members, Dr. Michael Fitzsimmons, Dr. Steven Johnston, Dr. Cristian Batista, and Dr. Thomas Papenbrock, for their time and feedback, which helped me structure my PhD research and improve my communication skills.

I would like to extend my gratitude to my current and former group members, and collaborators, Dr. Zengquan Wang, Dr. Hui Wang, Mr. Leo Zella, Dr. Chae Woo Ryu, Dr. Jaeyun Moon, Dr. Eva Zarkadoula, Dr. Douglas Abernathy, Dr. Takuya Iwashita, Dr. Eugene Mamontov, and Dr. Daniel Pajerowski, without whom my research would not have been possible, for their assistance and encouragement.

Finally, I could not have completed this dissertation without the love and support of my wife, Dr. Anu Thomas. I would also like to thank my friends Jerome Kovoor, Dony Varghese, Rakesh Kamath, Hasitha Suriya-Arachchige, and Rahul Soni for being an integral part of my life in Knoxville.

ABSTRACT

Liquid state physics remains relatively unexplored compared to solid-state physics, which achieved massive progress over the last century. The theoretical and experimental methodologies used in solid-state physics are not suitable to study the liquid state due to the latter's strong time dependence and the lack of periodicity in structure. The approaches based on phonon dynamics break down when phonons are over-damped and localized in liquids. The microscopic nature of atomic dynamics and many-body interactions leading to liquid state properties such as viscosity and dielectric loss in liquids remain unclear. Inelastic neutron scattering measurements were done to study the microscopic origins of the above phenomena on two liquid state systems, water and gallium, with the atomic dynamics explored in real-space and time utilizing the Van Hove function, *G(r,t)*. Molecular Dynamics (MD) simulations were implemented to explain the experimental observations.

The Local Configurational Excitation (LCE) is the fundamental excitation that changes the topology of local connectivity in liquids. The life-time of LCE (τ_{LC}) is defined as the time it takes for an atom to lose or gain a neighbor. It was proposed through MD simulations, and later verified through neutron scattering measurements that the LCE's are the microscopic origin of viscosity in metallic liquids at high temperatures. Generalizing this study to different types of liquids is essential to obtain a universal dynamical behavior of liquids. Towards that goal, we studied the correlated dynamics of a partly covalent liquid, gallium. We show that it is possible to achieve a universal behavior for simple metallic liquids and partially covalent liquid metals.

The high dielectric loss in water is one of the anomalous properties of water. The microscopic molecular mechanism leading to this property remains unclear despite decades of research. By determining the Van Hove function of water from inelastic neutron scattering measurements, we show that the origin of the high dielectric loss is a collective reorientation of water molecules and cooperative proton tunneling involving several water molecules. The results contradict the widely held beliefs that the dielectric relaxation mechanism in water involves the rotation of a single molecule and is purely diffusive in origin.

TABLE OF CONTENTS

LIST OF TABLES

LIST OF FIGURES

CHAPTER 1 INTRODUCTION

The liquid state is one of the three fundamental states of matter, intermediate between gaseous state and solid state. Liquids along with glasses, which are generally considered as liquids frozen in time, are strongly disordered matter. In fact they are the most dominant form of matter that exist on earth. These amorphous materials are characterized by their atomic arrangement with no long-range periodicity. Liquid state materials are ubiquitous on our planet and they have played a key role in our society's cultural and industrial progress. Humanity's use of glasses dates back to the stone age when they were used as tools and weapons, as well as valuables such as gemstones. The glassmaking technique dates back approximately 3600 years, long before humans learned to make iron tools.[8] Throughout human history, liquids and glasses have also played a vital role in the advances of art and architecture. During the early civilizations, they were used for agricultural and transportation needs, then gained industrial importance later with the advent of steam engine, hydraulic systems, and measuring devices. Given all this, it is peculiar that liquid state physics remains relatively unexplored compared to solid state physics, which achieved tremendous advances over the last century. The majority of materials on earth are amorphous in structure, but the physics of amorphous systems significantly lags behind the physics of crystalline materials. What is the origin of this disparity? The lack of periodicity in liquids is a striking reason why it is challenging to understand the liquid state phenomena. In contrast to crystalline materials, where periodicity largely simplifies the many-body problem, liquid state systems are innately disordered. Furthermore, the highly dynamic nature of its structure along with the inherent

disorder makes the first-principle studies of liquids cumbersome. The liquid state possesses a *marginal* character that arises from a delicate balance between the packing of molecules and the cohesive forces. The existence of a *small parameter* in solids and gases greatly simplifies the theoretical modeling of those systems.[9] For gases, the many-body interactions are the *small parameter,* because their energy contribution is negligible compared to the enormous kinetic energy contribution from the diffusion of molecules. For solids, the diffusion of atoms is the *small parameter*, which is suppressed by the strong many-body interactions that result in only collective dynamics known as phonons. The liquid state does not have a *small parameter* because neither many-body interactions nor the diffusion dominates the structure and dynamics of liquids alone. This makes liquids fascinating, yet at the same time, extremely challenging to understand. For many years, researchers thought the lack of a long-range order made liquids uninteresting. However, note that the complexity that arises from competing forces has been utilized in technological innovations quite often. Small perturbations in external parameters induce great changes in the system's behavior in these systems. Most materials prevalently used today in industrial and technological applications have disorder generated in them for efficiency - for example in the soft matter and polymer industry, the interplay between order and disorder is used in the development of new, high-performance materials. The semiconductor industry relies on doping silicon to create n-type and p-type semiconductors to modulate its electrical and optical properties. Thus, the deviations from periodicity and disorder characterize the properties of most complex and sophisticated materials. Studying the physics of liquid state also helps us understand the true-nature of emergent phenomena,

which are the hallmarks of many-body systems. In the early 1960s, some physicists began to call the field "condensed-matter physics", instead of "solid state physics" due to their increasing interest in the field of soft matter and the quantum many-body problem. They initiated the unification of the research done in solid and liquid states under the umbrella field, "Condensed Matter Physics", which signified the growing interest in disordered systems, including liquids.[10]

While liquid state research pales in comparison to solid state research, there is a plethora of rich and dense works that have uncovered fundamental insights regarding many liquid state behaviors, starting with the theoretical and computational studies on critical phenomena, phase-transitions, and nonlinear dynamics of fluid systems in early 1940s.[9, 11-13] A brief first-person review of which can be found from David Chandler's autobiographical account of the 1967 Gordon Research Conference on the Physics and Chemistry of Liquids.[14] The behavior of liquids at high temperature was assumed to be similar to the free diffusion of atoms in gases. However, unlike gases, the atoms in liquids are strongly bound by cohesive forces, and they have similar density as solids. This would suggest a strongly correlated behavior in their dynamics. One of the fundamental properties of a liquid is its viscosity, the atomic origin of which remains debated to this day. The temperature-dependent changes in viscosity of a liquid is an ill-understood problem. Austen Angell described a graphical method to compare the changes in viscosity of a variety of liquids in his seminal work in 1995.[2] This allowed the behaviors of glass-forming liquids to be compared. This initiated the categorization of liquids to two broad classes based on their viscous behavior. The "strong liquids" that nearly follow the Arrhenius

behavior of viscosity to “fragile liquids”, which exhibit a strong non-Arrhenius behavior upon cooling towards the glass transition temperature. Glass transition is the process in which a viscous liquid undergoes a continuous transition into the amorphous solid state during cooling. The Angell plot is shown in **Figure 1.1**, in which the logarithm of shear viscosity is plotted against the scaled inverse temperature, *Tg/T* (where *Tg* is the glass transition temperature). A parameter called fragility (*m),* which is defined as,

$$m = \frac{\partial(log\ \eta)}{\partial(T_g/T)}\bigg|_{T=T_g},$$

determines the extent to which a liquid deviates from the Arrhenius behavior of viscosity. Higher the value of *‘m’* the more fragile the liquid is. Strong network forming liquids such as Silica belong to the “strong liquids”, whereas some molecular liquids such as O-terphenyl belong to the fragile liquids category. Most metallic liquids are fragile, where the viscosity follows an Arrhenius behavior at high temperatures, but transition to a super-Arrhenius behavior when cooled below a temperature known as the crossover temperature. The microscopic mechanism leading to this crossover behavior of viscosity remains unclear.

It was observed that the heat capacities of metallic liquids approximately satisfied Dulong-Petit's law of specific heat capacity at high temperatures. Theories based on phonon dynamics could not explain this behavior because the life-time of atomic dynamics was shorter than the phonon life-time at high temperatures, making phonons overdamped and marginalized in liquids. The atoms in liquids are under constant motion, hence changes in the local topology are inevitable. An elementary excitation called Local Configurational

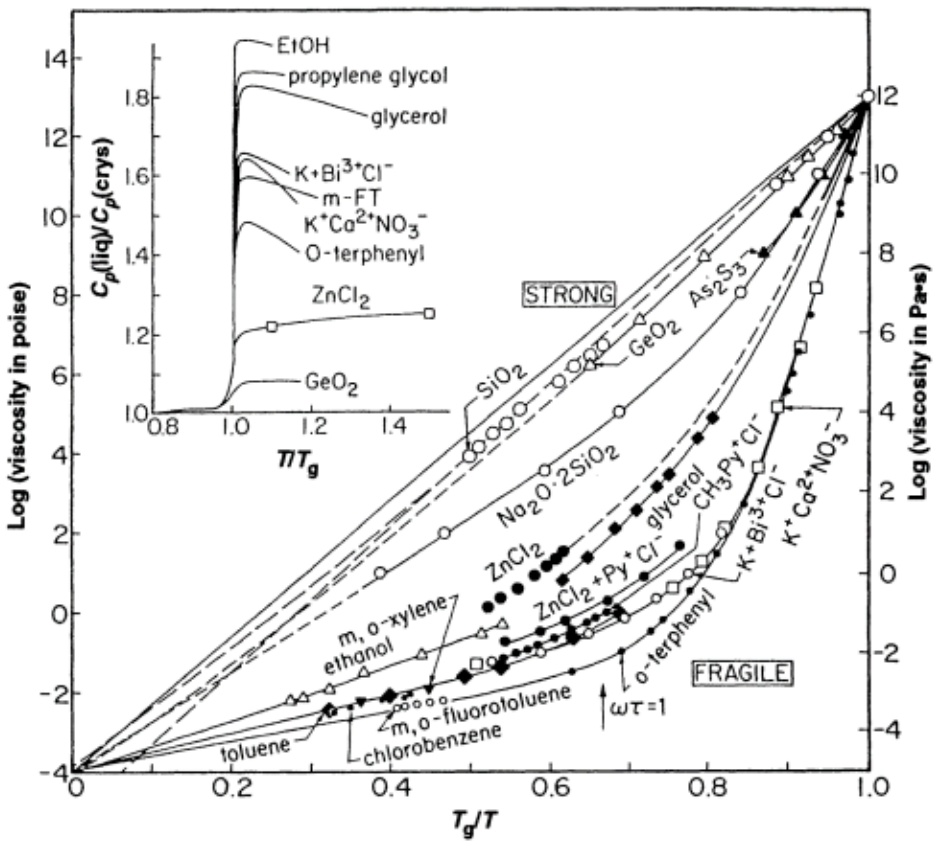

Figure 1.1 The Angell plot of viscosity shown for a variety of liquids. The strong to fragile pattern of liquid behavior on which liquids are classified is shown. [2]

Excitation (LCE) was proposed to explain the origin of viscosity in metallic liquids at high-temperatures.[3] LCE embodies the characteristic nature of liquid state where bond formation and breakages occur quite frequently. It is defined as the process of losing or gaining a neighbor, thereby changing the atomic connectivity or local topology of the liquid. The relaxation time of this new excitation, which is a microscopic quantity, was found to be approximately equal to the macroscopic Maxwell relaxation time, which is defined as the time-scale of viscosity, in simple metallic systems at high temperatures. This is a fascinating observation, strongly supporting the claim that LCE is the elementary excitation in high-temperature metallic liquids.[3] Below a particular temperature, T_A, this equality breaks down, which coincides with a clear deviation from the Arrhenius behavior of viscosity, the crossover phenomenon, as shown in **Figure 1.2**. It is suspected that the crossover occurs because the LCE's were independent of each other at high temperature (above), but begin to interact with each other to form a long-range elastic stress-field below. It is also speculated that upon cooling below, the lifetime of atomic dynamics exceeds the phonon life-time, resulting in a competition between phonons and LCEs, ultimately culminating in glass transition. A connection was established between stress-resolved pair-correlation functions and stress-correlations in a model monoatomic liquid using classical MD simulations[15]. Some results on the nature of elastic stress field due to deformation in solids[16] predicted by Eshelby in 1957 were reproduced using the new approach, suggesting the feasibility of connecting the two states of matter. The suspected origin of the crossover phenomenon is the temperature-dependent competition between phonons and LCEs.[3] Generalizing the crossover behavior observed in high temperature

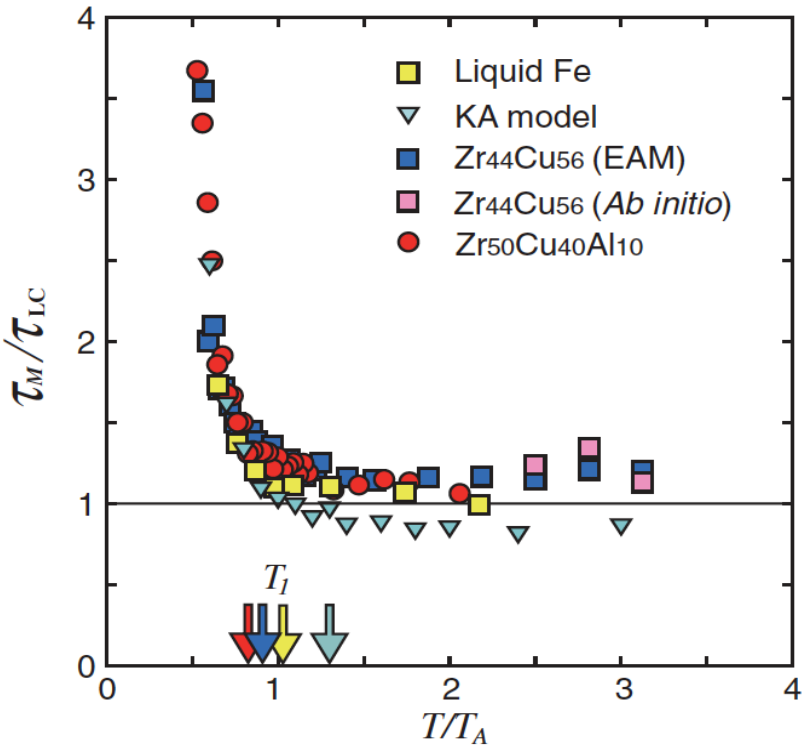

Figure 1.2 The ratio of the relaxation times ($\boldsymbol{\tau_M/\tau_{LC}}$) of metallic liquids plotted against scaled temperature (T/T_A). [3]

metallic liquids to other types of liquids is required to formulate a universal microscopic understanding of liquids.

Although structure and dynamics in various liquid systems have been studied using diffraction and spectroscopic techniques, correlation studies both in time and space together have rarely been done. The direct experimental observations of atomic dynamics in liquids were scarce, and mostly carried out to study diffusion or the self-motion of atoms in a liquid using quasi-elastic, incoherent scattering. Studying the correlated atomic motion requires the use of coherent scattering techniques, which is starting to grow in popularity over the last decade.[17] The powerful technique of time-delayed pair-correlation functions help us combine the spatial and temporal correlations in liquids to give valuable information on their underlying physics. The advent of powerful synchrotron and neutron scattering facilities combined with the above technique can give valuable information on the atomistic mechanisms behind many fascinating properties of liquids.[18]

The primary focus of my Ph.D. dissertation is to study the microscopic mechanisms behind a few captivating structural and dynamical behaviors of two liquid state systems, water and gallium. Water covers approximately 70% of earth's surface and constitutes more than 60% of the human body. The origin of life on earth is fundamentally tied to the presence of water on earth. Despite being the most common liquid, water remains a mystery to researchers in all disciplines of science. It exhibits many anomalous behaviors which are thought to be tied to the presence of a strong hydrogen bond network present in it. Although, the precise mechanisms that gives rise to those properties and make water a unique liquid are not yet completely understood. I specifically focus on one of water's

anomalous properties, the high dielectric loss. The microscopic mechanism behind the dielectric loss is highly debated among researchers. By performing neutron inelastic scattering, a microscopic measurement, I plan to elucidate the mystery of dielectric loss in water. Studying water is also key in unravelling the true nature of hydrogen bond, which is widely believed to be the reason behind the anomalous properties of water. Hydrogen bonds play a significant role in biological systems such as proteins and DNA by facilitating their secondary and tertiary structures. Gallium is an important material in the electronics industry, mainly in its compound forms such as Gallium Arsenide (*GaAs*) and Gallium Nitride (*GaN*) in semi-conductor circuits and diodes. Other than having a very low melting point (303 K), it also possesses higher density in liquid state than in the stable solid state, similar to the behavior exhibited by water and silicon. Gallium exhibits an anomalous change in diffusivity as a function of temperature, similar to the behaviors observed in water. The presence of residual covalent dimers have been observed near the melting point,[19] pointing to the mixed nature of atomic bonding in the liquid state.[20]

I utilized the inelastic neutron scattering techniques and the time-dependent pair-correlation functions to study the atomistic mechanisms in two liquid systems in my research, water and gallium. This research would result in a better understanding of the microscopic behavior of liquids, in general. The theory, experimental methods, and computational techniques will be discussed in the next chapter.

CHAPTER 2 THE THEORY & EXPERIMENTAL METHODS

Overview of the Methods

Traditionally, the structure and dynamics of liquid systems are investigated using diffraction and spectroscopy, respectively. Diffraction of a liquid sample provides the 'snapshot' structure of the liquid, which is encoded in the output of diffraction measurement called the structure factor, *S(Q)*. The structure factor is a function of Q (momentum transfer), and is independent of E (energy transfer) as the diffraction measurements are low energy-resolution scattering measurements which integrate the energy transfer. For a crystalline sample, *S(Q)* consists of sharp Bragg peaks representative of different crystal planes, which are interpreted in a straightforward manner. This is not the case with liquids and other amorphous materials. Due to the lack of long-range structural order, *S(Q)* of liquids consists of short, diffused peaks. Therefore, the crystallographic interpretation does not have any meaning. Thus, the structure of liquids and other disordered systems are studied using the pair distribution function, *g(r)*, which is estimated from *S(Q)* by Fourier transforming the data from Q-space to the real-space. Pair distribution function is the dominant technique used in the investigation of the structure of liquids from diffraction technique. In practice, the Fourier transformation is a tricky process. The accurate estimation of the pair distribution function requires obtaining the *S(Q)* over a large accessible Q-range, preferably over 20 Å^{-1}. This is important to avoid the termination errors that arise from the Fourier transformation due to the finite Q-range available from experiments. It is possible to obtain the scattering data over a wide Q-range using high-energy X-Ray Diffraction (XRD) and neutron diffraction techniques using large 2D detectors and linear-position sensitive detectors as they cover large solid angles.

Liquid Dynamics

Liquid dynamics is conventionally studied using spectroscopic measurements such as NMR, Raman and infrared spectroscopy.[21-23] These spectroscopic measurements yield the characteristic time-scales of the different excitations in the system. By tuning the frequency range of the measurement, electronic, vibrational or molecular-level excitations can be probed. These measurements are macroscopic by design as they the lack spatial resolution to provide microscopic-level information regarding the mechanisms giving rise to these excitations. Understanding the atomic-level mechanisms and the ensuing dynamics deserves more attention in the research of liquid systems. In the last decade, inelastic, quasi-elastic, and spin echo techniques have become mainstream to study liquid dynamics by adding a spatial dimension to the information collected. All of these techniques provide the dynamical information in the reciprocal space. In the first two methods, the dynamic structure *S(Q,E)* is factor is measured, but neutron spin-echo measurement outputs the dynamical information in the *Q*-*t* space, in the form of a function called the intermediate scattering function, *F(Q, t)*. Despite the additional spatial information collected in the dynamical studies, the interpretation of the physics of liquids from these techniques is not straightforward due to the analyses being carried out in the *Q*-space. The transformation of the inelastic scattering data to the real-space is a significant challenge due to the experimental limitation of obtaining the *S(Q,E)* over a wide range of momentum energy transfers with sufficient energy resolution required for studying dynamics. Neutron scattering is a signal-limited technique, therefore designing an experiment with a higher *Q*-range would limit the energy resolution. This is an important consideration while designing

experiments to obtain the *S(Q,E)* data. The detector coverage and the resolution needs to be tailored for each measurement depending on the relevant length-scale and time-scale of the phenomena. The urgent need of real-space transformation in our investigation of liquid dynamics necessitates the use of wide Q-range, which puts a major constraint on the selection of neutron spectrometers capable of providing excellent resolution and good statistics of measurement. The Van Hove function is then estimated to understand the correlated atomic dynamics in liquids in real-space.

Theory of Inelastic Neutron Scattering

Scattering techniques provide the most convenient methods for obtaining quantitative information on composition, structure, and dynamics of materials. They are based on interactions between incident particles (we primarily focus on neutrons, but x-rays and other radiation follow the same principles) and the atoms in the target system. The scattered intensity of the probing beam after hitting the sample is obtained as a function of the scattered angle, and the energy exchanged during the event. For understanding structure and dynamics of systems, the probing radiation should have wavelengths comparable to the inter-atomic lengths of the sample. The foundation of scattering technique is the Bragg's law:

$$2d\ sin\,\theta = n\,\lambda\ ,$$

where θ is the scattering angle, d is the inter-atomic spacing, , λ is the wavelength of the incident radiation and n is a positive integer. Bragg diffraction occurs when a radiation is scattered by the system and undergoes constructive interference. The Bragg's law provides

the path difference between the waves undergoing diffraction by connecting the inter-atomic spaces in the sample and the scattering angles. For crystals, the detected spectrum will have a series of sharp-peaks known as Bragg peaks. This is due to the ordered packing structure of crystals. For disordered or dynamic systems, the observed spectrum will have broader peaks, generally called diffuse scattering, due to disorder and motion of atoms inside the sample. Scattering techniques are broadly divided into two known as elastic and inelastic scattering. When the state of the system remain the same after scattering, the process is called elastic scattering. In elastic scattering, the dynamical information is lost and only the averaged structure remains in the collected data. For inelastic scattering, the state changes after getting scattered by the radiation, and the energy of the radiation gets transferred to the system or vice versa. The exchanged energies and momentum information is used to collect the structural and dynamical information of the target sample, as the corresponding Fourier components are the real-time and real-space. This makes this method ideal for our purpose of studying the correlated dynamics.

Consider a collision experiment where the number of scattered particles measured by a detector through a solid angle per unit time with the final energy between E' and $E' + dE'$ is $N d\Omega\, dE'$. The scattering occurs through in a particular direction (θ, ϕ). The number of scattered particles is directly proportional to the incident flux of particles (Φ) defined as the number of particles crossing a unit area perpendicular to the direction of incidence per unit time. If we are not interested in resolving the energies of the scattered particles, but simply want all the particles that scattered, the corresponding cross-section is called differential cross-section, The partial-differential cross section is written as.

$$\frac{d^2\sigma}{d\Omega dE'} = \frac{N}{\Phi}$$

The differential cross section is estimated by summing over all the energies of the scattered particles,

$$\frac{d\sigma}{d\Omega} = \int_0^\infty \frac{d^2\sigma}{d\Omega dE'} dE'$$

The total cross section is obtained from the differential cross-section by integrating caross the solid angles,

$$\sigma = \int \frac{d\sigma}{d\Omega} d\Omega = \int_0^{2\pi} d\phi \int_0^\pi d\theta \, sin\,\theta \frac{d\sigma}{d\Omega}$$

Let $\hbar\boldsymbol{k}'$ and $\hbar\boldsymbol{k}''$ denote the incident and scattered waves involved in the scattering process. For neutrons, the interaction occurs with the nuclei and for x-rays with the electron cloud of the atoms in the material. The transferred momentum is given as,

$$\hbar\boldsymbol{Q} = \hbar\boldsymbol{k}' - \hbar\boldsymbol{k}''.$$

If the scattering is elastic, the magnitude of momentum doesn't change, thus giving $|\boldsymbol{Q}| = 2|\boldsymbol{k}'|\sin(\theta/2)$. Given that there's minimum coupling between the incident particle and the system, the rate of transmission from one state, $|\boldsymbol{k}'\rangle$ to another $|\boldsymbol{k}''\rangle$, is given by the Fermi's golden rule in quantum mechanics. Let V be the potential of the interaction between the scattering particle and the sample, the differential cross-section per solid angle is given by:

$$\frac{d\sigma}{d\Omega} \sim |\langle \boldsymbol{k}'|V|\mathbf{k}''\rangle|^2$$

The expression for interaction potential, V, summed over all atoms in the material is:

$$V(r) = \sum_{i=1}^{N} V(r - r_i).$$

Using the expression of the potential in the differential cross-section, we ultimately obtain

$$\frac{d\sigma}{d\Omega} \sim |V(\boldsymbol{Q})|^2 \langle \rho_{\boldsymbol{Q}}\, \rho_{-\boldsymbol{Q}} \rangle \sim N|V(\boldsymbol{Q})|^2 S(\boldsymbol{Q}).$$

The expression on the R.H.S. includes the structure factor, $S(\boldsymbol{Q})$, which is the correlation function of the Fourier component of density fluctuations, $\rho_{\boldsymbol{Q}}$, with its complex conjugate. For neutrons, $|V(\boldsymbol{Q})|^2$ has no dependence on $\boldsymbol{Q}$ and is referred as the scattering length. For x-rays, $|V(\boldsymbol{Q})|^2$ depends on $\boldsymbol{Q}$ and is called the atomic form-factor of the material.

Scattering measurements can be further categorized into two different categories, called coherent and incoherent scattering. Coherence is usually used in science in relation to the phase matching of waves. The structural information of the material that underwent scattering comes from coherent part of the scattering, which correlates different particles at different times. Incoherent scattering provides information about the single particle dynamics (diffusive motion) or the time correlation between the same particle at different times. In our studies, we primarily focus on inelastic coherent scattering of neutrons.

The Van Hove function

In 1954, Leon Van Hove generalized the static pair-distribution function to a time-dependent function for a system of interacting particles[24]. He stated that under Born approximation, it is always possible to express the scattering cross-section in terms of a generalized pair-distribution function, $G(r, t)$, which is a function of r and a time-interval t. $G(r, t)$ is the averaged density distribution at a time $t' + t$ as observed from a point where a particle was found at time t' . for time $t = 0$, it reduces to the static pair distribution function, $g(r)$. In the case of neutron and x-ray scattering, this provides the comprehensive

analysis of the structure and dynamics of the system under consideration. From here on, we call the as the Van Hove function, defined as

$$G(r,t) = \frac{1}{4\pi\rho_0 N r^2} \left\langle \sum_{i,j}^{N} \delta\left(r - \left|\boldsymbol{r}_i(t) - \boldsymbol{r_j}(0)\right|\right) \right\rangle,$$

where *N* is the number of atoms in the system, $\boldsymbol{r}_i(t)$ is the position of the *i*-th atom at time *t*, ρ_0 is the average number density of atoms and $\langle \ldots \rangle$ denotes thermal and quantum averages. It is possible to separate the Van Hove function into two parts, considering our interest of studying single particle dynamics (diffusion) or dynamics of inter-particle correlations. Separating the above equation for $i = j$, and $i \neq j$:

$$G(r,t) = G_s(r,t) + G_d(r,t),$$

where $G_s(r,t)$ and $G_d(r,t)$ are the self (diffusion) and distinct (dynamical correlations) part of the Van Hove function. When $t \to 0$, they become as follows:

$$G_s(r, t=0) = \frac{1}{\rho}\delta(r)$$

$$G_d(r, t=0) = g(r),$$

G(r,t) is directly connected to the dynamic structure factor, *S(Q,E)*, through a double-Fourier transformation,

$$G(r,t\,) = \frac{1}{2\pi^2 \rho r} \int S(Q,E)\, e^{-iEt/\hbar}\, Q\, \sin(Qr)\, dQdE.$$

Despite this, its adoption in scientific circles had been rare. The primary reason for the scarce adoption of the Van Hove function was the practical difficulty of collecting inelastic scattering data over a wide momentum and energy transfer ranges, sufficient to apply the transformation to the real-space and time. In the past, Triple-Axis Spectrometry (TAS), which allows the determination of the energy transfer by analysis of the wavelength, were

used to collect *S(Q,E)*, famously by Brockhouse[25] in 1959 to study lead. In TAS, the neutrons are characterized before and after hitting the sample. These three processes (monochromatizating, sample interaction, and analyzing) make up the three axes of the triple-axis spectrometer. The collection of sufficient data using TAS took weeks or even months, which restricted the adoption of the Van Hove function in the scientific community. The advent of synchrotron radiation sources in France, USA and Japan in the late 1970's provided an opportunity to obtain high quality x-ray data from samples. Not until the arrival of the spallation neutron source in 2006 at the Oak Ridge National Laboratory, it was possible to measure the neutron Van Hove functions of materials. Thus most of the research using Van Hove function analysis were either carried out computationally, focusing primarily on the self-diffusive behaviors, or proof-of-concept experiments using TAS.

Molecular Dynamics Simulations

Molecular Dynamics (MD) simulation predicts how atoms in a molecular ensemble moves based on the forces exerted upon them via interactions between other atoms and/or an external field. MD simulations use pair-wise and many-body interatomic potentials to simulate molecular systems at a variety of thermodynamic conditions, such as temperature and pressure. The inter-atomic potentials (also called forcefields) are used to calculate the forces between particles and equilibrates by iteration of system energies. The pair potentials between atoms/molecules consists of a repulsion that materializes at short range which has its origin in the overlapping outer electron shells.[26] A short-range order is created by these strongly repulsive forces that characterizes the liquid state. Meanwhile the long-

range attractive forces changes gradually with the distance between particles, which gives rise to an attractive background that provides the cohesive energy required to stabilize the system.[26] The MD simulations are key to the study molecular systems because they estimate the coordinates and velocities of every atom at time, whereas experimental techniques are limited by instrumental bottlenecks to accomplish this task. The first MD simulations were performed in 1957 on simple gases using a hard sphere system by Alder and Wainwright.[27] A molecular dynamics simulation of a system of 864 particles interacting with a Lennard-Jones potential on a digital computer to simulate molecular dynamics in liquid argon was successfully carried out by Rahman.[28] This initiated a series of studies establishing the use of Lennard-Jones pair potentials as the more realistic model for rare gases compared to hard sphere systems used by Alder and Wainwright. The potential and the forces existing in a system of interacting particles are defined as:

$$\boldsymbol{F}_i = m_i \frac{d^2 \boldsymbol{r}_i}{dt^2} = -\boldsymbol{\nabla}_i V,$$

where $\boldsymbol{F}_i$ is the force acting on particle *i* of mass m_i, and *V* is the inter-atomic potential that describes the interaction between the particles. The total energy (initial state) of the system is estimated by summing over all particles in the system. The velocities of the particles are numerically computed by following Newton's equations of motion by fixing a finite MD timestep integration. New forces and positions are calculated at each timestep and the process is continued until the system reaches equilibrium based on the thermodynamic parameters or as many timesteps as we wanted. As the time integration method, the standard for microcanonical ensemble (NVE) is the velocity-Verlet integrator. Nose-Hoover integrators are used to obtain the canonical (NVT) and the isobaric-

isothermal (NPT) ensembles by constraining particle velocities (thermostat) and simulation box sizes (barostat), and thereby achieve the corresponding ensembles, respectively.

MD simulations are performed using the LAMMPS software package using either NVT or NPT ensembles. Unless otherwise specified, we assume periodic boundary conditions (PBC) for the simulations. There are numerous computational models for water.[29] Although, many of the most popular ones are successful in describing numerous features of water such as its anomalous variations in density, high specific heat capacity, and the high dielectric constant, these models fail to describe the dynamical behaviors.[30-33] Elucidating the dynamics of water is an essential step for a comprehensive understanding of the role of water in many biological systems. For water, the theoretical models used in this work are SPC/E[34] (Simple Point Charge Extended) for simulation of bulk water, and ReaxFF[35, 36] for the simulation of proton dissociation in a ring structure. Quantum MD (AIMD or Ab-initio MD) simulations were performed to study the dynamics in gallium by my collaborator J. Moon, because the self-diffusion and viscosity of gallium calculated from AIMD agreed with experimental measurements better than its classical counterpart, MEAM (Modified Embedded Atom Method). Details of the simulations will be elaborated on the following chapters.

Experimental Setup for Inelastic Scattering Measurements

Inelastic scattering is carried out at the Spallation Neutron Source (SNS), Oak Ridge National Laboratory (ORNL). SNS is equipped with over 20 modern neutron scattering spectrometers to study a variety of physical phenomena, ranging from measuring slow dynamics of polymers to measuring high-frequency phonons, and spanning a wide array

of fields such as physics, biology to 3D printed materials. As we learned in the previous chapter, inelastic neutron scattering has been conventionally performed using the triple-axis spectrometer at a reactor source, such as the HFIR (High Flux Isotope Reactor, ORNL). Collecting the dynamic structure factor spanning a wide range of energy and momentum transfers was a time-consuming and impractical process with this technique. The advent of the Spallation Neutron Source makes this feasible in a significantly shorter time-scale of hours or days. We primarily use the time-of-flight (TOF) method, which complements the TAS method. TOF instruments is ideal to explore large regions of Q-E space due to the large array of detectors collecting the neutrons over a wide range of scattered energy.[37] TOF methods were first implemented (then called velocity selectors) in 1935 to demonstrate that many of the slow neutrons belong to the thermal energy range by direct measurement.[38]

Inelastic Scattering Spectrometers at SNS

The TOF neutron spectrometers can be categorized into direct geometry spectrometers and indirect geometry spectrometers. For the direct geometry, the initial neutron energy is selected by a choppers/monochromators. For the inverted scattering geometry, the final energy of the scattered neutrons is chosen by the analyzer crystals. Backscattering is a technique where the inverted scattering geometry employs the energy analyzer crystals with a Bragg reflection angle near 90^0.[1] BASIS (Backscattering Silicon Spectrometer) is an indirect geometry spectrometer (BL-2) at the Spallation Neutron Source, which is primarily used for the measurement of quasi-elastic scattering. In regular time-of-flight neutron spectrometers, dynamics of the order of a few picoseconds are investigated. On the

other hand neutron spin echo measurements probe dynamics of the order of nanoseconds. The inelastic measurements done at BASIS can connect these two extremes dynamical regimes. The sample position is located in an external building about 84 m from the liquid H_2 moderator. A system of guides transport the beam to the sample position through a corridor that connects the BASIS building with the main target building.[1] Instead of using monochromators for the selection of incident energy, BASIS utilizes the time-of-flight technique for determining E_i. The available time range depends on a combination of the source repetition rate, the selection of choppers, and the neutron flight path. BASIS provides an energy resolution of ~ 3.5 μeV (FWHM at the elastic line) with an energy transfer range between -18 meV to 18 meV. However, the fine energy resolution is attained by sacrificing intensity of the neutron beam signal, it is possible to use analyzer crystals with large d-spacing to improve the resolution, but that results in lower Q-ranges. BASIS typically utilizes the Si(111) (the largest d-spacing in Silicon) analyzer crystals, which achieves high energy resolution while maintaining the other spectrometer parameters. The scattering measurements at BASIS probes the quasi-elastic scattering originating from diffusion or low frequency dynamics at the picoseconds to nanosecond time-range.

The wide Angular-Range Chopper Spectrometer (ARCS) at the Spallation Neutron Source (SNS) is designed to supply neutron beam at the sample position with high flux and a wide solid angle of detector coverage for the scattered neutrons.[6] The instrument is home to some of the state-of-the-art neutron instrumentation techniques, such as an elliptically shaped supermirror guide in the incident neutron flight path, an oscillating radial collimator

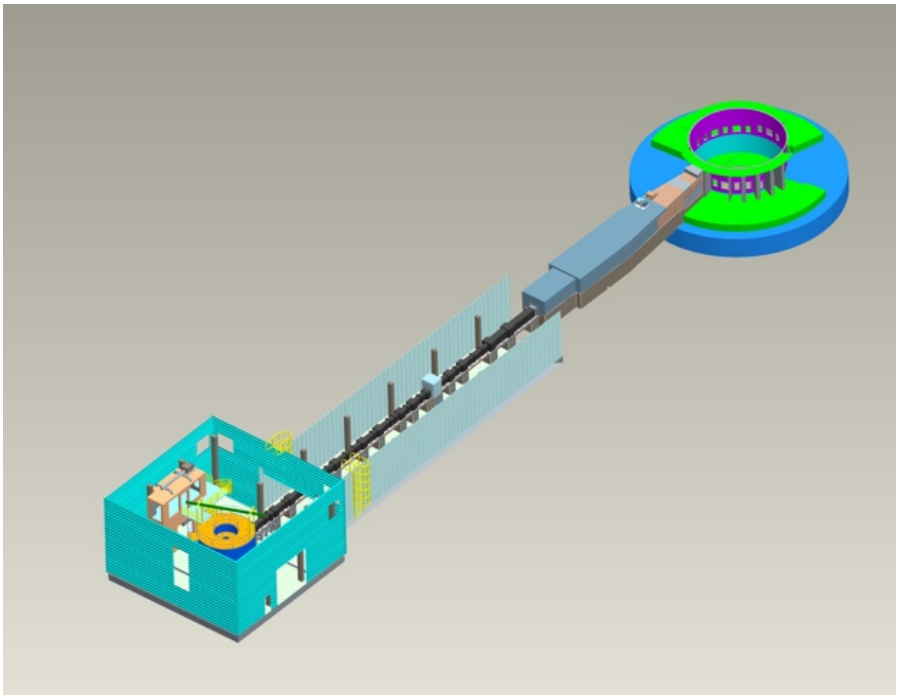

Figure 2.1 The schematic diagram of BASIS. A system of guides that transport the beam to the sample position through a corridor that connects the BASIS building with the main target.[1]

that significantly reduces background scattering, and a wide array of linear position sensitive ^{3}He detectors, some of them can be seen in the schematic diagram of ARCS in **Figure 2.2**. ARCS also utilizes a gate valve between the sample and the detector room, along with a window-free final flight path, which facilitates a rapid change of samples. The vacuum environment of the detector additionally provides minimal background scattering. The inelastic neutron scattering instruments such as ARCS, which belong to the class of time-of-flight spectrometers, is distinguished by the use of a Fermi chopper in the neutron flight path to the sample. A short burst of monochromatic neutrons were made to scatter off the sample by adjusting the Fermi chopper slits. The cylindrical array of over 100 modules of ^{3}He position sensitive detectors is positioned inside the detector chamber, which are placed around the sample to determine the scattering angle of the outgoing neutrons, from which the momentum transfer is measured. The final energies of the scattered neutrons are calculated from the total time-of-flight method, providing the energy transfer *E* of the scattering event. ARCS data reduction package was the first of its type to reduce event data using the pixel location of the detector (**Figure 2.3**) and the TOF of each detected neutron to a spectra *S(Q, E)*.

Cold Neutron Chopper Spectrometer (CNCS) at SNS is a direct geometry, multi-chopper spectrometer (**Figure 2.4**) at SNS (BL-5) which utilizes cold or thermal neutrons with high energy resolution to study dynamics of materials. CNCS consists of two high-speed choppers to shape the neutron pulse and to adjust the pulse length at the sample position. It exhibits the optimum performance from 1 meV to 50 meV incident energies. Like ARCS, CNCS utilizes the ^{3}He linear position sensitive detectors to characterize the

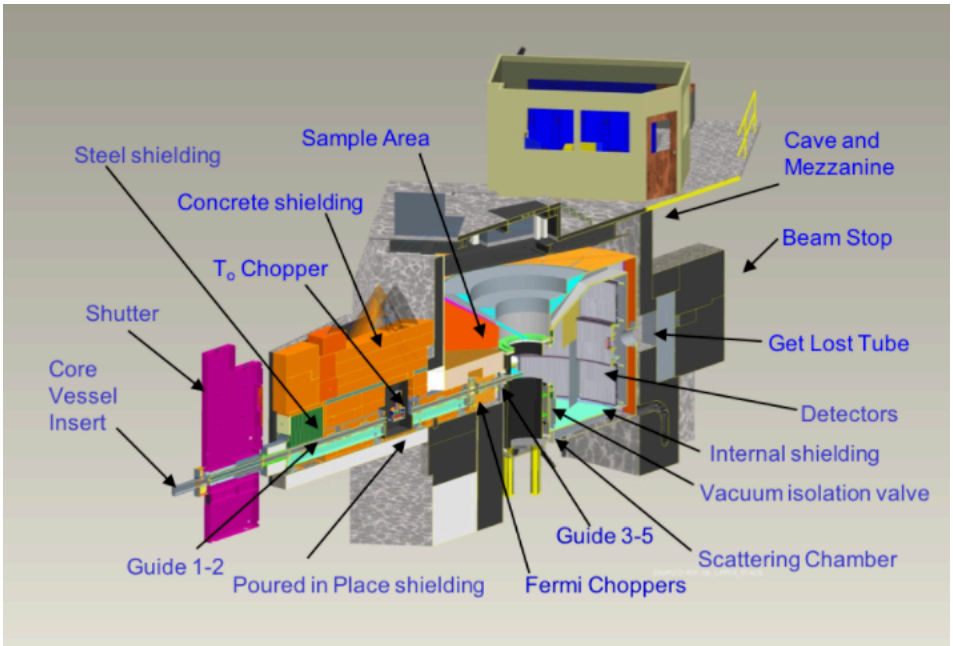

Figure 2.2 A schematic diagram of ARCS instrument showing the scattering chamber and other features.[6]

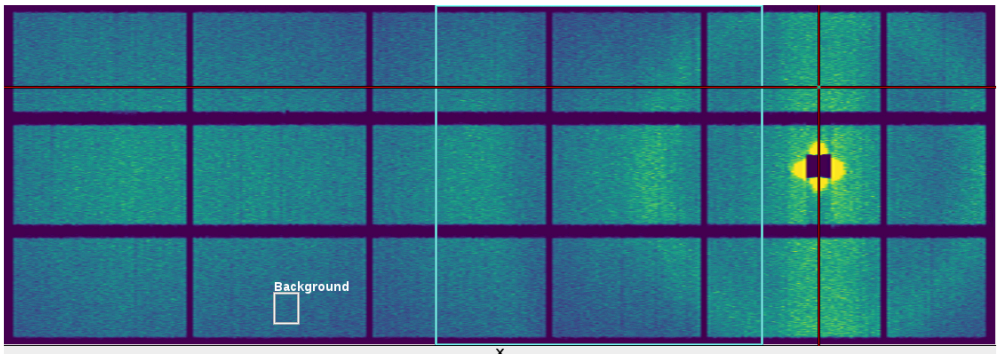

Figure 2.3 Neutron scattering data observed in the ARCS data acquisition software. This is reduced to *I(Q, E)* using the positions and angles of each detector from the sample.

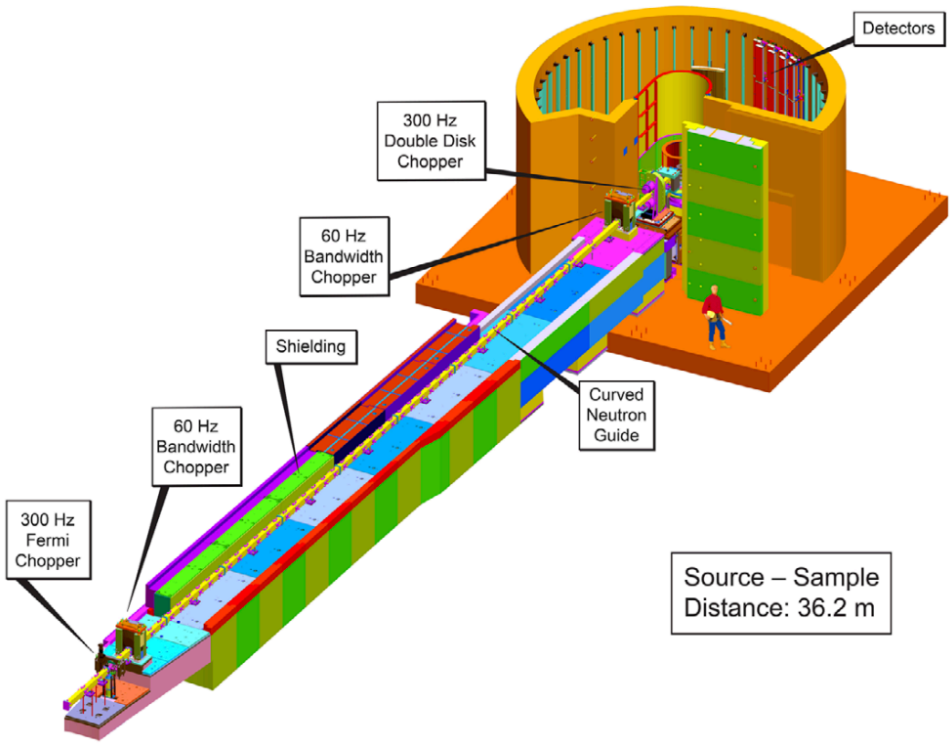

Figure 2.4 A schematic diagram of the CNCS spectrometer. [4]

momentum transfer of scattering. The detector array consists of 400 tubes, each of length 2 meters with a solid angle of ~ 1.7 steradian. The high energy resolution available at CNCS, which ranges from 10-500 μeV is useful in investigating long relaxations with time-range greater than 10 ps in liquids.

CHAPTER 3 INELASTIC SCATTERING STUDY OF WATER DYNAMICS

A Brief History of Water

Water plays a central role in many scientific disciplines. It is a fundamental material for the living, and remains the most researched compound on our planet. The importance of water in our lives cannot be overstated - it covers two-thirds of our world, and constitutes more than 60% of the adult human body. Understanding the structure and dynamics of water will significantly impact many fields of life sciences and industrial sciences[39, 40]. At the same time, water is known for its anomalous properties, which have long baffled scientists[39, 41]. It is understood that the extensive hydrogen bond network is responsible for these anomalies[41, 42]. However, the atomistic mechanisms such as specific configurations of molecules and local correlated dynamics, which are undoubtedly influenced by the hydrogen bonds, leading to these anomalous properties remain elusive. The avenue of research in understanding the properties of water have mostly been macroscopic in nature. The spectroscopic techniques such as Raman, IR and ultraviolet spectroscopies have been used to understand the molecular vibrational modes in water. Being a polar liquid, H+ and OH- diffusion mechanism have been of interest and studied using techniques, for example, dielectric relaxation spectroscopy. Although they are powerful methods to understand the molecular dynamics in systems, they lack a very fundamental characteristic necessary to study the origin of liquid state behavior in depth – the spatial resolution. Until the last decade, studies linking structure and dynamics of liquids were few and far between. The "structure" of liquids were studied using diffraction technique by transforming the reciprocal space data into the real-space using the pair-distribution functions. The pair-distribution studies of water dates as far back as 1938 when x-ray diffraction technique was

used to determine the radial distribution function of water.[43, 44] X-ray diffraction data primarily contains information from the oxygen atoms due to their relatively high electron density compared to hydrogen, therefore the obtained pair-distribution functions are inter-molecular in nature. To see the hydrogen atoms, we require a different probe. This is where neutron diffraction techniques come in. The first neutron pair-distribution function of water[45] was obtained by Narten, Thiessen, and Blum in 1981 following their works exploring the x-ray studies[46] in 1967. They derived the three atomic pair distribution functions from neutron diffraction data on four mixtures of light and heavy water, $g_{O-O}(r), g_{O-H}(r)\ and\ g_{H-H}(r)$. Experimental pair-distribution functions have improved the computational modelling of water through verifying the inter-atomic distances and estimating the coordination shell characteristics. The disconnect between the structure studies and dynamical studies in water prompted a study where the correlated dynamics of water was probed using the Van Hove function from inelastic scattering studies.[7] It was shown that the nearest neighbor molecules move away as time evolves while next-nearest neighbor molecules move toward the central atom. This was visualized by determining the Van Hove function of water from x-ray inelastic scattering[7] as seen in **Figure 3.1**. This is in contrast to what is observed in simple metals where atomic correlations are weak due to the weak nature of the metallic bonds[47]. In simple metals, the cutting and forming of a bond are not correlated unlike what is seen in water. Therefore, using Van Hove function to link the structural and dynamical behavior of water in atomic length and time-scales will help further our understanding of this very complex, yet the most important liquid on our planet.

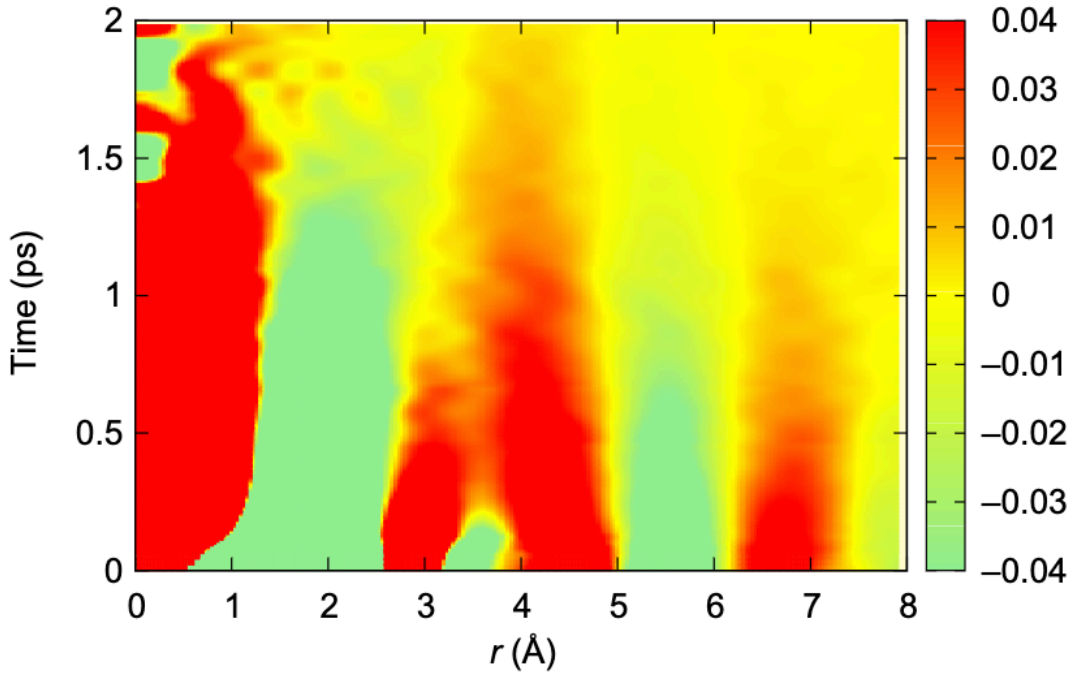

Figure 3.1 The Van Hove function, *G(r, t)*, of liquid water measured from Inelastic X-ray Scattering measurements.[7]

Neutron Van Hove function of water

The inelastic scattering measurement of water using x-rays provides the 'molecule-molecule' correlated dynamics in water because x-rays only see oxygens because the scattering cross-sections of the two isotopes of hydrogen (H^1 and H^2) are negligible compared to that of oxygen.[48] As there exist only a single oxygen in a molecule, the scattering data consists of oxygen-oxygen correlations, in other words, inter-molecular correlations. However, the neutron cross-sections for Deuterium (inter-changeably represented by H^2 or D) and Oxygen are comparable, therefore neutron scattering of heavy water (D_2O) provides richer information, such as the intra-molecular correlations between O & O, O & H, and H & H. It is a significantly harder challenge to elucidate the inner-workings of water molecules from neutron scattering because of the over-whelming amount of atomic correlations. Therefore, we depend on classical molecular dynamics simulations to explain the experimental findings. The current chapter will explore the many techniques and the results we obtain from the Van Hove function study of water from inelastic neutron scattering experiments. The conventional instrument for performing inelastic neutron scattering measurements was the Triple-Axis-Spectrometer (TAS), which utilizes the continuous beam of neutrons from a reactor neutron source.[49] The measurement of scattering data is performed by fixing a Q and scanning over E, then switching to another Q, and vice versa. Thus, the TAS measurement is a time-consuming process, which requires a few hours for a single scan of Q or E. Therefore collecting even a single spectra of $S(Q, E)$ would take weeks or months. The spectrometers equipped with wide, two-dimensional detectors made in the modern pulsed neutron facilities made it possible to

measure the *S(Q, E)* in a relatively short time. It is now viable to obtain a *S(Q,E)* scan over a wide energy and momentum transfers within a few hours at the Spallation Neutron Source spectrometer.

Inelastic Neutron Scattering at ARCS Spectrometer

We utilize the direct geometry chopper spectrometer, ARCS at SNS, for carrying out the inelastic scattering study of water. This class of spectrometers have successfully measured dynamics in materials using the energy ranges from meVs up to a few eVs encompassing a broad range of scientific disciplines. ARCS is capable of using incident energies upward of 15 meVs to a few eVs with an elastic energy resolution of 3% - 5% of the incident energy, with the corresponding momentum transfers ranging from 6.3 $Å^{-1}$ to 37 $Å^{-1}$. A neutron *S(Q, E)* measured from water would be dominated by the incoherent scattering from hydrogen (cross-section = 80.26 barns) in comparison to its negligible coherent scattering contribution (cross-section = 1.76 barns). As we learned earlier, the incoherent scattering provides details on the diffusive dynamics, and makes it difficult to study the distinct atomic correlations in the system. To resolve this issue, we use deuterated water (hydrogens replaced with deuterium). Deuterium (^2H) possesses a higher coherent scattering cross-section compared to hydrogen, with significantly lower incoherent scattering cross-section (2.05 barns for D against 80.26 barns for H). This approach doesn't compromise any of our objectives of studying the dynamics of water because studies have shown that water and heavy water, despite their obvious differences in their mass, possess little differences in their structural and dynamical behaviors.[50, 51] Therefore, we used the heavy water (D_2O) as our material of interest to study using neutron scattering techniques.

In the following section, we establish a proof-of-concept of the feasibility of using ARCS, or in general neutron scattering spectrometers at SNS, to study the correlated dynamics of water on a picosecond time-scale.

The structure of water has been a topic of interest to researchers from many disciplines thanks to the range of applications it is used in. The "structure of water" may sound like an oxymoron as it is a liquid and we know that liquids do not have any fixed shape. In literature, "structure of water" means the snapshot or same-time correlations between the constituent atoms that gives rise to its specific properties, which are the results of the forces between the atoms. By measuring the correlations we can attempt to understand the forces and the underlying mechanisms that make water the special liquid it is.[51] This is where scattering techniques (photon or neutron), which measure the microscopic atomic-level correlations, are of great utility. The PDF of water was measured using x-ray and neutron scattering measurements and have contributed massively to our understanding of the structure of water. The neutron scattering of hydrogen is very different to that from deuterium, hence by measuring the scattering data from light water, heavy water and a mixture of the two, one can obtain the three partial pair distribution functions. These functions, $g_{O-O}(r)$, $g_{H-H}(r)$, and $g_{O-H}(r)$, describe the average structure of water, and they have been studied thoroughly in the last few decades. We know that the nearest neighbor separation (molecular) in water is 2.8 Å, and the next nearest neighbor distance is 4.5 Å by obtaining the $g_{O-O}(r)$ of water. $g_{O-H}(r)$ provides an opportunity to measure the covalent bond length (O-H) – 1 Å, as well as the hydrogen bond length in water, which is approximately 1.8 Å. The coordination number of water can be estimated from $g_{O-O}(r)$

as the area under its first peak. The coordination number of water (~4.5) points to it possessing an inter-molecular tetrahedral network, as a result of the hydrogen bond connectivity between molecules. The static pair distribution functions *g(r)*, despite providing rich insights regarding water's structure, are unequipped to probe the dynamics of water. Complementing the structural information with spectroscopic measurements such as NMR or Raman scattering is futile because they lack the spatial resolution to connect the dynamical information. The Van Hove function is the generalized pair-distribution function, which describes the time-dependence of the atomic correlations. Estimating the Van Hove function of water from inelastic neutron scattering technique is a major challenge, but simultaneously a big step in the process of elucidating the atomic dynamics in water.

Experimental Details and Data Reduction

The sample (D_2O) is placed in a Vanadium container shaped like an annulus with negligible thickness (less than 1 mm). Vanadium is chosen as the sample container because it acts as an incoherent elastic scatterer on pulsed neutron spectrometers with neutron energies up to 1 eV,[52] providing no contribution to the structural dynamics of the system. The raw data collected from the D_2O sample placed inside a Vanadium container setup is reduced by the direct-geometry spectrometer (DGS) reduction routine, using the Mantidplot software[53, 54] from Mantid project and the beamline parameters extracted from standard white beam calibrations. The $I(Q, E)$ spectrum was obtained for the sample and the empty Vanadium setup (for the subtraction of the background). Alternatively, the DPDFreduction algorithm (which uses the DGS reduction routine) in the MantidPlot software may be used to convert

the raw scattering data to the *I(Q, E)* spectra as shown in **Figure 3.2**. The *Run Numbers* for the sample, the white *Vanadium* scattering data for detector calibration, and the *Empty Can Run Numbers* are given for the reduction routine. Selection of the parameters for the reduced data may be specified in the *EnergyBins* (for example, *-70, 0.1, 70* means the energy ranges for the spectra being -70 meV to 70 meV with energy bin of 0.1 meV). It is also possible to specify only the energy bin (0.1 meV for instance) and let the algorithm determine the energy ranges based on the incident energy. The output workspace is then saved as an ascii file to begin the data exploration using the in-house data analysis framework. The *I(Q,E)* of D_2O at 295 K for 70 meV incident energy is shown in **Figure 3.3**. The maximum Q value is about 11.8 $Å^{-1}$ for E_i = 70 meV, which contains the first three broad scattering peaks from water. Scattering peaks beyond this Q_{max} have negligible intensity and contribute little to the Fourier transform-obtained $F(Q, t)$ and $G(r, t)$, thus the Q-range measured by this INS experiment is reasonable for our purposes. The transformation of *I(Q, E)* to the *S(Q, E)* is done by applying the detailed balance equation the spectra to the missing *Q-E* coordinates using the equation below, then normalizing the spectra by the square of the mean scattering length, $\langle b^2 \rangle$, of the compound.

$$I(Q, E) = I(Q, -E) \exp(E/k_B T)$$

S(Q, E) is transformed to the *F(Q, t)* – the Intermediate Scattering Function by Fourier transforming over *E* as shown in the equation,

$$F(Q, t) = \int S(Q, E)\, e^{-iEt/\hbar}\, dE.$$

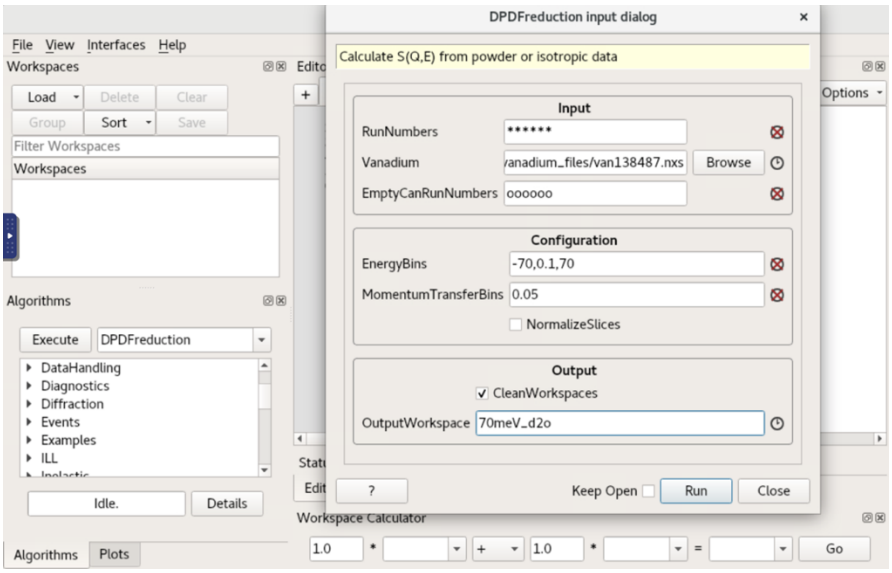

Figure 3.2 DPDF reduction dialog box in the MantidPlot software.

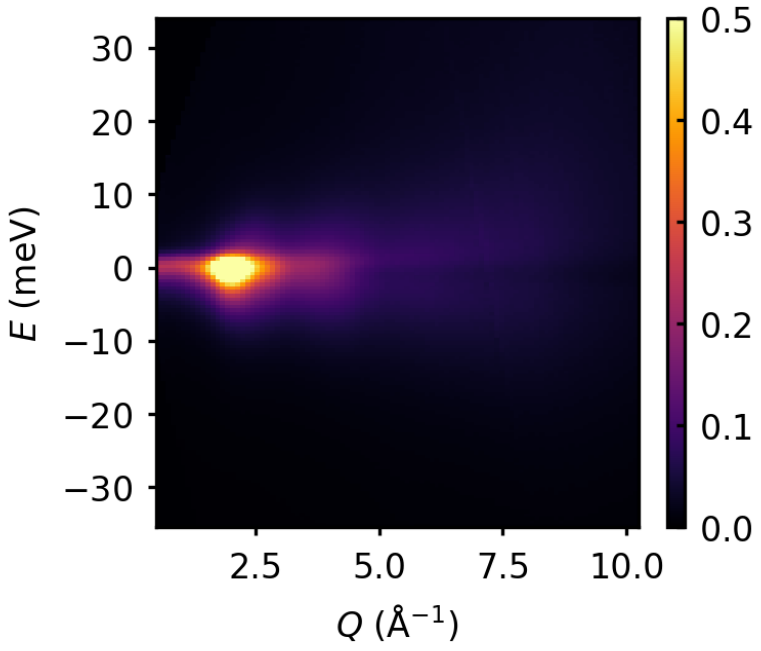

Figure 3.3 *I(Q,E)* processed using the DPDF reduction algorithm ready for transformation to the Van Hove function in real-space and time.

The intensity plot and the time-sliced plots of *F(Q, t)* are shown in **Figure 3.4** and **Figure 3.5**. It can be observed that $F(Q, t=0)$ is oscillating around a constant value as Q tends to ∞, suggesting that the relation $S(Q) = F(Q, t=0)$ is followed. To enforce that the $S(Q)$ oscillates around unity as $Q \rightarrow \infty$, $F(Q, t)$ is normalized by a Gaussian curve of the form $G(Q) = A \exp(-BQ^2)$, the parameters A and B of which is obtained by fitting the $F(Q, t=0)$ with the Gaussian function. The intermediate scattering function is widely used to study liquid dynamics over the past decade. The common approach in liquid community is to analyze the first peak of $F(Q, t)$ and measure the characteristic relaxation time of the system, which is termed the α-relaxation time. This received huge popularity in the liquid community, primarily because it was simple and *F(Q, t)* data containing the structure factor maximum $S(Q_{max})$ was available from quasi-elastic measurements and spin-echo measurements. This also relieved researchers of obtaining the *S(Q,E)* or *F(Q, t)* to wider ranges of Q, which was a great challenge at the time. Considering that the scattering data of liquids contain diffused peaks, it is difficult to understand how measuring the dynamics at a single Q-point would reveal the true nature of dynamics in liquids. Later, it was shown in 2018 that this method is misleading, and the α -relaxation time does not provide the true structural change or local dynamics of the liquid system by our research group.[55]

The energy resolution of the inelastic neutron scattering instrument depends on the chosen incident energy. Therefore, the scattering intensity from the sample is convoluted with neutron beam energy profile. To improve the energy resolution of the instrument, the incident energy need to be decreased ($\Delta E = 3\% - 5\%$ of E_i). Even though it is possible to perform the scattering measurements at lower incident energies, that would result in

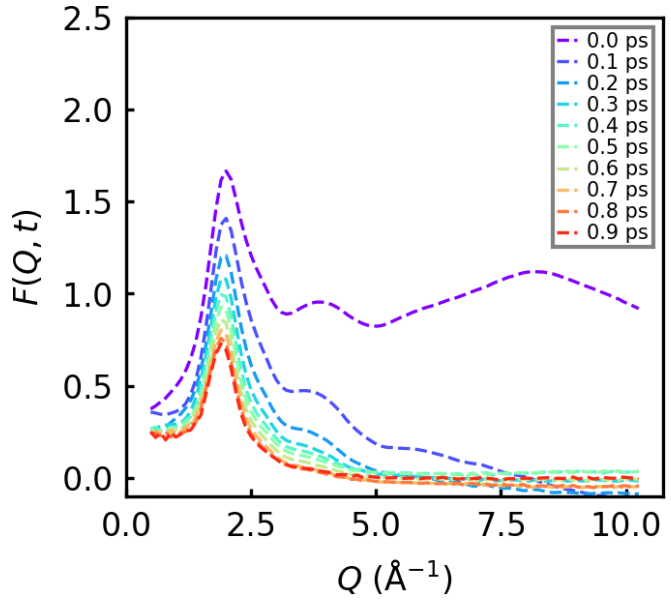

Figure 3.4 Time-sliced *F(Q, t)* at 295 K for D2O

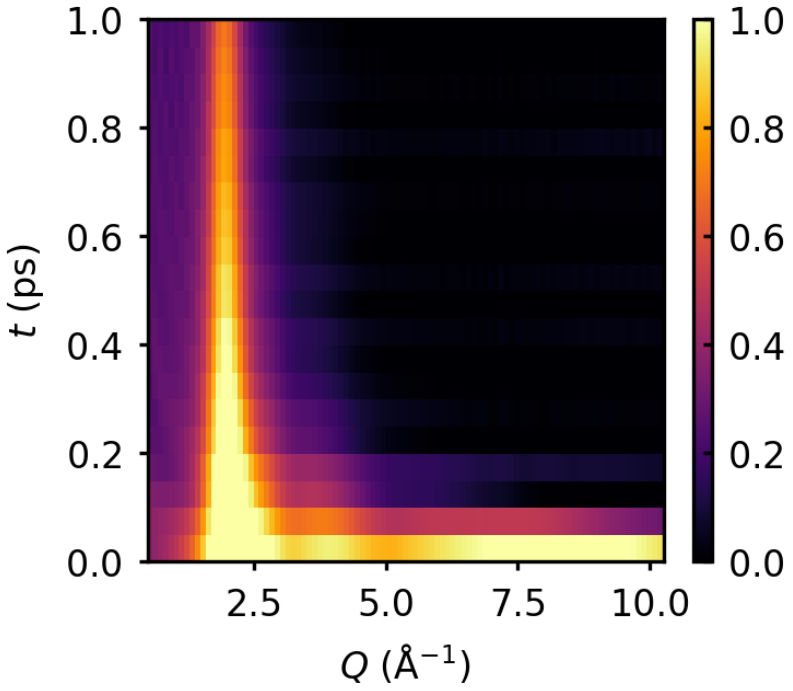

Figure 3.5 Intensity plot for *F(Q, t)* of heavy water from INS measurement at ARCS for T = 295 K.

limiting the *Q* range of *S(Q,E)*, which in its turn makes the Fourier transformation procedure to real-space impossible. As an alternative, we implement the energy resolution correction by deconvoluting the energy profile of the spectrometer, $S_V(Q,\ E)$, from the sample data. The neutron energy profile is obtained by measuring the *S(Q, E)* of a Vanadium rod (a purely incoherent scatterer). The *S(Q, E)* of Vanadium at an incident energy can be used to describe the corresponding neutron energy profile. Hence, the total dynamic structure function can be expressed as:

$$S_{total}(Q,\ E) = S_{sample}(Q,\ E) * S_V(Q,\ E),,$$

where $S_{total}(Q,\ E)$ is the total dynamic structure function measured, $S_{sample}(Q,\ E)$ is the dynamic structure function for the sample alone, and $S_V(Q,\ E)$ is the dynamic structure function measured from the standard vanadium sample with the same incident energy, which represents the neutron energy profile. Upon Fourier transforming the *S(Q, E)* to *F(Q,t)*, the convoluted functions becomes a product as the following:

$$F_{total}(Q,t) = F_{sample}(Q,t)\ \cdot\ F_V(Q,t),$$

Where $F_V(Q,\ t)$ is independent of *Q,* therefore we change the notation to *R(t)* – the energy resolution function. Thus the intermediate scattering function for the sample is then obtained by

$$F_{sample}(Q,t),= \frac{F_{total}(Q,t)}{R(t)}.$$

The *S(Q, E)* of water contains both the self and distinct scattering contributions, the separation of which can be carried out by fitting *F(Q, t)* with a Gaussian function of the form $F_{self}(Q,t) = A(t)\ e^{-w(t)Q^2}$, where *A(t)* and *w(t)* are the amplitude and width

functions. A detailed account of studying the self-diffusion of water using the Van Hove function from inelastic x-ray scattering measurements can be found from Shinohara et al.[56] $F(Q, t)$ in all time-slices can now be fitted to separate the self-part, $F_{self}(Q,t)$, and distinct part,

$$F_{dist}(Q,t) = F(Q,t) - F_{self}(Q,t).$$

The usage of Van Hove function removes the requisite of the process of separation of self and distinct dynamics from the total *F(Q, t)*. For the relevant time-ranges accessible by neutron/x-ray scattering techniques ($0 - 10$ ps), the self-dynamics and the correlated dynamics will be revealed in non-overlapping spatial regions. The self-part will be located below 2 Å, whereas the distinct-atom correlations shows up beyond 2 Å in the Van Hove function. This is interpreted in the following way; the time a particle takes to diffuse beyond a particular spatial range is shorter than the time a group of atoms behave collectively. Thus the time regime engulfed by the two following time-scales, vibrational dynamical regime (< 0.1 ps) and the long diffusive regime (>10 ps) plays a key role in elucidating the atomic dynamics in liquids. We choose not to separate the self and distinct *F(Q, t)*, and proceed with the resolution correction. The corrected *F(Q, t)* is now ready to be Fourier transformed to the Van Hove function. In the ideal world, the transformation over Q and E will be done from 0 to ∞ for Q and from $-\infty$ to ∞ for E. Unfortunately, the experimental conditions limit the ranges of the accessible Q–E space. If this Q or E range is not large enough, the Fourier transformation introduces termination errors, which are manifested as oscillations in the Van Hove function. The energy ranges available and the resolution determines the time-ranges and resolution after the Fourier transformation process. The shortest time

resolved, $\Delta t = {}^{\hbar}/_{E_{max}}$ where E_{max} is the maximum energy. Similarly, the maximum time limit is determined by the energy resolution, $t_{Max} = {}^{\hbar}/_{\Delta E}$, where ΔE is the energy resolution. This may also be extended to the momentum-space and real-space ranges. The spatial resolution is determined by the Q range, as $\Delta r = {}^{2\pi}/_{Q_{max}}$. The maximum spatial range of the data is determined by the momentum resolution, as $r_{Max} = {}^{2\pi}/_{\Delta Q}$.[18] Obtaining *F(Q, t)* or *S(Q, E)* over a wide range of the *Q–E* space is key to a reliable measurement of the Van Hove function. This is why choosing the right instrument and the ensuing design of scattering experiments is of great importance. Determine the energy resolution required for the dynamical regime of interest, then choose the instrument and parameters (energies, chopper frequencies, neutron statistics). A solution to this problem would be to measure different energy data and create a master *S(Q, E)* by combining the results. There are two ways to estimate the Van Hove function, one is to transform the *S(Q, E)* data to *F(Q, t)* first and then transform to *G(r,t)*. The second is to estimate *g(r,E)* instead of *F(Q, t)*, then transform it to *G(r,t)* as shown in equation below. It was determined that it is best to go the second way to minimize the termination error from previous work on the x-ray Van Hove function of water, using the following equation to transform the data,[7]

$$F(Q,t) = \int S(Q,E)\, e^{-iEt/\hbar}\, dE.$$

A modification function was proposed by Lorch (1969) to suppress the spurious termination ripples when scattering data is Fourier transformed over a finite range in the reciprocal space to real space.[57] The Lorch function is given as,

$$M(Q_0) = \frac{sin\,(Q_0\,\Delta_r)}{Q_0\Delta_r}, \text{ for } Q_0 \leq Q_{max}.$$

We use the Lorch function near the Q_{max} to suppress the termination errors in our data. Then the Fourier transformation to the real-space is as follows:

$$G(r,t) = \frac{1}{2\pi^2 \rho r} \int M(Q)\, F(Q,t) \sin(Qr)\ Q\, dQ.$$

The Van Hove function of D_2O at 295 K is shown in **Figure 3.6**, and the intensity plot of the VHF in **Figure 3.7**. The first peak represents the covalent bond (O-H) at ~ 1 Å, the shorter peak at 1.8 Å belong to the hydrogen bond. The peak around 2.3 Å represent the shortest H-H intermolecular correlations. All of these correlations are characterized by fast dynamics, which are difficult to study in the dynamical regime given by the instrument, as seen by their decay by 0.1 ps in **Figure 3.6**. The broad peak centered around 3.5 Å encompasses two correlations, H--O and H--H, where each atom belongs to different molecules, as can be seen from **Figure 3.8**. The relaxation time of this peak is < 2 ps, but the instrument lacks the necessary time-range for the incident energy setting (70 meV) to determine the accurate relaxation times. Additionally, we notice a shift in the peak position from 3.5 Å to 3.9 Å in the span of 1 ps, however the meaning of this peak-shift remains to be inconclusive. Through this work, we have now established that estimating the neutron Van Hove function of water is feasible, and the VHF exhibits all the atomic correlations in real-space. In the next section, we apply the same approach to study the dielectric relaxation behavior of water from inelastic scattering technique using BASIS and CNCS spectrometers.

Neutron Scattering Study of Dielectric Relaxation in Water

One among the many anomalous properties of water, the high dielectric loss at low

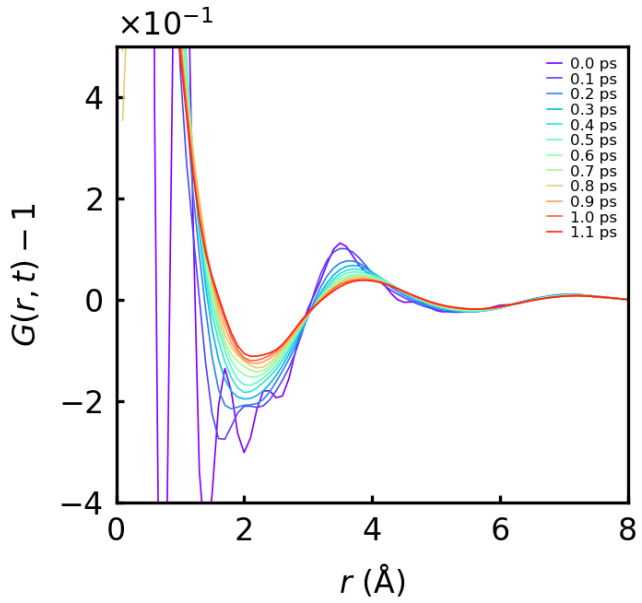

Figure 3.6 Time-sliced *G(r, t)* of water at 295 K

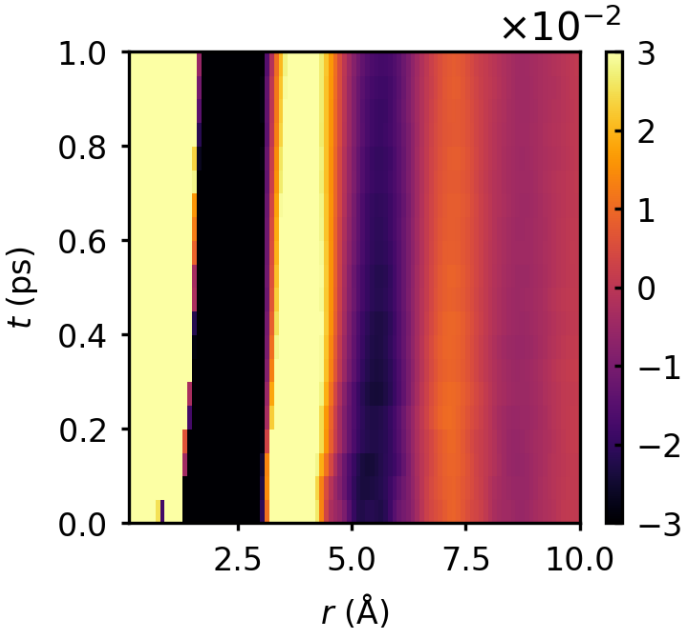

Figure 3.7 Intensity plot of *G(r, t)* of D_2O at 295 K

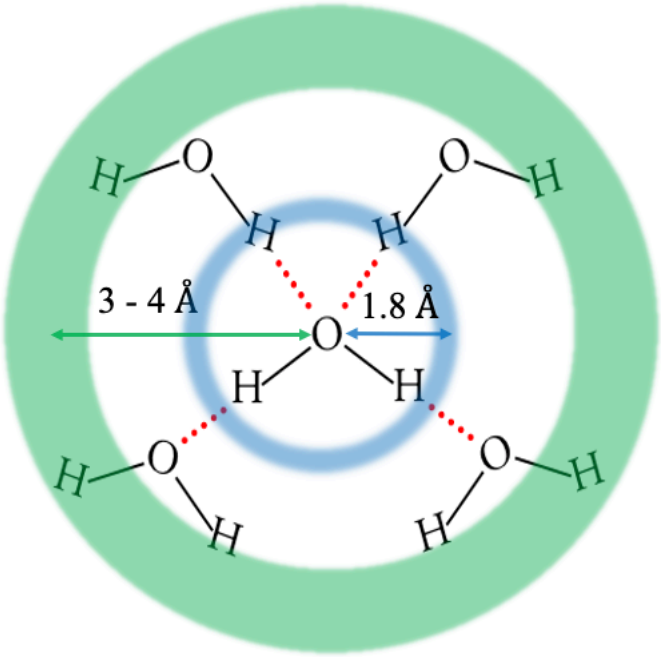

Figure 3.8 A 2-D visualization of the molecular arrangement in bulk water. The shorter distance (1.8 Å) corresponds to the hydrogen bond, and the longer distance (3 - 4 Å) to the intermolecular O--H and H--H correlations.

frequencies (20 GHz) deserves our special attention. It is routinely utilized in our daily lives as the working principle of the microwave oven. We investigate the mechanism behind this phenomenon by employing inelastic neutron scattering (INS) with the results displayed in real space and time. As we learned on the earlier chapter instrumental methods, neutron scattering is a microscopic probe, therefore the scattering data contains valuable information regarding the atomic dynamics of water. Our results show that the dielectric loss is created by highly collective dynamics of water molecules, which most likely originates from the quantum-mechanical nature of the hydrogen bonds.

Water is a polar molecule, with a dipole moment of 1.85 D (Debye). The water dipoles undergo an torque in an external electric field, and becomes aligned with the field direction, thereby minimizes the total energy of the system. In a microwave oven, water molecules undergo reorientation motion resulting in energy loss, which heats up the system. There is clear consensus that the motion of water molecules in water is controlled by the extensive hydrogen bond network. Dielectric spectroscopy has been used to study this phenomenon in the past to cover the full spectrum of the complex dielectric response of water[58, 59]. Substantial dielectric loss is observed from dielectric relaxation spectroscopy measurements with the maximum at $\nu_{\max}$~19 GHz with a characteristic relaxation time, $\tau_D = (2\pi\nu_{\max})^{-1} \approx 8.3$ ps as shown in **Figure 3.9**. The shape of the spectrum is well described by a single Debye relaxation mechanism: $\varepsilon'' = \omega\tau(\varepsilon_s - \varepsilon_\infty)/(1 + \omega^2\tau^2)$, where ε'' is the imaginary part of the complex dielectric permittivity, ε_s is the static permittivity, ε_∞ is the permittivity at high frequencies beyond the microwave region, ω is the angular frequency of the applied electric field, and τ is the dielectric relaxation time.

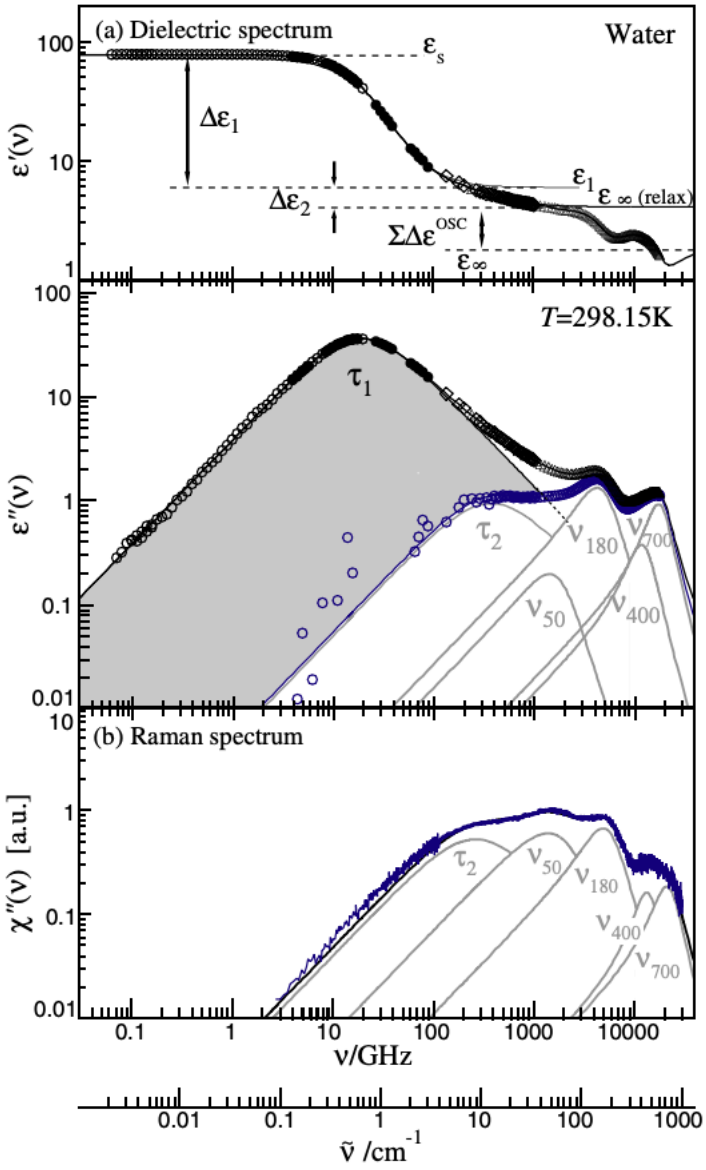

Figure 3.9 a) The complex dielectric spectrum of water at 25 °C. The blue symbols denote the dielectric loss after subtracting the contribution from process I. (b) Raman spectrum of water at 25 °C. [5]

The mechanism causing this response (process I) remains widely debated. In 1929, Peter Debye was the first to attempt an interpretation for this phenomenon in terms of the re-orientational diffusion of single water molecules.[60] Debye assumed liquids as an elastic continuum in which a polar molecule (assumed to be a perfect sphere) undergo reorientation motion, and estimated the relaxation time associated with it and found that it agrees with the experimentally determined value of dielectric relaxation time. The Debye relaxation time was estimated by $\tau_D = 4\pi a^3 \eta / K_B T$, where a is the radius of the sphere and η is the viscosity of the liquid. Strong non-Debye behavior of the calculated dielectric spectrum was estimated from computer simulations if only the orientational relaxation is considered by Ohmine,[61] and by Bagchi and Chandra.[62] In 1996, Agmon suggested that two different molecular mechanisms contribute to the dielectric relaxation in water, and slower translational mechanism may be the mechanism behind dielectric relaxation, instead of single molecular rotations[63]. A fast relaxation at higher frequencies (process II) was introduced in addition to the Debye relaxation, to model the THz reflection spectroscopy results by Rønne et al.[64] This additional fast-relaxations (sub-THz) observed[65, 66] are interpreted as structural relaxations[67]. This peculiar dielectric response is also observed in monohydroxy alcohols, but their properties are not as anomalous as of water. A review of the developments towards the microscopic understanding of dielectric relaxation of mono-alcohols can be found in Böhmer et al.[22] It is now believed that the cooperative reorientation of water molecules causes the Debye loss in water, and other hydrogen bonded liquids. [68-74] One of the models that try to explain the Debye behavior is the 'wait and switch' model, which explains the Debye process based on an activated jump

mechanism of a dipolar group. The dipolar molecule rotates to another orientation only if one or more hydrogen bonds are broken. Therefore, different dipole orientations are separated from each other by a potential energy barrier. Hence, the reorientation of a molecule occurs only if another molecule exist in a suitable position. For water, the estimate suggests about 10 ps at room temperature for a 'fifth neighbor' molecule to be present in a position that enables reorientation.[74] However, the origin of the defects in water that enables such a behavior in water is widely debated. There are also theories proposed based on orientational defects and ionic defects to explain the phenomenon[75], but a consensus on the correct mechanism behind the dielectric relaxation of water is yet to be reached.

For many years, it was thought that the only direct experimental technique that could detect the dielectric relaxation was spectroscopic techniques, based on charge fluctuations such dielectric spectroscopy. To probe the nature of the Debye relaxation process, majority of the research in this field has utilized dielectric spectroscopy. However, dielectric spectroscopy provides information only for the frequency dependence, and does not offer information on the microscopic details of the relaxation. This scenario began to change as coherent inelastic scattering techniques became accessible with the advances of instrumentation in neutron sources. Coherent neutron scattering techniques made it possible to see the time-resolved structure of materials. Recently, quasi-elastic neutron scattering was deployed to study the nature of dielectric relaxation in water.[76] However, the quasi-elastic scattering provides a limited Q-range range ($Q < 2$ Å^{-1}), where Q is the momentum transfer in scattering. As the real-space and Q-space are related by a Fourier

transform, to fully understand the real-space phenomena requires real-space analysis, which is not possible to carry out with a limited Q-range. This limits us from harvesting atomic level information of the microscopic mechanism.

We perform the INS measurement on D_2O to determine the dynamic structure factor, $S(Q, \omega)$, where $E = \hbar\omega$ is the energy transfer in scattering, over a wider Q-range ($0.6\ \text{Å}^{-1} < Q < 5.7\ \text{Å}^{-1}$) and present the results in terms of the Van Hove function (VHF) which describes dynamic atomic correlation in real space and time[24]. Heavy water (D_2O) is used because hydrogen strongly absorbs neutron and has a large incoherent cross section for neutron. The VHF is defined by

$$G(r,t) = \frac{1}{4\pi\rho_0 N r^2} \left\langle \sum_{i,j}^{N} \delta\left(r - \left|\boldsymbol{r}_i(t) - \boldsymbol{r_j}(0)\right|\right) \right\rangle,$$

where $\boldsymbol{r}_i(t)$ is the position of the i-th atom at time t, N is the number of atoms in the system, ρ_0 is the average number density, and $\langle \ldots \rangle$ denotes thermal and quantum averages. It is obtained by double-Fourier-transformation of $S(Q, \omega)$ from Q to r, and ω to t.[24] The VHF has been known for half a century, but because of the difficulty of collecting data over a sufficiently wide range of Q and E in reasonable time frames, it has not been used in the study of dynamics beyond early attempts[25, 77]. However, because of the advent of pulsed neutron sources with wide two-dimensional detector arrays, $S(Q, \omega)$ can now be measured in a much shorter time[78]. In the present work, we carried out the INS measurements of D_2O at the Backscattering Silicon Spectrometer (BASIS)[1] and the Cold Neutron Chopper Spectrometer (CNCS). The BASIS uses a backscattering geometry to measure the scattering of neutrons, whereas the CNCS uses the direct-geometry. Both of them have

high energy-resolution (33 μeV for BASIS and 125 μeV for CNCS) allowing to probe the dynamics with long relaxation time.

The Neutron Scattering Experimental Setup

99.99% deuterium substituted water was used for the experiment. The use of deuterium allows us to observe the self-part and the distinct-part of the Van Hove function. The coherent neutron scattering cross-section of deuterium (5.6 barns) and oxygen (4.2 barns) suggests that each atomic correlations, O-O, D-D and O-D will contribute to the total neutron scattering data based on the Faber-Ziman formalism[79]. The normalized weight of the O-O correlation is 0.09, D-D correlation is 0.49, and O-D correlation is 0.42. The D_2O sample was contained in a double walled Vanadium cylinder with an annular thickness of mm at both the beamlines. However, the annular radius was changed to accommodate the different beam sizes. Maintaining the sample thickness below 1 mm is crucial to avoid multiple scattering effects dominating the scattering data. The incident energy of the neutrons was kept at 18 meV at BASIS and at 7, 12 and 20 meV at CNCS. The detector efficiency was corrected by using the scattering data from the empty Vanadium containers. The dynamic structure factor from experiment, $S(Q, E)$, is then double Fourier transformed to $G(r, t)$. The INS measurements were performed at 295, 300 and 333 K at BASIS, as seen in **Figure 3.10**, and at 285, 300, 310, 320, 330 and 345 K at CNCS as in **Figure 3.11**. The neutron spectra were collected over ranges of Q (0.6 $Å^{-1} < Q < 5.7$ $Å^{-1}$) and E (-10 meV $< E <$ 10 meV). The raw data from the sample were reduced to by using the MantidPlot software[53] and the D_2O diffraction data[80]. The 2D intensity maps of *G(r,t)* from BASIS at three temperatures, 295K, 315K,

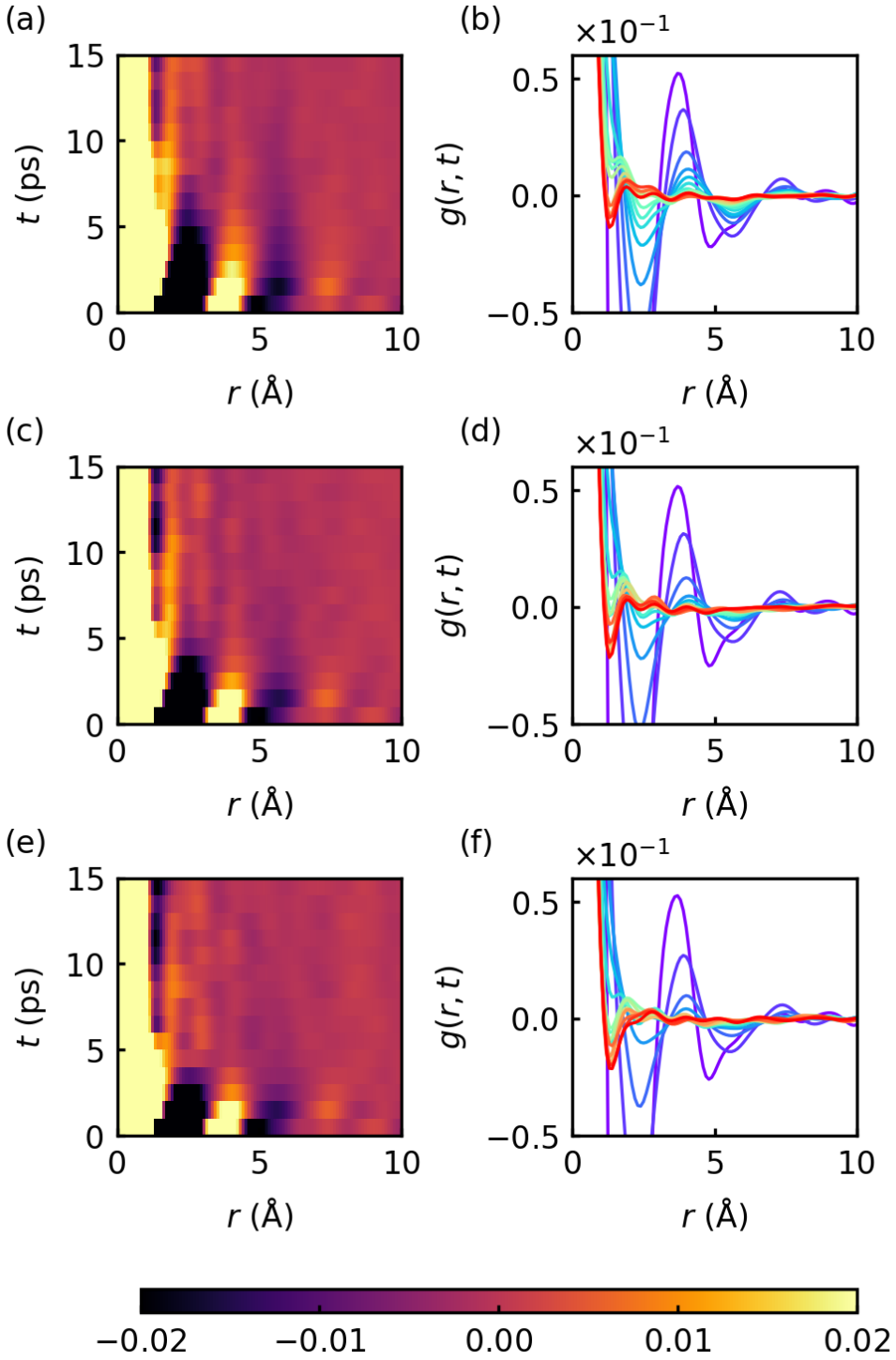

Figure 3.10 The *G(r, t)* of D_2O at three temperatures from BASIS, 295K (a, b), 316K (c, d), and 333K (e, f).

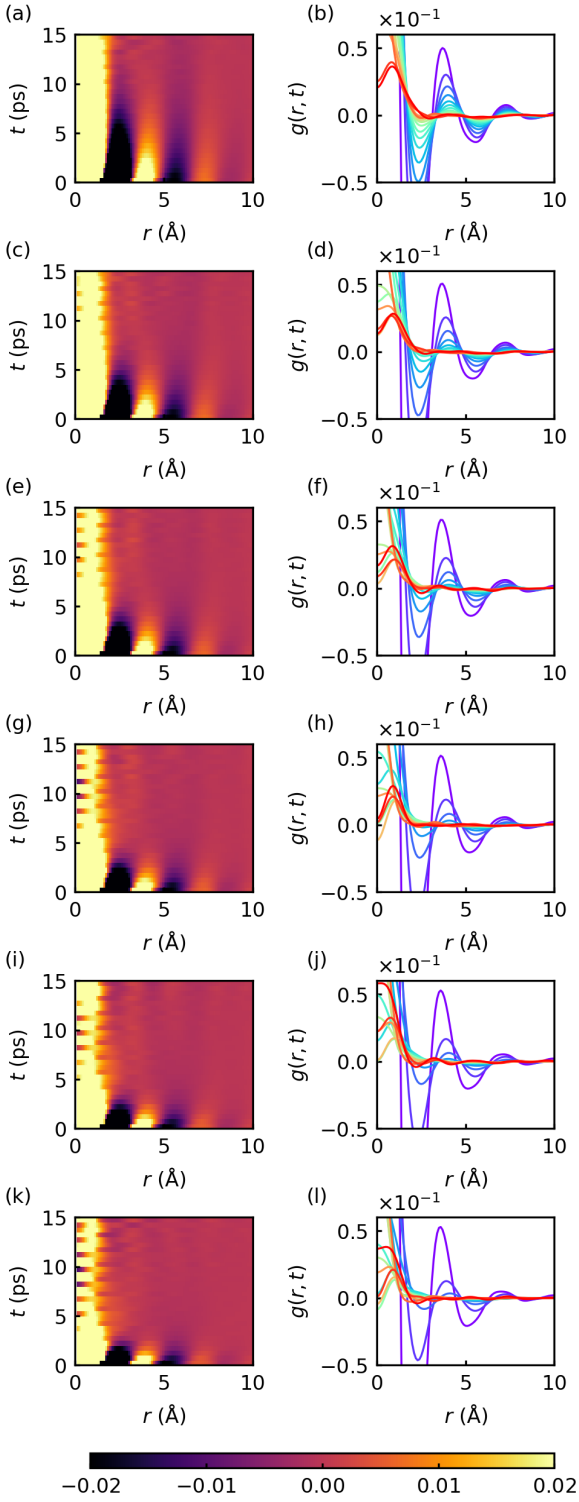

Figure 3.11 The *G(r, t)* from CNCS at six temperatures, 285K, 300K, 310K, 320K, 330K and 345K.

and 333K are shown in **Figure 3.10 (a, c, e)**, along with the time-sliced *G(r,t)* in **Figure 3.10 (b, d, f)**. The 2D intensity maps and the time-sliced from CNCS at six temperatures, 285, 300, 310, 320, 330 and 345 K are shown in **Figure 3.11**. The first peak observed in the *G(r,t)* at t = 1 ps is located at r = 3.9 Å, which encompasses both O- D and D–D intermolecular correlations. The valley that follows the peak, centered at 5.6 Å, exhibits significantly slower relaxation, which is quantitatively similar to the Debye relaxation time-scale, as shown in **Figure 3.12**. The peak/valley areas of the $G(r,t)$ were fitted using simple exponential relaxation functions to estimate the relaxation time, but the valley at 5.6 Å required two exponential relaxation functions due to the slowly relaxing tail; $A(t) = A_1 e^{-t/\tau_1} + A_2 e^{-t/\tau_2}$. The functional form of the fitting functions were chosen to be exponential because the Debye shape in the frequency response becomes an exponential behavior in time. The fitted curves can be found in the appendix. The relaxation time estimated from everywhere else in general was of the order of 2 ps, whereas a long relaxation time of 7 – 8 ps is observed for the region of 5.6 Å, which agrees with the Debye relaxation time of water at room temperature (~8.3 ps). The relaxation time of this region is plotted as a function of temperature along with the data obtained from previous dielectric measurements in **Figure 3.13**. It is clear that the temperature dependence of τ closely tracks that of the Debye relaxation time. Interestingly, the dipole-dipole correlation function of water shows positive correlation in the range of 5-6 Å by previous MD simulation works[81, 82] suggesting a direct connection between the dipole-dipole correlation and the slow decay of the VHF at these distances. Because the molecular separation, the

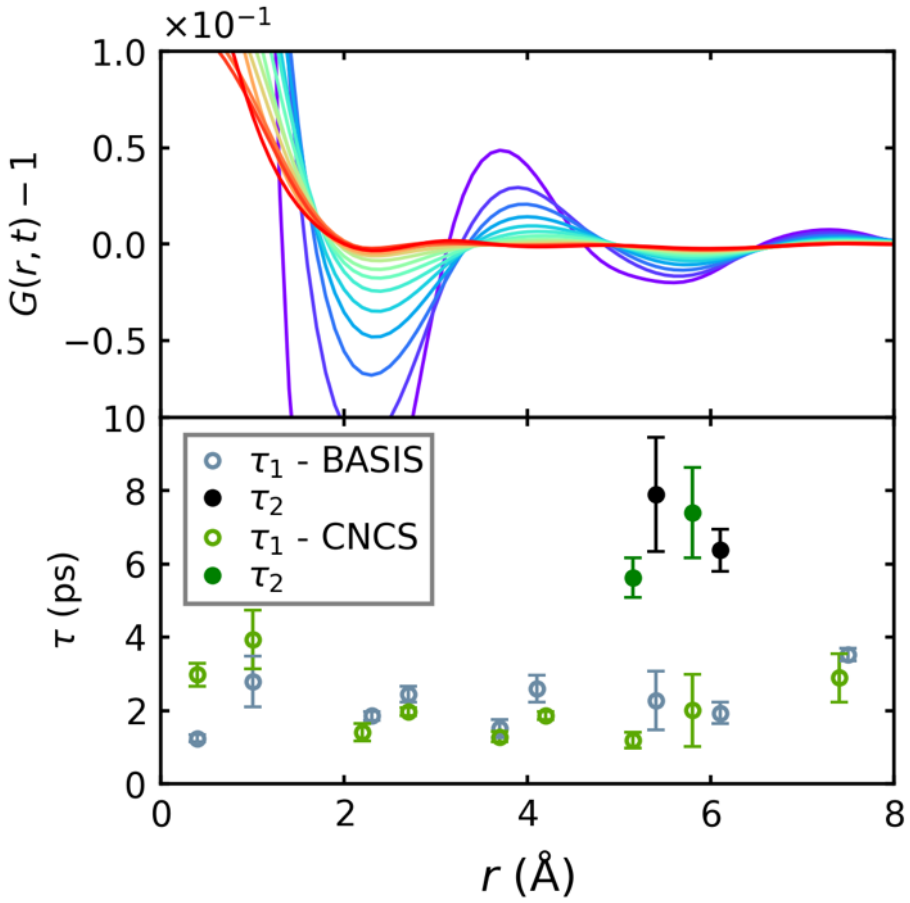

Figure 3.12 The relaxation times estimated at specific regions of space from *G(r, t)*. The time-sliced *G(r, t)* is shown above. green circles represent CNCS data, black circles represent BASIS data

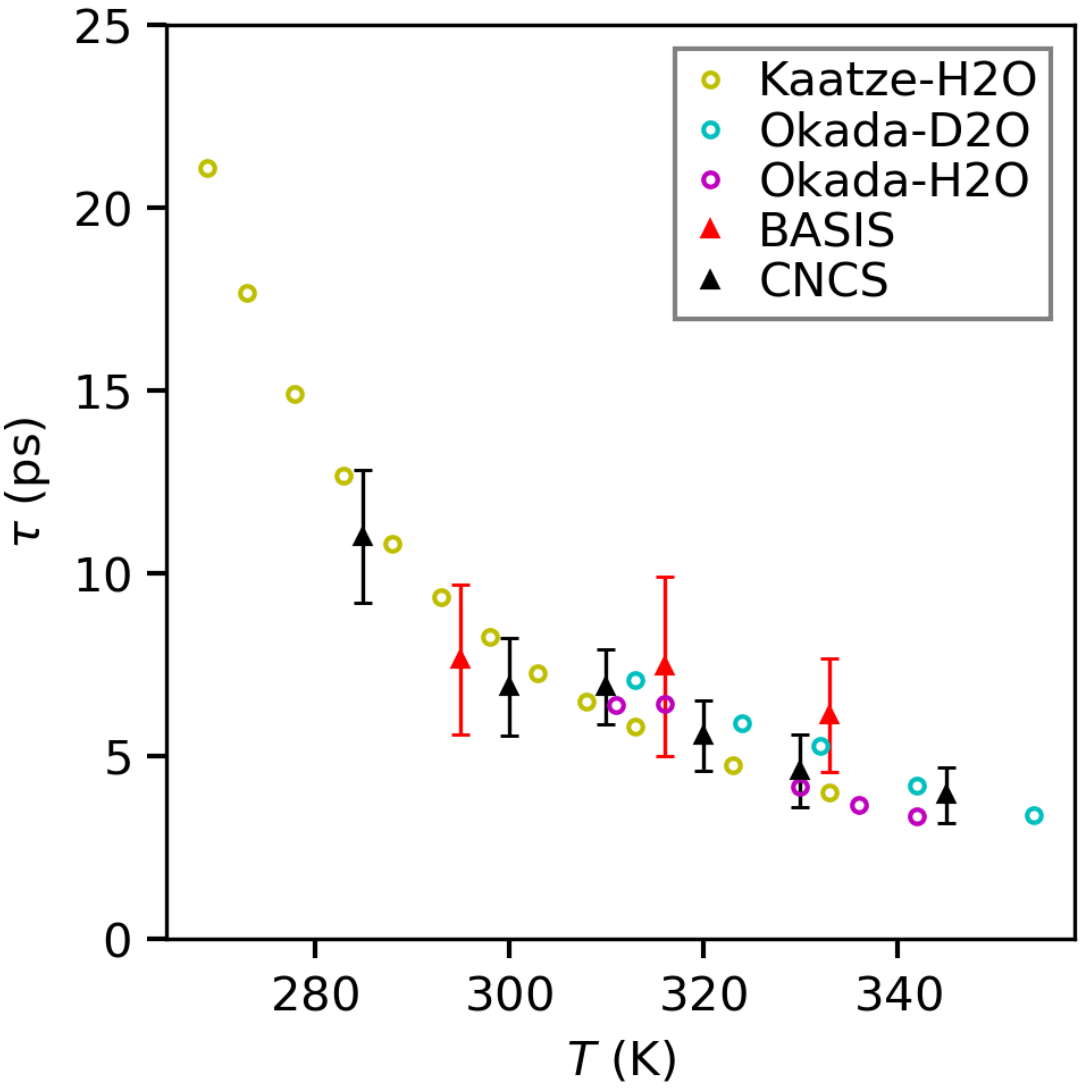

Figure 3.13 The relaxation times from the 5-6 Å in the *G(r, t)* plotted against the previous measurements from dielectric relaxation spectroscopy.

nearest O-O distance, is 2.8 Å in water, this result shows that the Debye relaxation in water does not originate from the molecular rotation as envisaged by Debye. It involves collective dynamics of several water molecules. The arrangement of molecules in bulk water is governed by the 'ice rules' (Bernal–Fowler rules),[83, 84] which states that each oxygen atom is connected to four hydrogen atoms, two by covalent and the other two by hydrogen bonds. The rule maintains the presence of a hydrogen atom between any two oxygen atoms. For this reason, water molecules are not free to rotate, because an O--H bond cut to rotate the molecule has to be compensated by forming another O--H bond. However, such a successive bond transfer, H^+ and OH^- ions transfers between different water molecules through the hydrogen bond network resulting in proton transfer, can occur rapidly, known as the Grotthuss mechanism[40, 85]. Such rapid transport explains the remarkable differences in the diffusion rates of protons and hydroxide ions compared to the other common ions in water, such as Na^+ or Cl^- [40]. In particular this can occur inside the ring structure of $(OH)_n$ [86-89]. If the ring is symmetric, as in crystalline ice, the transfer does not change the total dielectric polarization. But in liquid water the ring lacks symmetry, and the collective rotation of protons in the ring changes polarization, and can respond to external electric field. Such a collective transport in the 5 – 7 member rings could explain the observed relaxation at the 5 – 6 Å range.

Table 3.1 SPC/E model parameters

Model parameters	Value
σ (L-J)	3.16 Å
ϵ (L-J)	0.65 kJ/mol
r_{O-D}	1
D-O-D angle	109.47°
Charge on oxygen (q_O)	-0.8476e
Charge on hydrogen (q_D)	+0.4238e

Molecular Dynamics Simulation of Water Dynamics

Van Hove function from Classical MD simulations

Classical molecular dynamics (MD) simulations were performed to interpret the experimental results using the rigid, extended Simple Point Charge (SPC/E) model of water and the ReaxFF model.[34, 36] The SPC/E model contains three fixed-point charges at each atoms. A single cut-off is used for both the Lennard-Jones and the real-space part of the Coulomb interactions. The model parameters are shown in **Table 3.1**. The simulation system consisted of 8000 water molecules in a cubic box length of 62 Å. Simulations were carried out using the Large-Scale Atomic/Molecular Massively Parallel Simulator (LAMMPS)[90]. The simulation systems were cubic boxes with periodic boundary conditions under NPT ensemble and simulation timestep of 1 fs. The molecules were kept rigid using the SHAKE algorithm[91, 92]. The system was equilibrated for 6 ns before measuring the particle trajectories to calculate the *G(r,t)*. The partial Van Hove functions can be estimated from simulations for each pair of atoms, O-O, O-D, and D-D. Based on the Faber-Ziman formalism, these partial Van Hove functions were weighted based on the each pair's neutron scattering cross-section to simulate the neutron Van Hove function from heavy water. The contribution to the total Van Hove function from each pair correlations are 0.09 for O-O correlations, 0.49 for D-D correlations, 0.42 for O-D (or D-O) correlations. The *G(r,t)* is calculated for a cutoff distance of 10 Å, thus correlations beyond that distance are not considered. The total *G(r,t)* of heavy water is shown in **Figure 3.14**. The relaxation time is estimated from *G(r,t)* by fitting the peak/valley decay using an exponential decay function; $A(t) = A_1 e^{-t/\tau_1} + A_2 e^{-t/\tau_2}$. The fitting results are shown in

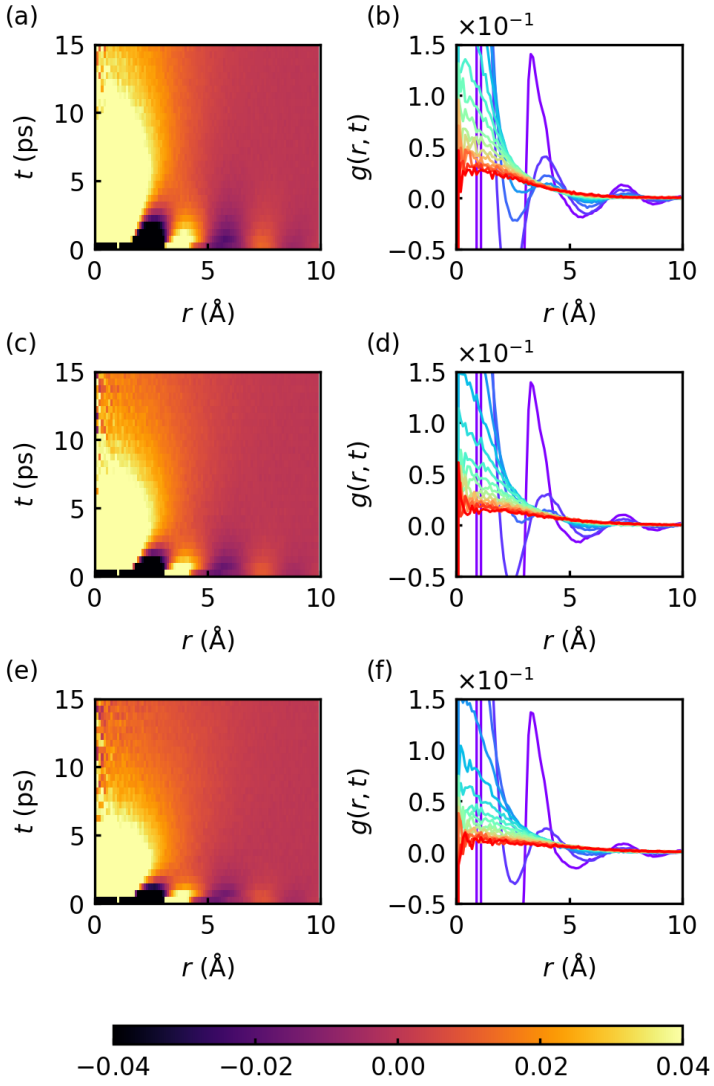

Figure 3.14 2D intensity plots of Van Hove function from classical MD simulations. 295 K (a, b), 315 K (c, d), and 333 K (e, f)

Figure 3.15. The molecular dynamics simulation of the Van Hove function of water with classical force fields shows that the *G(r,t)* decays uniformly fast with the relaxation times in the order of 2 ps across all regions of space as seen in figure. Classical models did not reproduce the long relaxation time in the range of 5 – 6 Å. Therefore, it is most likely that the relaxation in range of 5 – 6 Å is highly quantum-mechanical, involving proton tunneling as expected for hydrogen bond.

Ring Statistics from Graph Theoretical Principles

A ring statistics analysis is performed using the SPC/E water model. In this calculation, the presence of a hydrogen bond is established based on the 'Chandler-Luzar' criteria.[93] These rules specify that two specific criteria need to be met for a hydrogen bond to exist between a pair of molecules, 1) The oxygen – oxygen distance be less than 3.5 Å, 2) the angle between the vector connecting the two oxygen atoms and the vector representing any O-H covalent bond be less than 30°. This newly formed simple network of water molecules connected by hydrogen bonds are analogous to the mathematical concept of a 'graph'. In this graph system, the water molecules are the 'vertices', and the hydrogen bonds connecting them are the 'edges'. The system can then be studied using graph theoretical and computational algorithms.[94] I utilize the Depth First Search (DFS) method, which helps to calculate the total number of '*n*-rings' in the system, where *n* represents the number of molecules forming the specific ring. The code is provided in the Appendix. By performing the DFS algorithm in the graph structure formed by 1000 water molecules, we estimated the number of *n*-rings present in the system as seen in **Figure 3.16**

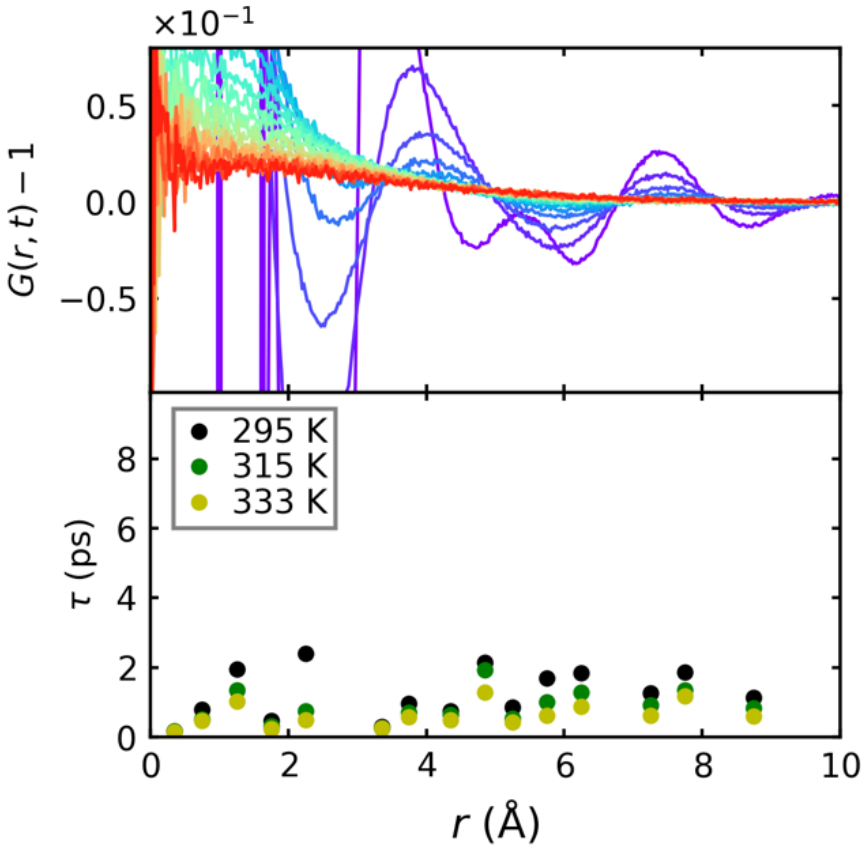

Figure 3.15 Relaxation times of *G(r, t)* as a function of *r* from classical MD simulations.

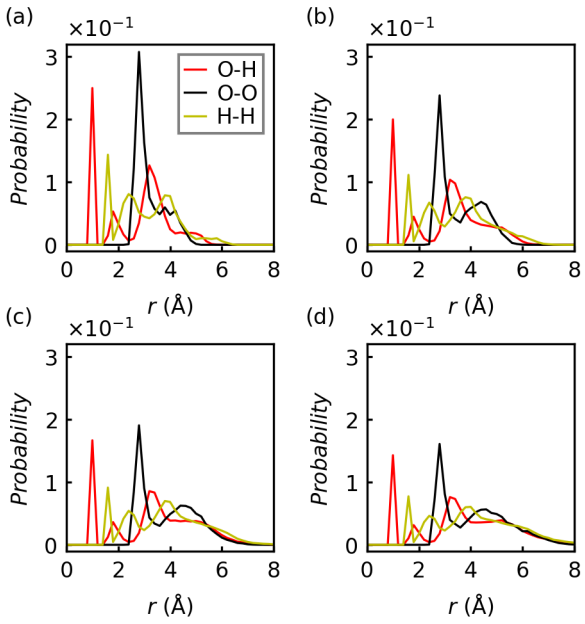

Figure 3.16 Intra-ring correlations from a) 4, b) 5, c) 6, and d) 7 numbered rings from classical MD simulations

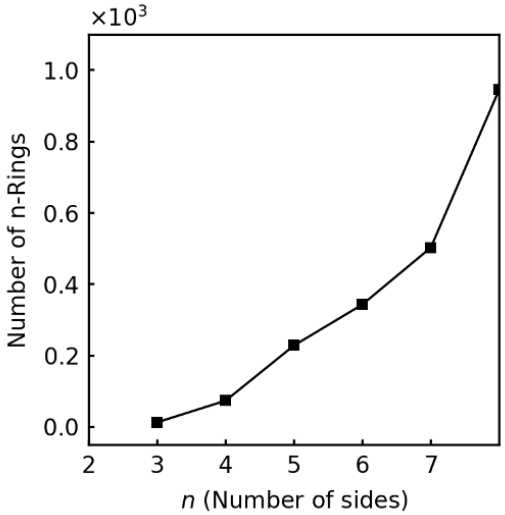

Figure 3.17 The number of 'n-rings' present in the graph system of 1000 water molecules.

and **Figure 3.17**, and identified the individual molecules constituting the ring structures. From these data, the partial pair correlation functions specific to the different *n*-rings are calculated, where n = 4, 5, 6, and 7. We can see in **Figure 3.16** that all the partial correlations have contributions in the 5-6 Å spatial range for rings with $n = 6 \pm 1$. This points to the possibility that the slower-relaxation emerging from the experimental Van Hove function may be traced back to the prevalence of these ring structures in water. The absence of any strong signal (peak/valley) from any particular correlations are discouraging for our hypothesis. However, since the slow relaxations are absent in the MD Van Hove functions from SPC/E model, this is not a compelling evidence to prove/disprove our hypothesis of the existence of ring structures in water. Therefore, we utilize a different simulation model where the water molecule can dissociate and facilitate a transfer of ions/protons across the ring structures and estimate the relaxation times from the Van Hove function of the system which I will discuss in the final section of this chapter.

Dipole-Dipole Correlations of Water from Classical MD simulations

The dipolar correlations in water is investigated using the SPC/E model. The radial dipole-dipole correlation function, $F(r)$, is defined as

$$F(r) = \frac{1}{N}\left\langle \sum_i \frac{1}{n_i(r)} \sum_{j=1}^{n_i(r)} \left(\hat{\boldsymbol{\mu}}_{\boldsymbol{i}} \cdot \hat{\boldsymbol{\mu}}_{\boldsymbol{j}}\right) \right\rangle,$$

where $n_i(r)$ is the number of molecules within a distance r and $r + \delta r$ from molecule i, and $\hat{\boldsymbol{\mu}}$ is the normalized dipole moment of a molecule, and *N* is the total number of dipoles in the system. The system consisted of 1000 water molecules equilibrated for 5 ns, and the coordinates are obtained as a function of the time. The radial dipole-dipole correlation

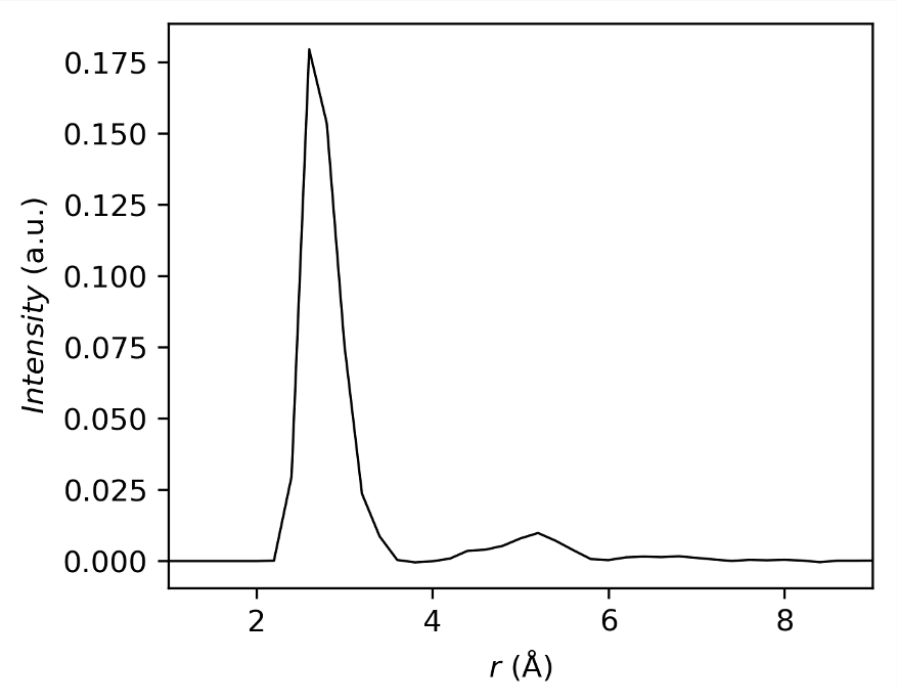

Figure 3.18 Radial dipole-dipole spatial correlation function, *F(r)*, of liquid water at 300 K and P = 1 atm.

function is estimated from the trajectories for 300 K and shown in **Figure 3.18**. We observe that the two prominent peaks are revealed, a sharp peak at ~ 2.8 Å and a broad peak between 4 Å and 6 Å. The first peak represents the dipolar correlations between the nearest neighbors, whereas the second peak shows the correlations from the next-nearest neighbor shell and beyond.

MD Simulation of Water using ReaxFF model

To explain our observation that the spatial signature of the dielectric relaxation of water appears at 5-6 Å, we propose a proton transfer mechanism involving a ring of 6 water molecules as shown in **Figure 3.19**. Proton transfer is a highly quantum mechanical phenomenon, which cannot be modeled using typical classical molecular dynamics simulations. However, by imposing certain constraints which sustains the ring structure for a longer period, we can observe the dielectric signature of water in real-space. The rigid water models such as SPC/E do not allow the dissociation of water molecules, therefore each hydrogen stays in the same molecule for the entirety of the simulation. The ReaxFF model employs bond order dependent potentials that enables the chemical reaction analysis of a system.[35, 36] The total energy of the system is given as the sum of bonded and non-bonded potential energies. The non-bonded energies are associated with the Coulomb and van der Waals interactions between atoms. The energies from bonded interactions correspond to terms representing bond, penalty of over-coordination, under-coordination stability, torsion, valence angle, and lone pair in the model.[36] ReaxFF can simulate bond dissociation in water, and with the help of other LAMMPS utilities, help us create a system motion so that the ring was artificially kept throughout the simulation. The distance

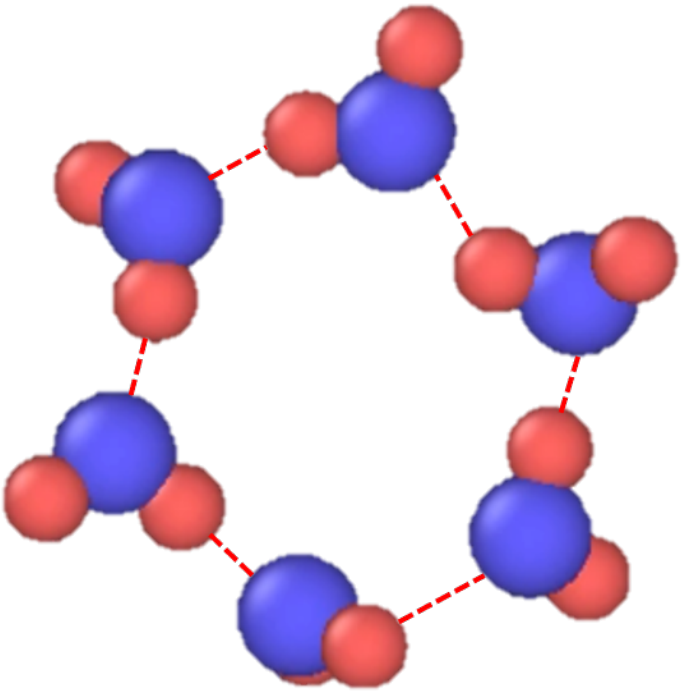

Figure 3.19 6 water molecules forming a 2D hexagon. The red dash line represents the hydrogen bond. Oxygen atoms are blue and hydrogen atoms are red.

of water molecules that provides and atomistic relaxation mechanism. A structure $(OH)_6$ is created as the initial configuration in a cubic box of length 9 Å (input files can be found in the Appendix). Using the 'real' units and 'full' atom-style in LAMMPS, the configuration was equilibrated for 500 ps. ReaxFF was assigned as the inter-atomic potential using the 'pair_style' command. A 'freeze' fix was applied to the oxygen atoms to restrict their between the oxygen atoms were kept at 2.3 Å. This was required to facilitate the 'tunneling' of hydrogens through the ring network. The equilibrated configuration was collected using the 'write_data' command and used for simulations at different temperatures. The simulations were run for 5 temperatures, 375, 405, 435, 465 and 500 K. The Van Hove function was estimated from the coordinates of the hydrogen atoms for every 0.1 ps for 150 ps, collected using the 'dump' command in LAMMPS. The relaxation times were estimated by fitting an exponential function across all the distances in the Van Hove function as shown in **Figure 3.20**. The relaxation times from the VHFs were found to be increasing as a function of distance, with the maximum relaxation time located close to the diameter of the ring structure, which is 4.6 Å as seen in **Figure 3.21**. Note that we had reduced the inter-molecular separation to be 2.3 Å instead of 2.8 Å to decrease the energy barrier for proton tunneling. Therefore, in the normal situation, the maximum relaxation time would have manifested at 5.6 Å, which coincides with our experimental observation from inelastic neutrons scattering measurements. Considering the fact this is an idealized system to re-create a specific structure, the temperatures do not have the regular meaning. Therefore, we use a scaled temperature ($T_c=T/c$, with an arbitrary scaling factor $c=1.5$) while comparing the temperature dependent relaxation times with the experimental values.

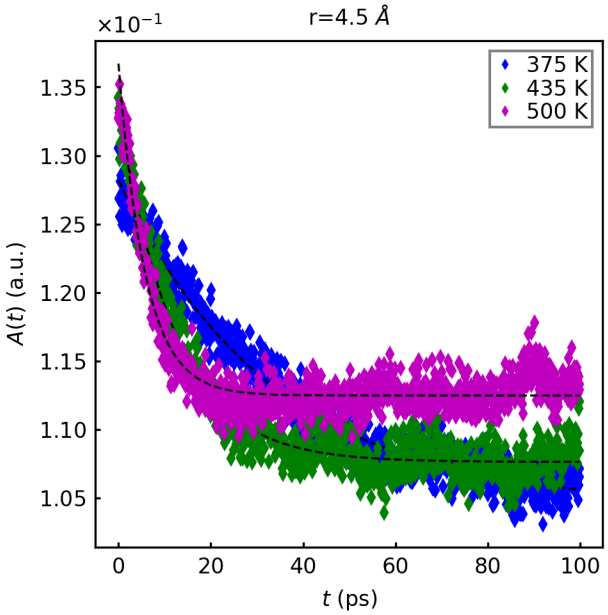

Figure 3.20 The relaxation time estimation technique from hydrogen Van Hove functions at different temperatures.

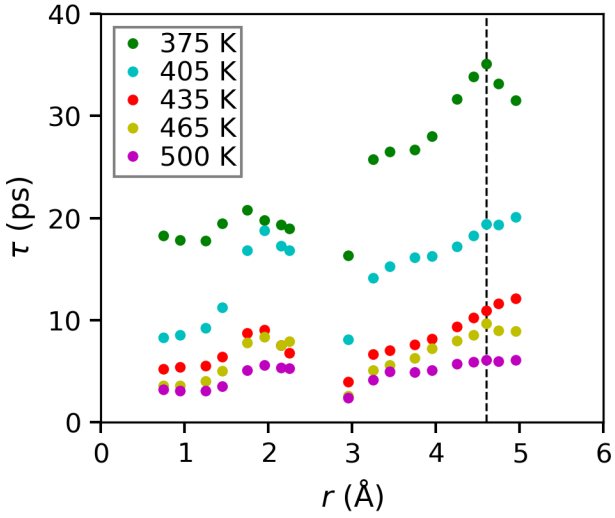

Figure 3.21 The relaxation times from the Van Hove function as a function of the distance.

The relaxation times from the simulation are plotted against the scaled temperature along with our experimental findings and previous dielectric measurements using dielectric relaxation spectroscopy in **Figure 3.22**. We observed a remarkable agreement between the simulation and the experimental values. This supports our hypothesis that the long relaxation observed in the 5-6 Å region of space in the Van Hove function from inelastic scattering measurements are the result of collective proton dynamics involving 6 water molecules.

In summary, we found that the origin of the Debye relaxation in water is a collective dynamics with the spatial range of 5 – 6 Å through the Van Hove function determined by inelastic neutron scattering measurements. The results contradict the belief that the dielectric relaxation mechanism in water involves the rotation of a single molecule and is purely diffusive in origin. We speculate that the $n = 6 \pm 1$ ring connectivity of water supra-molecular structure, which permits a collective reorientation of molecules and cooperative proton tunneling might be a key mechanism in triggering the dielectric relaxation phenomenon in water.

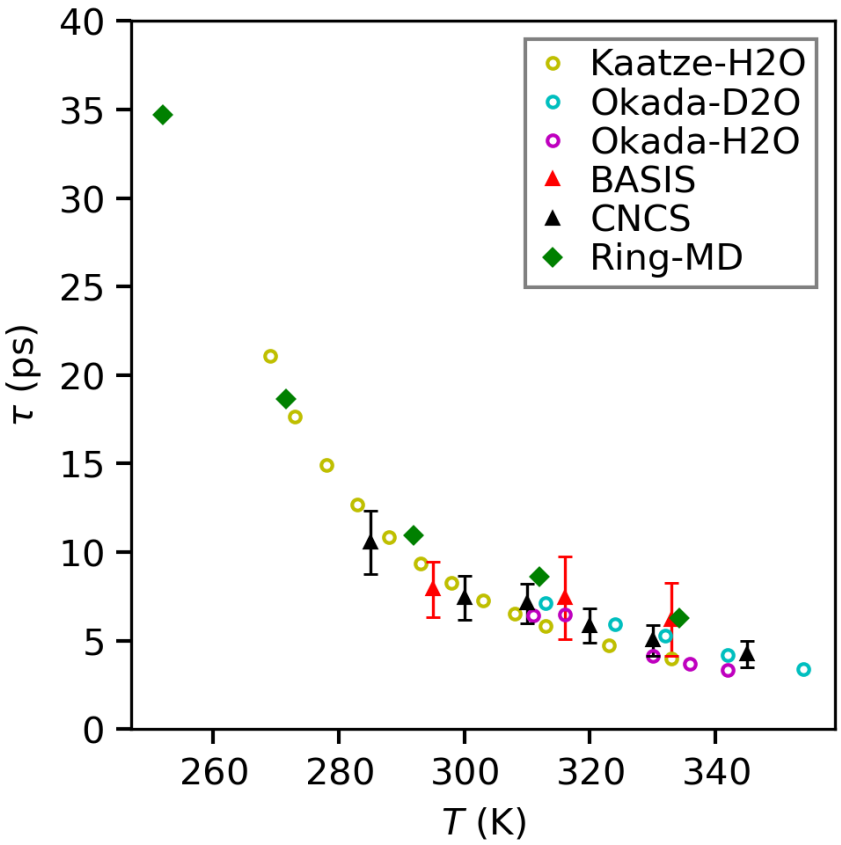

Figure 3.22 The relaxation times estimated from ring dynamics of the hydrogen atoms in comparison to the relaxation times from inelastic neutron scattering experiments and previous measurements using DRS.

CHAPTER 4 CORRELATED DYNAMICS IN LIQUID GALLIUM

Dynamics in Metallic Liquids and Gallium

The macroscopic relaxation time in liquids, also known as the Maxwell relaxation time, τ_M, is connected to the shear viscosity of the system by the Green-Kubo relations, $\tau_M = \eta/G_\infty$. The microscopic local configurational excitation time, τ_{LC}, and the macroscopic Maxwell relaxation time, τ_M, were found to be equal above the viscosity crossover temperature) in simple metallic liquids from molecular dynamics simulation studies.[3] This is a fascinating result, which suggests that the proposed Local Configurational Excitations (LCE) are the elementary excitations in high temperature metallic liquids[3]. The LCE is described as the cutting or forming of a bond, with a characteristic relaxation time, τ_{LC}, which is the time it takes for an atom to lose or gain one nearest neighbor. The crossover behavior of viscosity may now be characterized by the divergence of the ratio τ_M/τ_{LC} from unity. This prediction was later verified in simple metallic liquids (*CuZr*, *CuZrAl,* and *ZrPt)* by inelastic neutron scattering measurements.[47] The generalization of this behavior across different types of liquids would lead to a unification of the dynamical behaviors of all liquids. Through the present work, we study whether this behavior generalizes to different types of liquids. For our purposes, the 'type' of a liquid is characterized by the nature of the atomic bonding present in the system, such as covalent, metallic, or a hybrid of both. The metallic bonds are non-directional, thus at higher temperatures, atomic packing dominates the bond-influenced dynamics. Conventionally, a metallic bond is characterized by utilizing the pair-distribution function (PDF), and by extension, we use the Van Hove function to describe a metallic bond. This is done by finding the distance at which the first minimum (which separates the first and

second peak) in a PDF, which provides the range of distances between nearest neighbors in liquids. This technique is useful in obtaining the structural and thermodynamical information about the system. Additionally, there are lot of efforts made to derive the inter-atomic potential from the PDF method. The metallic bonds are non-directional, as opposed to the covalent bonds, which are strictly bi-directional, that exist in liquids such as water and silica. Earlier studies have shown that the atomic/molecular motions are highly correlated in covalent liquids such as water, whereas the correlations in simple metallic systems such as *ZrPt* and *ZrCuAl* are weaker due to their high coordination number.[7, 18, 48, 95] In this work, we intend to study the changes in liquid dynamics originating from the differences in bonding interactions existing in a system. Towards that goal, we focus on a system that exhibits a mixed nature of bonding – partly covalent and partly metallic, Gallium. Elemental gallium exhibits many fascinating properties, such as its low melting point (303 K), and a density anomaly similar to what is observed in water and silica.[96, 97] It expands upon solidification and strongly tends to supercool below its melting point. Covalent dimers have been observed near the melting point in liquid Gallium exhibiting its mixed nature of bonding.[98] We perform inelastic neutron scattering studies on liquid gallium with the dynamics shown in real-space to extend our understanding of a possible universal dynamical behavior of liquids.

Neutron Van Hove function of Liquid Gallium

The local atomic dynamics of gallium is studied by collecting the dynamic structure factor, *S(Q, E)* from inelastic neutron scattering measurements. In general, the *S(Q, E)* of crystalline solids contains well-defined peaks and dispersion relations representing the

collective excitations such as phonons. However, due to disorder and the highly dynamical nature of liquids, liquid *S(Q, E)* contains diffused peaks which are mostly quasi-elastic. Although *S(Q, E)* contains the microscopic structure and dynamical information of a liquid, its interpretation remains a challenge. To remedy this, we determined the Van Hove function of liquid gallium by double Fourier transforming the neutron *S(Q, E)* to real-space and time. The inelastic measurements of liquid Gallium were carried out at ARCS at the Spallation Neutron Source. 18g of 99.9% pure gallium was loaded into a vanadium container with a radius of 4 mm and height 6 cm. The container was sealed with a titanium lid. The sample was top loaded into a MICAS furnace at BL-18 ARCS. A vanadium rod was used to correct the instrumental energy resolution when transforming the inelastic *S(Q, E)* to *F(Q, t)*. A wide range of temperatures were chosen to include the viscosity crossover behavior, ranging from 310 K to 950 K. The sample was heated to 400 K to melt the gallium crystal completely, then cooled back to 310 K to start collecting the data. We obtained the scattering data for three incident energies, 20, 40 and 80 meV. Due to the kinematic restriction of neutron scattering, the momentum transfer range is limited by the incident energy. The finest energy resolution is obtained from the 20 meV data, which has a relatively limited *Q*-range. The higher energies of 40 and 80 meV have poor energy resolution, but they provide a wider *Q*-range, which is sufficient for an accurate transformation of the data from *Q*-space to real-space in the form of the Van Hove function, *G(r, t)*. Our solution to combine *S(Q, E)* data from the different incident energies and form a master spectrum with a wider *Q*-range and a finer energy resolution. An empty sample measurement was carried out to subtract background. The 2D intensity plot of *S(Q, E)* after

the background subtraction is shown in **Figure 4.1**. The background subtraction is performed by determining the Self-Shielding Factor (SSF = 0.8) for the sample in the specified geometry using the DAVE software package[99]. The *S(Q, E)* is converted to *F(Q, t)* by Fourier transforming over the energy transfer range. The energy resolution of ARCS is measured by measuring the *S(Q, E)* of a standard Vanadium rod at 310 K. The $F_{rf}(Q,t)$ of the Vanadium rod is calculated in the same fashion and used to correct the resolution of the instrument.

$$F(Q,t) = \frac{F_{total}(Q,t)}{F_{rf}(Q,t)},$$

where $F_{\mathrm{total}}(Q,t)$ is the intermediate scattering function obtained after the background subtraction. $F_{\mathrm{rf}}(Q,t)$ is the resolution function calculated from the empty Vanadium container, and $F(Q,t)$ represents the resolution corrected function ready to be Fourier transformed to $G(r,t)$. The 2D intensity plot of *F(Q, t)* is shown in **Figure 4.2**. Understanding the dynamics of liquids in *Q*-space have been carried out using quasi-elastic and inelastic neutron measurements in the past, however, these dynamical studies were focused on understanding the diffusive behavior of molecules. Explaining correlated dynamics of liquids using *Q*-space analysis is flawed because there is no one-to-one correspondence between the real-space and *Q*-space. Therefore, the widely adopted usage of α-relaxation time to explain dynamical behaviors is incorrect.[55] The α-relaxation time is measured from *F(Q, t)* at $Q = Q_0$, where the maximum of the function is located at. In our approach, we analyze the dynamics in the real-space using the Van Hove function to interpret the correlated dynamics of gallium. *G(r, t)* of gallium is estimated by Fourier transforming the *F(Q, t)* over a wide *Q*-range. The 2D intensity plot of *G(r, t)* is shown in

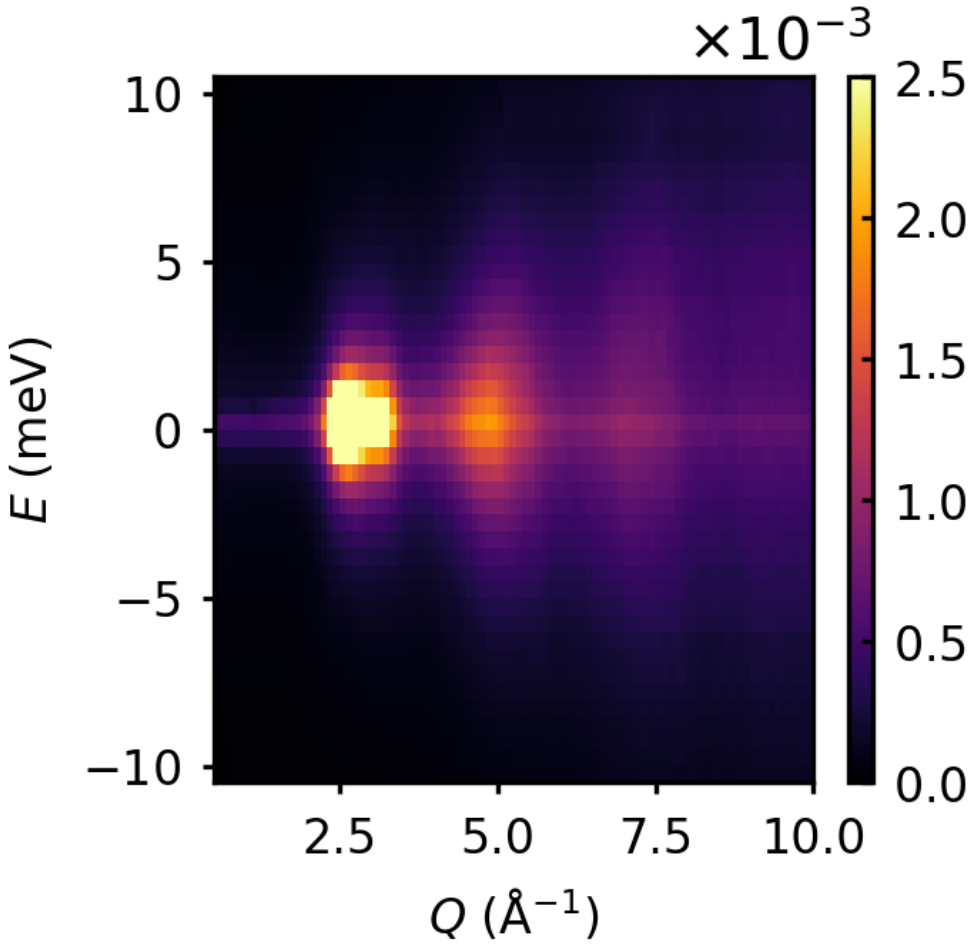

Figure 4.1 The *S(Q,E)* of liquid gallium at 310 K from for E_i = 80 meV

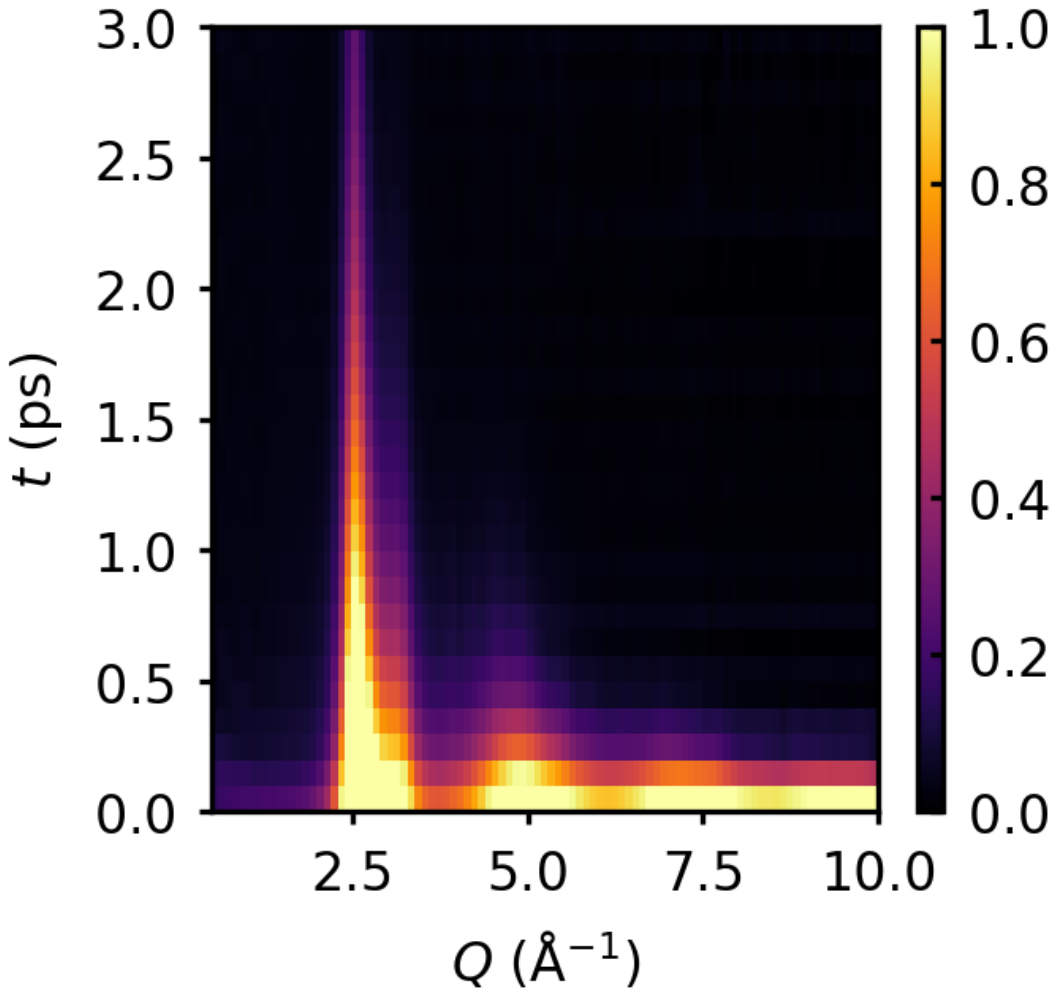

Figure 4.2 *F(Q, t)* of liquid gallium at 310K obtained by Fourier transformation of *S(Q,E)* over the energy range

Figure 4.3, and the time-sliced *G(r, t)* in Figure **4.4**. The first peak of the *G(r,t)* at $r =$ 2.8 Å describes the nearest neighbor environment, which is in agreement with *g(r)* from x-ray and neutron diffraction studies.[100] The nearest neighbor peak is broader compared to the sharp peaks seen in the static pair-distribution functions from diffraction measurements, this is due to the narrower *Q*-range available to inelastic neutron scattering (elastic scattering provides Q -range greater than $20\ \text{Å}^{-1}$). Typically, it is customary to use a 'modification' function to help minimize the spurious termination (or truncation) ripples that originate due to the finite range of the scattering data, which is Fourier transformed to obtain the pair distribution function. In this work, we use the Lorch function for that purpose. The first peak of *G(r, t)* represents the correlation between the nearest neighbors in gallium at $r = 2.8$ Å and the second peak represents the next-nearest neighbor correlations, located at $r = 5.4$ Å. The peaks that appear below $r = 2.8$ Å for $t = 0$ are not physical correlations, but artifacts of the Fourier transformation of the data to real-space. The liquid dynamics is studied from Van Hove function by fitting the decay of the area of the peaks corresponding to each specific correlations using the functional form, $g(t) = g_0 e^{-t/\tau}$, where τ is the characteristic relaxation time. Using this approach, the correlated atomic dynamics is measured from the Van Hove function. Similarly, the α-relaxation time is estimated from *F(Q, t)* and shown in **Figure 4.5**. The relaxation of the first nearest neighbor peak determine the τ_{LC}. It is not possible to obtain the microscopic τ_{LC} directly from scattering experiments, therefore we estimate τ_{LC} from molecular dynamics simulations, and compare it with τ_{VHF}, which is the relaxation time estimated from the decay of the first peak of the Van Hove function. Upon comparison, we observe

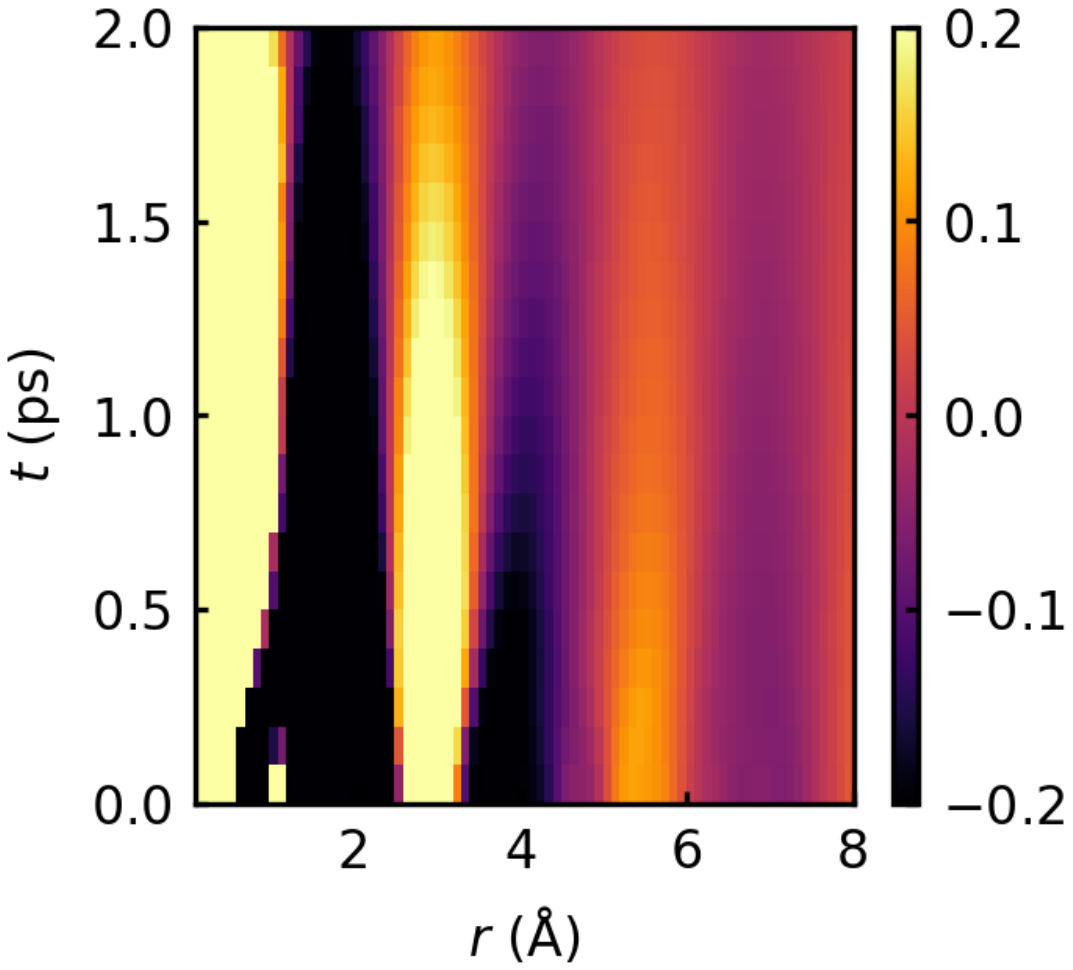

Figure 4.3 Intensity plot of *G(r, t)* of liquid gallium at 310 K.

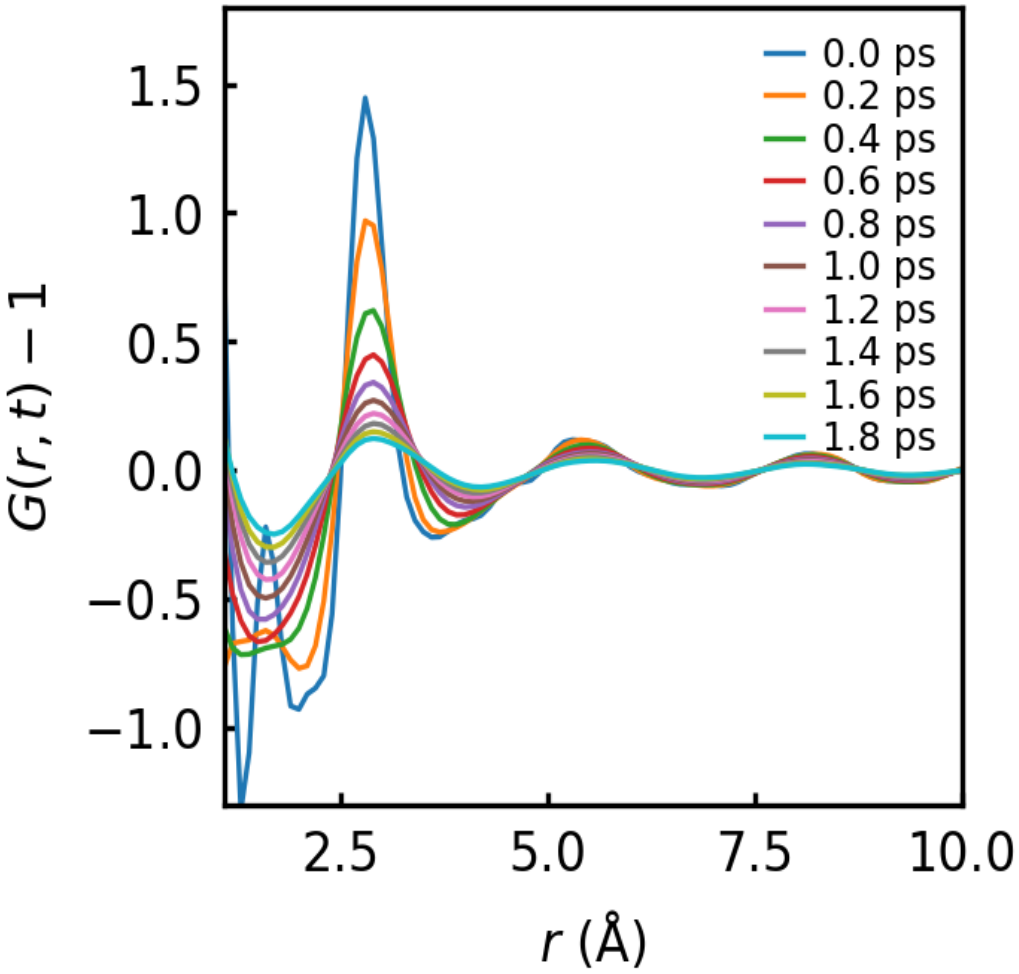

Figure 4.4 The time-sliced Van Hove function of liquid gallium at 310 K.

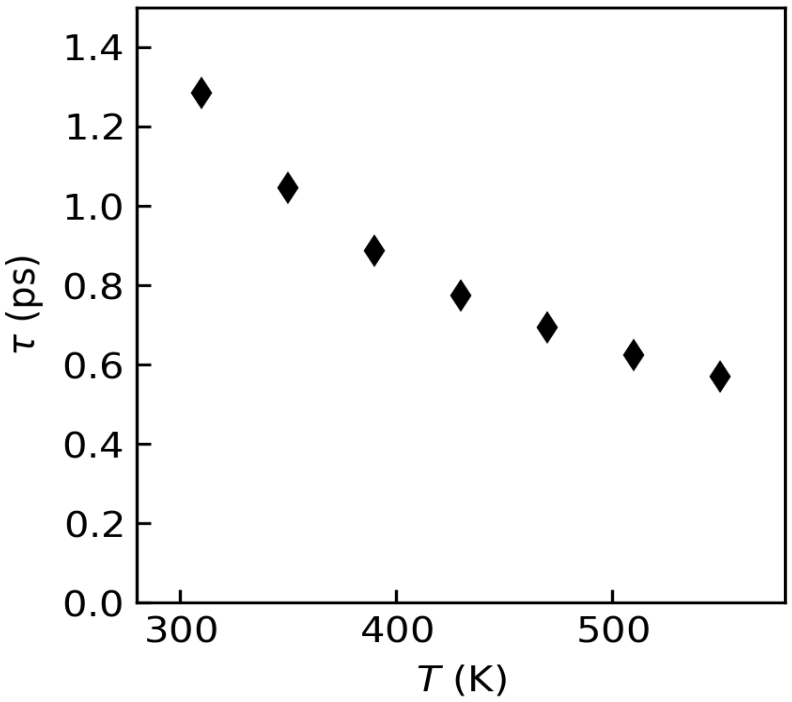

Figure 4.5 The $\boldsymbol{\alpha}$-relaxation time determined from the *F(Q, t)* at $Q=Q_0$, where Q_0 is the momentum transfer value at which the maximum of *S(Q)* occurs.

that the two are linearly connected, which can be seen from **Figure 4.6**. Based on this approach, we are able to establish a method to determine from scattering measurements. The macroscopic relaxation time in liquids, also known as the Maxwell relaxation time, τ_M, is connected to the shear viscosity of the system by the Green-Kubo relations,

$$\tau_M = \eta / G_\infty.$$

The value of the high-frequency shear modulus (G_∞) of gallium is unknown from experiments, this restricts our attempt to calculate τ_M from measurement, despite knowing the viscosity of gallium. Thus, we depend on Ab initio Molecular Dynamics (AIMD) simulations to estimate the Maxwell relaxation time of gallium. τ_M of a liquid is calculated from the shear stress correlations of atoms in the system, given by the Green-Kubo equations of the Fluctuation-Dissipation theorem as,

$$\tau_M = \int_0^\infty \frac{\langle \sigma^{xy}(0)\sigma^{xy}(t)\rangle}{\langle (\sigma^{xy}(0))^2\rangle}\, dt,$$

where $\sigma^{xy}(t)$ is the shear stress at time t. The $\langle \dots \rangle$ represent the averaging of the shear stress across the different cartesian components. Iwashita et al[3] showed that the Maxwell relaxation time was equal to the LCE relaxation time above the crossover temperature in simple metallic liquids, as observed in **Figure 4.7**. The equality of the two relaxation time-scales indicates that the LCE's are the elementary excitations in simple metals above T_A. This suggests that the breaking or forming of a metallic bond quantifies the viscosity of the system. A quantitative estimate proving the existence of that process is a key step in the search for the origin of viscosity in liquids. The breaking/forming of a bond would change the atomic-level stresses for the atoms involved because the atomic connectivity is tightly

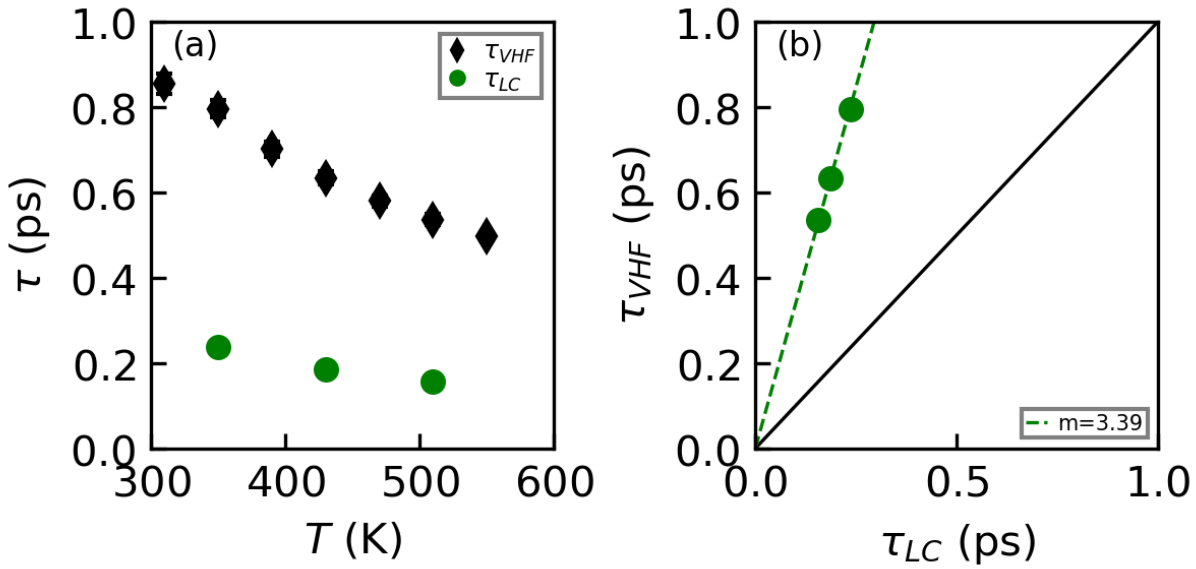

Figure 4.6 (a) The relaxation time evaluated from the first peak of the Van Hove function ($\boldsymbol{\tau_{VHF}}$) and the local configurational relaxation time $\boldsymbol{\tau_{LC}}$ from MD simulations. (b) The relation established between $\boldsymbol{\tau_{LC}}$ and $\boldsymbol{\tau_{VHF}}$.

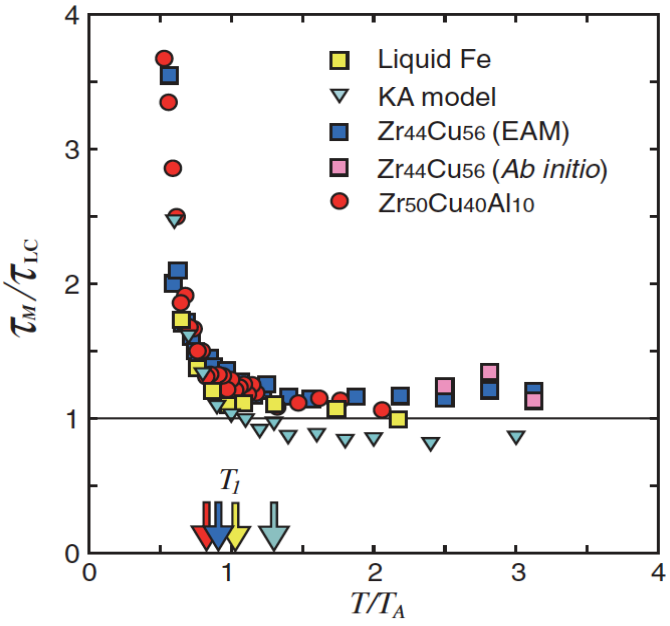

Figure 4.7 The ratio $\boldsymbol{\tau_M/\tau_{LC}}$ plotted against $\boldsymbol{T/T_A}$ for different MD models of simple metallic liquids. $\boldsymbol{\tau_M}$ is found to be approximately equal to $\boldsymbol{\tau_{LC}}$ above $\boldsymbol{T_A}$.[3]

linked to the atomic stresses.[101, 102] At lower temperatures (T < T_A), this empirical observation does not hold true. The rapid divergence of the ratio τ_M/τ_{LC} above $T_A$from unity suggests a temperature dependent cooperative behavior for simple metals. Above T_A, τ_{LC} is possibly too short to influence the neighboring atoms other than the two atoms involved in the bond[3], but for $T < T_A$, the value of τ_{LC} is sufficiently long enough to support a dynamics stress-field interactions between the LCE's, which might be the reason behind the rapid divergence of the relation between the two time-scales in that regime.[3]

Ab Initio Molecular Dynamics Simulation of Gallium

Extending the approach of comparing the relaxation behaviors to a partly covalent liquid like gallium, which is claimed to exhibit covalent dimers near the melting point and possesses significantly stronger bonds, can help us understand if this behavior extends to all liquids, along with understanding the role of LCE's in covalent liquids. For this purpose, we perform AIMD simulations to obtain the Maxwell relaxation time of gallium. The AIMD simulation of liquid gallium is carried out using the Vienna Ab-initio Simulation Package (VASP)[103]. VASP is a computer program to perform electronic structure calculations based on principles from quantum mechanics. The ground state electronic structure of gallium is calculated by using Density Functional Theory. In DFT, the properties of a many-electron system are calculated from the spatially dependent electron density. The VASP simulation generates the liquid configurations of Ga at and temperature T = 350 K, 430 K, and 510 K. The number density ρ was kept at the value 0.053 $Å^{-3}$, which is the experimentally determined value for liquid gallium. The simulation were run

for 256 Ga atoms contained in a cubic box with its length set at 29.38 Å, with periodic boundary conditions applied.[104] For electronic structure calculation, a projector augmented wave (PAW) potential in the local density approximation was utilized. The electronic wavefunctions of the system were represented by plane waves with an energy cutoff at 134.6 eV. The initial atomic configurations were obtained from classical molecular dynamics simulations using the MEAM potential in LAMMPS[105]. The atomic configurations of the system after reaching the thermal equilibrium were used as the initial conditions to the VASP simulation. The volume of the simulation box was kept constant under the NVT ensemble. The system was completely melted at 950 K to reach thermal equilibrium, then cooled to other low temperature points using the Nose-Hoover thermostat. The simulations were run for 100 ps with a time-step of 3 fs. The time dependent atomic positions of the system were then used to estimate the Van Hove functions of gallium. The cut-off distance for correlations were arbitrarily set at 10 Å, thus correlations between atoms that are spaced beyond the cut-off will not contribute to the VHF. The configurations of the system were collected after the equilibration at each temperature of interest.

Ab-initio molecular dynamics (AIMD) simulation provided the time-dependent coordinates and velocities of the atoms, which fully describes the atomic environment in liquid Gallium. τ_M is estimated by following the shear stress correlations in the system. The Van Hove function is measured from the atomic trajectories as a function of time. The coordination number of each atom can be estimated by counting the number of nearest

neighbor atoms from the Van Hove function. The radial distribution function, which is defined as

$$R(r) = 4\pi r^2 \rho_0 g(r),$$

when integrated over the first peak provides the coordination number of the system. When *g(r)* is substituted with its generalized time-dependent function, the Van Hove function *G(r, t)*, the resulting time-dependent radial distribution function describes how the coordination number changes as a function of time. The temporal change in coordination number signifies the change in the initial atomic environment of an atom. In other words, how many initial neighbors remain a neighbor as the atomic correlations evolve in time. τ_{LC} is defined as the time it takes for the coordination number to drop from N to $N-1$. **Figure 4.6 (a)** shows the estimated τ_{LC} and τ_{VHF} for gallium. We show that τ_{LC} and τ_{VHF} are linearly related by plotting the values of both quantities corresponding to each temperature in in Figure 4.6 (b), with the relation being $\tau_{LC} \sim \frac{1}{3.4}\,\tau_{VHF}$. This was also observed for other systems such as simple metals and water, albeit with a different scaling constant. In the case of water, $\tau_{LC} \sim \tau_{VHF}$,[48] for simple metals, $\tau_{LC} \sim \frac{1}{4}\,\tau_{VHF}$. This result hints that the dynamics of gallium lies in between the extremes of either types of systems. Thus, we have established a way of estimating the microscopic relaxation time of atomic systems from inelastic scattering experiments. The ratio τ_M/τ_{LC} is plotted against a scaled temperature T/T_G to obtain a universal plot, which can be compared to other liquids and observe how dynamics depend on the nature of bonding in the system, as shown in **Figure 4.8**. There is a marked difference in the values of gallium's values compared to other metallic liquids.[3] The obtained τ_M/τ_{LC} values are lower than unity for every temperature

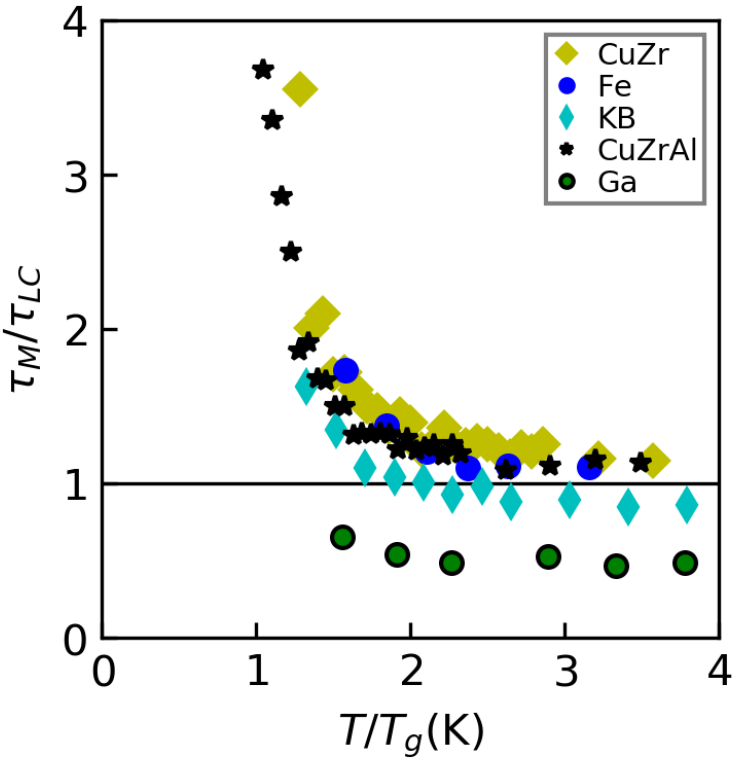

Figure 4.8 The ratio $\boldsymbol{\tau_M/\tau_{LC}}$ for gallium plotted against $\boldsymbol{T/T_G}$ along with the simple metallic liquids.

point and no cross-over in viscosity is obtained. This shows that for gallium, τ_M is consistently lower than τ_{LC}, markedly different from what is observed in simple metals. The results also suggest that the T_A is possibly in the super-cooled liquid regime, which is difficult to probe experimentally. The value of τ_M/τ_{LC} demonstrate that the time it takes to break a bond in liquid gallium is almost as twice as the time-scale of its viscosity. This is counter-intuitive, because by definition, below τ_M a liquid would behave like a solid, based on the definition of τ_M. This strongly points to the possibility that the mixed nature of bonding in the system, with metallic bonds and covalent bonds, might be averaging out the relaxation time, giving τ_{LC} a higher value than is expected. We attempt to define two LCE's in this case, the first an LCE associated with the simple metallic bond between gallium atoms, and the second, an LCE associated to the covalently linked atoms. In contrast to the method of estimation of τ_{LC} from simple metals, the time dependent coordination number change in liquid gallium is fitted with a decay function to quantify the relaxation process involved. We observe that the short time relaxation of the coordination is composed of two relaxation processes, a short process (τ_{LC}^1) of the order of ~ 0.1 ps, and a longer relaxation (τ_{LC}^2) of ~0.8 ps, as shown in **Figure 4.9**. We also needed a slower relaxation as the coordination number requires much longer time (order of 10 ps) to completely relax. Applying the same process with liquid Iron we notice that the short time relaxation is well described by a simple process, agreeing with our hypothesis. Substituting the newly found relaxation time τ_{LC}^1 in place of the τ_{LC}, we obtain the universal plot in **Figure 4.10**, and we find that τ_M/τ_{LC}^1 is closer to unity. We conclude that the atomic environment in liquid gallium is composed of two type of interactions, simple metallic bonding and stronger

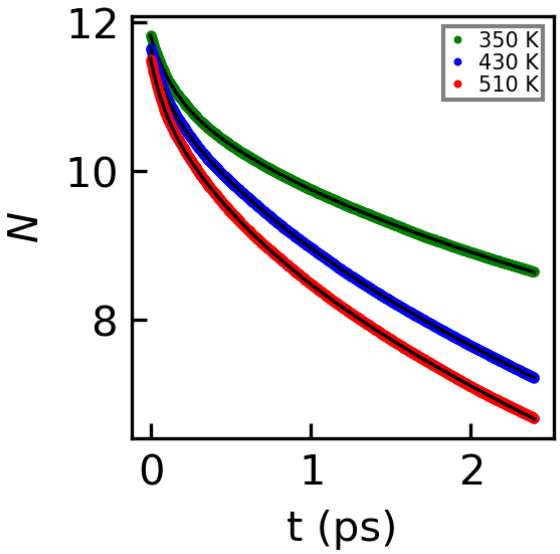

Figure 4.9 The change in coordination number w.r.t time. Three exponential decay functions are used to fit the relaxation. The first two relaxations are $\boldsymbol{\tau_{LC}^{1}}$ and $\boldsymbol{\tau_{LC}^{2}}$. $\boldsymbol{\tau_{LC}^{3}}$ is not shown as it is an order of magnitude greater and irrelevant for the current discussion.

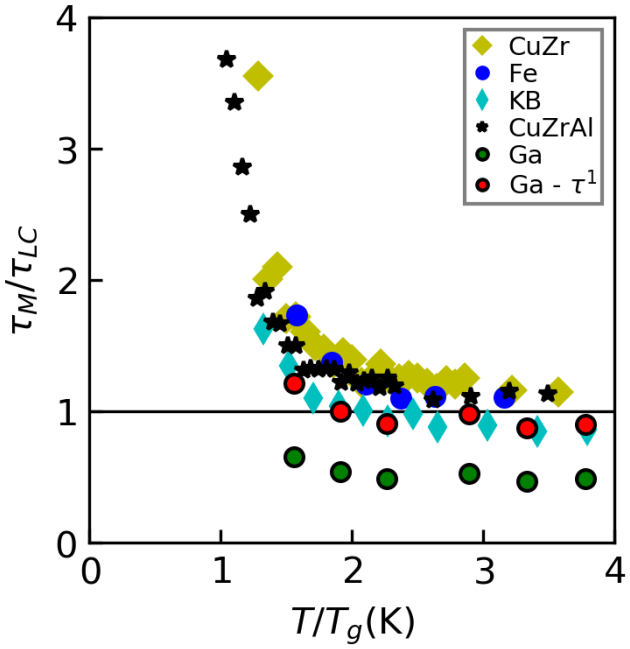

Figure 4.10 Plotting the $\boldsymbol{\tau_M\ /\tau_{LC}^{1}}$ for gallium plotted against $\boldsymbol{T/T_G}$. The green markers are for $\boldsymbol{\tau_{LC}}$ measured by the old approach. The red markers are for $\boldsymbol{\tau_{LC}^{1}}$ estimated by fitting the decay.

covalent bonds with a much longer relaxation time. The origin of viscosity in gallium may still be characterized by the local configurational excitation time, albeit with a slightly modified definition. Characterizing The atomic environment in gallium is not possible with experimental measurements using the Van Hove function as it is a statistically averaged quantity. Ab initio Molecular dynamics simulations can be used to understand and explain this phenomenon further, however that is not attempted yet as part of this work.

CHAPTER 5 CONCLUSION

In crystalline solids, the presence of long-range order in the structure enabled the assumption of translational periodicity, which expedited the theoretical understanding of many solid-state phenomena. Liquids are highly complex systems because of a combination of the absence of long-range order and the highly dynamic atomic environment. Therefore, understanding the microscopic origins of liquid state behaviors is a challenging task. The popular experimental practices for studying the liquid state are diffraction and spectroscopy, which characterize the structure and dynamics of liquids, respectively. However, they are primarily solid-state focused techniques adapted to investigate the liquid state phenomena, and are not fully capable of characterizing liquids. We require techniques purely dedicated to study the liquid state to explore and widen the scope of the physics of liquids.

In my PhD dissertation, the correlated dynamics of liquid state systems have been investigated by performing experimental measurements and computer simulations. The primary experimental techniques utilized was the inelastic neutron scattering technique, which provides the structural and dynamical information of the atomic environment of materials in the bulk at atomic length-scale and picosecond time-scale. Neutrons are charge-less particles, thus they can probe the samples deeper, which makes them an ideal probe for bulk measurements. The proximity of the Spallation Neutron Source at Oak Ridge National Laboratory, which produces the most intense pulsed neutrons in the world for scientific research, have massively helped our efforts to obtain high quality data from the modern neutron spectrometers and study the structure and dynamics of liquids in real-

space. The availability of modern distributed computing systems at University of Tennessee and Oak Ridge National Laboratory was essential in numerically computing the correlated atomic dynamics of liquids.

The structure of a liquid is characterized by the instantaneous pair-distribution function, *g(r)*, extracted from diffraction measurements, but they lack the temporal resolution to study the dynamical nature of liquids. Similarly, the spectroscopic measurements lack the spatial resolution to describe the structural aspects of dynamical excitations. Inelastic scattering has been used to characterize the collective excitations in liquids such as phonons. However, describing liquid dynamics only in terms of phonons is insufficient because phonons are overdamped and marginalized in liquids due to disorder[3]. We need to use techniques designed to study the correlated atomic dynamics of liquids, such as the Van Hove function - a generalized pair distribution function. The correlated dynamics is studied by the Van Hove function *G(r, t)* which provides the two-body correlations in real-space and time. The *G(r, t)* is experimentally determined from the dynamic structure factor, *S(Q, E*), obtained from inelastic scattering measurements, by double-Fourier transforming the *S(Q, E*) over energy and momentum transfers. Although inelastic scattering has been used in the past to understand the structural and dynamical properties of liquids, Fourier transformation of the data to the real-space has rarely been done. This is because in order to obtain reliable *G(r, t*), *S(Q, E*) has to be measured over wide *Q* and *E* transfer ranges, which is a time-consuming process at a Triple Axis Spectrometer. The advent of pulsed neutron sources and synchrotron facilities in the last few decades have dramatically reduced the time to collect the scattering data over wide

momentum and energy transfers. The dynamics is measured from the Van Hove function by fitting the decay of the atomic/molecular correlation peaks/valleys as a function of time to characterize the underlying atomistic processes. Molecular dynamics simulations were implemented to explain the experimental findings using LAMMPS and VASP, which are classical and ab-initio molecular dynamics packages, respectively.

In my dissertation, I studied how the atomic dynamics of liquids is affected by the nature of interactions in the system. Viscosity (η) is a fundamental property of the liquid state, which quantifies the flow of a liquid. Despite decades of research, it remains unclear how the atomic dynamics is connected to the viscosity of the system. A universal crossover behavior of viscosity was observed in simple metallic liquids from molecular dynamics simulations, which implied that the viscosity in liquids were characterized by the local configurational excitations at high temperatures, with a life-time of τ_{LC}.[3] τ_{LC} is defined as the time it takes for an atom to lose or gain a neighbor. This observation was experimentally verified for simple metallic liquids *CuZr*, *CuZrAl*, and *ZrPt*.[47] We studied how this behavior can be generalized to a different type of liquid. Gallium is a metal that exhibits a mixed nature of bonding, partly covalent and partly metallic. By determining the Van Hove function of gallium from inelastic neutron scattering experiments, and combining the results with ab initio MD simulations, we found out that the relaxation time ratio (τ_M/τ_{LC}) remained below unity across the temperature range of measurement. This is in stark contrast to simple metallic liquids where τ_M/τ_{LC} approached unity at high temperatures.[3] Extracting gallium's τ_{LC} corresponding to the metallic interactions was done by fitting its coordination number change with respect to time. This demonstrated that the local atomic

environment in liquid gallium is composed of two types of interactions, simple metallic bonding and stronger covalent bonds with a longer relaxation time. Substituting τ_{LC}^{1} (metallic τ_{LC}) in place of τ_{LC}, we observe that τ_M/τ_{LC}^{1} ratio is close to unity. Thus, the origin of viscosity in gallium may still be characterized by the local configurational excitation time, albeit with a slightly modified definition. This may further be investigated by fully describing the atomic environment in gallium using quantum mechanical computations, which can reveal the microscopic local environment in partly covalent systems such as gallium.

Water is one of the fundamental substances for life on earth, and the most researched compound on our planet. Water possesses many anomalous properties, such as the high freezing/melting point, a density maximum at 4°C, and a high dielectric constant. These behaviors are believed to be originating from the strong hydrogen bond network in water. The dielectric 'Debye' relaxation in water, which is used in the operation of microwave ovens, has been studied for decades using dielectric relaxation spectroscopy (DRS)[59]. However, a macroscopic probe like DRS cannot help elucidate the microscopic mechanisms behind this well-defined relaxation observed in the frequency space. Peter Debye attributed the dielectric relaxation time (~8.3 ps) to be the time-scale of rotation of a water molecule.[60] More recent researches have attributed the Debye relaxation to molecular diffusion controlled by the highly cooperative Hydrogen bond network in water[69]. Microscopic techniques such as quasi-elastic neutron scattering have been utilized to measure the dynamic structure factor of water to elucidate the atomistic mechanism[76]. We measured the Van Hove function from inelastic neutron scattering to understand the

microscopic mechanism behind the dielectric relaxation in water in real-space and time. The results contradict the widely held belief that the dielectric relaxation mechanism in water involves the rotation of a single molecule and is purely diffusive in origin. We found that the origin of the Debye relaxation in water is a collective dynamics with the spatial range of 5 – 6 Å through the Van Hove function determined by inelastic neutron scattering measurements. We speculate that the $n = 6 \pm 1$ ring connectivity of water supra-molecular structure, which permits a collective reorientation of molecules and cooperative proton tunneling might be a key mechanism in triggering the dielectric relaxation phenomenon in water.

Some of the key contributions from my dissertation research are summarized as follows:

1. Designed and performed Inelastic Neutron Scattering (INS) measurements to obtain the dynamic structure factor, *S(Q, E)* with a wide *Q-E* range for water and gallium by utilizing three inelastic neutron spectrometers (BASIS, ARCS, and CNCS) at SNS, ORNL.
2. A comprehensive data processing and analysis procedure were developed in Python to obtain the different pair-correlation functions, including the Van Hove function, *G(r, t)* from INS data. Implemented algorithms to calculate the Van Hove function, the dipole-dipole correlation function, and to perform ring-network analysis in liquids based on graph theoretical principles.

3. Performed classical MD simulations of water and gallium using LAMMPS and analyzed the data to explain experimental findings from inelastic scattering measurements.

The significance of the usage of Van Hove function in investigating liquid state phenomena is strongly demonstrated through my dissertation research. Significant progress was achieved in understanding the dielectric relaxation mechanism in water using inelastic neutron scattering measurements. We stress that further investigations using Quantum Monte-Carlo simulations are important in studying the cooperative proton tunneling mechanism, which facilitates the ring dynamics in water. The Van Hove function from INS measurements was effective in characterizing the atomic dynamics in gallium, which is a partly covalent liquid. A future study that can effectively describe the local atomic environment in gallium can reveal interesting physics behind the behaviors of covalent and partly covalent liquid systems.

REFERENCES

1. E. Mamontov and K. W. Herwig, Review of Scientific Instruments **82** (8) (2011).
2. C. A. Angell, Science **267** (5206), 1924-1935 (1995).
3. T. Iwashita, D. M. Nicholson and T. Egami, Physical Review Letters **110** (20), 205504 (2013).
4. G. Ehlers, A. A. Podlesnyak, J. L. Niedziela, E. B. Iverson and P. E. Sokol, Review of Scientific Instruments **82** (8), 085108 (2011).
5. T. Fukasawa, T. Sato, J. Watanabe, Y. Hama, W. Kunz and R. Buchner, Physical Review Letters **95** (19), 197802 (2005).
6. D. L. Abernathy, M. B. Stone, M. J. Loguillo, M. S. Lucas, O. Delaire, X. Tang, J. Y. Y. Lin and B. Fultz, Review of Scientific Instruments **83** (1), 015114 (2012).
7. T. Iwashita, B. Wu, W. R. Chen, S. Tsutsui, A. Q. R. Baron and T. Egami, Sci Adv **3** (12), e1603079 (2017).
8. K. Ward-Harvey, *Fundamental Building Materials*, 4 ed. (Universal, 2009).
9. J. P. Hansen and I. R. Mcdonald, *Theory of Simple Liquids*. (Elsevier Science, 1990).
10. J. D. Martin, Physics in Perspective **17** (1), 3-32 (2015).
11. L. D. Landau, E. M. Lifshits and L. P. Pitaevskiĭ, *Statistical physics / by L.D. Landau and E.M. Lifshitz ; translated from the Russian by J.R. Sykes and M.J. Kearsley*, 3d ed. / by E.M. Lifshitz and L.P. Pitaevskiĭ. Ed. (Pergamon Press, Oxford ;, 1980).
12. L. Onsager, Physical Review **65** (3-4), 117-149 (1944).
13. M. E. Fisher, Journal of Mathematical Physics **5** (7), 944-962 (1964).
14. D. Chandler, Annual Review of Physical Chemistry **68** (1), 19-38 (2017).
15. B. Wu, T. Iwashita and T. Egami, Physical Review E **92** (5), 052303 (2015).
16. J. D. Eshelby and R. E. Peierls, Proceedings of the Royal Society of London. Series A. Mathematical and Physical Sciences **241** (1226), 376-396 (1957).
17. V. N. Novikov, K. S. Schweizer and A. P. Sokolov, The Journal of Chemical Physics **138** (16), 164508 (2013).
18. T. Egami and Y. Shinohara, The Journal of Chemical Physics **153** (18), 180902 (2020).
19. R. Li, L. Wang, L. Li, T. Yu, H. Zhao, K. W. Chapman, Y. Wang, M. L. Rivers, P. J. Chupas, H.-k. Mao and H. Liu, Scientific Reports **7** (1), 5666 (2017).
20. A. G. Lyapin, E. L. Gromnitskaya, O. F. Yagafarov, O. V. Stal'gorova and V. V. Brazhkin, Journal of Experimental and Theoretical Physics **107** (5), 818-827 (2008).
21. N. B. Colthup, L. H. Daly and S. E. Wiberley, in *Introduction to Infrared and Raman Spectroscopy (Third Edition)*, edited by N. B. Colthup, L. H. Daly and S. E. Wiberley (Academic Press, San Diego, 1990), pp. 1-73.
22. R. Böhmer, C. Gainaru and R. Richert, Physics Reports **545** (4), 125-195 (2014).
23. F. Perakis, L. De Marco, A. Shalit, F. Tang, Z. R. Kann, T. D. Kühne, R. Torre, M. Bonn and Y. Nagata, Chemical Reviews **116** (13), 7590-7607 (2016).
24. L. Van Hove, Physical Review **95** (1), 249-262 (1954).
25. B. N. Brockhouse and N. K. Pope, Physical Review Letters **3** (6), 259-262 (1959).
26. J. P. Hansen and I. R. Mcdonald, *Theory of Simple Liquids*. (Elsevier Science, 2006).
27. B. J. Alder and T. E. Wainwright, The Journal of Chemical Physics **27** (5), 1208-1209 (1957).
28. A. Rahman, Physical Review **136** (2A), A405-A411 (1964).
29. B. Guillot, Journal of Molecular Liquids **101** (1), 219-260 (2002).
30. M. W. Mahoney and W. L. Jorgensen, The Journal of Chemical Physics **112** (20), 8910-8922 (2000).

31. W. L. Jorgensen, J. Chandrasekhar, J. D. Madura, R. W. Impey and M. L. Klein, The Journal of Chemical Physics **79** (2), 926-935 (1983).
32. J. L. F. Abascal and C. Vega, The Journal of Chemical Physics **123** (23), 234505 (2005).
33. G. Lamoureux, A. D. Mackerell and B. T. Roux, The Journal of Chemical Physics **119** (10), 5185-5197 (2003).
34. J. R. G. H. J. C. Berendsen, and T. P. Straatsma, The Journal of Physical Chemistry A **91** (24), 6269–6271 (1987).
35. W. Zhang and A. C. T. Van Duin, The Journal of Physical Chemistry B **121** (24), 6021-6032 (2017).
36. A. C. T. Van Duin, S. Dasgupta, F. Lorant and W. A. Goddard, The Journal of Physical Chemistry A **105** (41), 9396-9409 (2001).
37. J. R. D. Copley and T. J. Udovic, J Res Natl Inst Stand Technol **98** (1), 71-87 (1993).
38. J. R. Dunning, G. B. Pegram, G. A. Fink, D. P. Mitchell and E. Segrè, Physical Review **48** (8), 704-704 (1935).
39. P. Ball, Nature **452** (7185), 291-292 (2008).
40. E. Brini, C. J. Fennell, M. Fernandez-Serra, B. Hribar-Lee, M. Lukšič and K. A. Dill, Chemical Reviews **117** (19), 12385-12414 (2017).
41. L. Pauling, *The Nature of the Chemical Bond*, 3rd ed. Ed. (Cornell University Press, Ithaca, NY, 1960).
42. F. Franks, *The Physics and Physical Chemistry of Water*. (Springer US, Boston, MA, 1972).
43. J. Morgan and B. E. Warren, The Journal of Chemical Physics **6** (11), 666-673 (1938).
44. S. Katzoff, The Journal of Chemical Physics **2** (12), 841-851 (1934).
45. W. E. Thiessen and A. H. Narten, ABSTRACTS OF PAPERS OF THE AMERICAN CHEMICAL SOCIETY **181** (MAR), 82-PHYS (1981).
46. A. H. Narten, M. D. Danford and H. A. Levy, Discussions of the Faraday Society **43** (0), 97-107 (1967).
47. R. Ashcraft, Z. Wang, D. L. Abernathy, D. G. Quirinale, T. Egami and K. F. Kelton, J Chem Phys **152** (7), 074506 (2020).
48. Y. Shinohara, W. Dmowski, T. Iwashita, B. Wu, D. Ishikawa, A. Q. R. Baron and T. Egami, Phys Rev E **98** (2-1), 022604 (2018).
49. Shirane, S. M. Shapiro and J. M. Tranquada, *Neutron scattering with a triple-axis spectrometer*. (Cambridge University Press, Cambridge, England, 2002).
50. A. K. Soper and C. J. Benmore, Phys Rev Lett **101** (6), 065502 (2008).
51. A. K. Soper, ISRN Physical Chemistry **2013**, 279463 (2013).
52. J. Mayers, Nuclear Instruments and Methods in Physics Research **221** (3), 609-618 (1984).
53. J. Taylor, Arnold, O., Bilheaux, J., Buts, A., Campbell, S., Doucet, M., ... & Zikovsky, J. . , Bulletin of the American Physical Society **57** (2012).
54. O. Arnold, J. C. Bilheux, J. M. Borreguero, A. Buts, S. I. Campbell, L. Chapon, M. Doucet, N. Draper, R. Ferraz Leal, M. A. Gigg, V. E. Lynch, A. Markvardsen, D. J. Mikkelson, R. L. Mikkelson, R. Miller, K. Palmen, P. Parker, G. Passos, T. G. Perring, P. F. Peterson, S. Ren, M. A. Reuter, A. T. Savici, J. W. Taylor, R. J. Taylor, R. Tolchenov, W. Zhou and J. Zikovsky, Nuclear Instruments and Methods in Physics Research Section A: Accelerators, Spectrometers, Detectors and Associated Equipment **764**, 156-166 (2014).
55. B. Wu, T. Iwashita and T. Egami, Phys Rev Lett **120** (13), 135502 (2018).
56. Y. Shinohara, W. Dmowski, T. Iwashita, D. Ishikawa, A. Q. R. Baron and T. Egami, Physical Review E **102** (3), 032604 (2020).
57. E. Lorch, Journal of Physics C: Solid State Physics **2** (2), 229-237 (1969).

58. G. S. U. Heugen, E. Bründermann, M. Heyden, X. Yu, D. M. Leitner, and M. Havenith, PNAS **103** (33), 12301-12306 (2006).
59. W. J. Ellison, K. Lamkaouchi and J. M. Moreau, Journal of molecular liquids **68** (2-3), 171-279 (1996).
60. P. Debye, (John Wiley & Sons, Ltd, New York, 1929), Vol. 48, pp. 1036-1037.
61. I. Ohmine, The Journal of Physical Chemistry **99** (18), 6767-6776 (1995).
62. B. Bagchi and A. Chandra, Physical Review Letters **64** (4), 455-458 (1990).
63. N. Agmon, The Journal of Physical Chemistry **100** (3), 1072-1080 (1996).
64. C. Ro/nne, L. Thrane, P.-O. Åstrand, A. Wallqvist, K. V. Mikkelsen and S. R. R. Keiding, The Journal of Chemical Physics **107** (14), 5319-5331 (1997).
65. A. S. R. K. C. Rønne, Journal of Molecular Liquids **101** (1-3), 199-218 (2002).
66. K. B. J. Barthel, R. Buchner, and H. Hetzenauer, Chem. Phys. Lett. **165**, 369 (1990).
67. J. S. Hansen, A. Kisliuk, A. P. Sokolov and C. Gainaru, Phys Rev Lett **116** (23), 237601 (2016).
68. R. A Buchner, A Barthel, J., A Stauber, J., J Chemical Physics Letters **306**, 57 (1999).
69. R. B. U. Kaatze, R. Pottel, Journal of Non-Crystalline Solids **305** (1–3), 19-28 (2002).
70. P. Ben Ishai, S. R. Tripathi, K. Kawase, A. Puzenko and Y. Feldman, Phys Chem Chem Phys **17** (23), 15428-15434 (2015).
71. F. Sciortino, A. Geiger and H. E. Stanley, Nature **354** (6350), 218-221 (1991).
72. F. Sciortino, A. Geiger and H. E. Stanley, The Journal of Chemical Physics **96** (5), 3857-3865 (1992).
73. T. Sato and R. Buchner, The Journal of Chemical Physics **119** (20), 10789-10800 (2003).
74. P. Petong, R. Pottel and U. Kaatze, The Journal of Physical Chemistry A **103** (31), 6114-6121 (1999).
75. I. Popov, P. B. Ishai, A. Khamzin and Y. Feldman, Phys Chem Chem Phys **18** (20), 13941-13953 (2016).
76. A. Arbe, P. Malo de Molina, F. Alvarez, B. Frick and J. Colmenero, Phys Rev Lett **117** (18), 185501 (2016).
77. U. Dahlborg, W. Gudowski and M. Davidovic, Journal of Physics: Condensed Matter **1** (35), 6173-6179 (1989).
78. T. E. Mason, D. Abernathy, I. Anderson, J. Ankner, T. Egami, G. Ehlers, A. Ekkebus, G. Granroth, M. Hagen, K. Herwig, J. Hodges, C. Hoffmann, C. Horak, L. Horton, F. Klose, J. Larese, A. Mesecar, D. Myles, J. Neuefeind, M. Ohl, C. Tulk, X. L. Wang and J. Zhao, Physica B: Condensed Matter **385-386**, 955-960 (2006).
79. T. E. Faber and J. M. Ziman, The Philosophical Magazine: A Journal of Theoretical Experimental and Applied Physics **11** (109), 153-173 (1965).
80. A. H. Narten, W. E. Thiessen and L. Blum, Science **217** (4564), 1033-1034 (1982).
81. C. Zhang and G. Galli, J Chem Phys **141** (8), 084504 (2014).
82. C. Zhang, F. Gygi and G. Galli, The Journal of Physical Chemistry Letters **4** (15), 2477-2481 (2013).
83. J. A. Pople, Proceedings of the Royal Society of London. Series A. Mathematical and Physical Sciences **205** (1081), 163-178 (1951).
84. J. D. Bernal and R. H. Fowler, The Journal of chemical physics **1** (8), 515-548 (1933).
85. D. Marx, A. Chandra and M. E. Tuckerman, Chemical Reviews **110** (4), 2174-2216 (2010).
86. C. J. Burnham, S. S. Xantheas, M. A. Miller, B. E. Applegate and R. E. Miller, The Journal of Chemical Physics **117** (3), 1109-1122 (2002).
87. J. Liu, X. He, J. Z. H. Zhang and L. W. Qi, Chem Sci **9** (8), 2065-2073 (2018).

88. J. Gelman-Constantin, M. A. Carignano, I. Szleifer, E. J. Marceca and H. R. Corti, J Chem Phys **133** (2), 024506 (2010).
89. J. Liu, X. He and J. Z. H. Zhang, Phys Chem Chem Phys **19** (19), 11931-11936 (2017).
90. S. Plimpton, J. Comput. Phys. **117**, 1-19 (1995).
91. H. C. Andersen, JOURNAL OF COMPUTATIONAL PHYSICS **52**, 24-34 (1982).
92. G. C. J.-P. Ryckaert, and and H. J. C. Berendsen, JOURNAL OF COMPUTATIONAL. PHYSICS **23**, 321-341 (1977).
93. A. Luzar and D. Chandler, Nature **379** (6560), 55-57 (1996).
94. S. Le Roux and P. Jund, Computational Materials Science **49** (1), 70-83 (2010).
95. T. Egami and Y. Shinohara, Molecular Physics **117** (22), 3227-3231 (2019).
96. X. G. Gong, G. L. Chiarotti, M. Parrinello and E. Tosatti, Physical Review B **43** (17), 14277-14280 (1991).
97. R. Poloni, S. De Panfilis, A. Di Cicco, G. Pratesi, E. Principi, A. Trapananti and A. Filipponi, Physical Review B **71** (18), 184111 (2005).
98. X. G. Gong, G. L. Chiarotti, M. Parrinello and E. Tosatti, Europhysics Letters (EPL) **21** (4), 469-475 (1993).
99. L. R. K. R.T. Azuah, Y. Qiu, P.L. Tregenna-Piggott, C.M. Brown, J.R. Copley, R.M. Dimeo, J Res Natl Inst Stand Technol **114**, 341-358 (2009).
100. A. H. Narten, The Journal of Chemical Physics **56** (3), 1185-1189 (1972).
101. T. Egami, K. Maeda and V. Vitek, PHILOSOPHICAL MAGAZINE A-PHYSICS OF CONDENSED MATTER STRUCTURE DEFECTS AND MECHANICAL PROPERTIES **41** (6), 883-901 (1980).
102. O. H. Nielsen and R. M. Martin, Physical Review Letters **50** (9), 697-700 (1983).
103. G. Kresse and J. Hafner, Physical Review B **47** (1), 558-561 (1993).
104. J. Yang, J. S. Tse and T. Iitaka, The Journal of Chemical Physics **135** (4), 044507 (2011).
105. M. I. Baskes, Physical Review B **46** (5), 2727-2742 (1992).
106. A. M. Saitta, F. Saija and P. V. Giaquinta, Phys Rev Lett **108** (20), 207801 (2012).

APPENDIX

APPENDIX A: Determination of the Dielectric Spectrum of Water

The polarization of a material is described by the polarization vector $\boldsymbol{P}(r)$, which is defined as the polarization per unit volume at r. To satisfy the Gauss's law, bound charge density is introduced, so that,

$$\nabla \boldsymbol{P} = -\rho_b.$$

Therefore, Gauss's law may be written as,

$$\nabla E = \frac{1}{\varepsilon_0}\left(\rho_f + \rho_b\right).$$

This leads to a new field called electric displacement,

$$\boldsymbol{D} = \varepsilon_0 \boldsymbol{E} + \boldsymbol{P},$$

which allows us to write the free charge density as the gradient of electric displacement,

$$\nabla \boldsymbol{D} = \rho_f.$$

In the case of a linear, homogeneous, isotropic, and non-dispersive dielectric medium, the polarization is proportional to the electric field E, and aligned in the same direction, as given by

$$\boldsymbol{P} = \varepsilon_0 \chi \boldsymbol{E},$$

where ε_0 is the dielectric permittivity in vacuum, and χ is the electrical susceptibility of the medium. For a time-dependent electric field in a non-dispersive medium, taking account of the causality of the field, this equation generalizes to

$$\boldsymbol{P}(t) = \varepsilon_0 \int_{-\infty}^{t} \chi_e(t - t')\boldsymbol{E}(t')dt',$$

where $\chi_e(t)$ is the time-dependent susceptibility. Assuming the conditions of linear response theory are applicable, it is better to describe this relation in the frequency space due to the convolution theorem:

$$\boldsymbol{P}(\omega) = \varepsilon_0 \, \chi(\omega) \, \boldsymbol{E}(\omega),$$

where $\chi(\omega)$ is the complex susceptibility. For real materials, the response of the susceptibility or the dielectric constant depends on the frequency of the applied electric field. Due to causality, the polarization response is not instantaneous. Therefore, the dielectric constant is treated as a complex function of frequency. At low frequencies of an applied electric field, the polarization of the material will be in-phase, but as the frequency is increased, the polarization starts to lag behind the field. This would lead to energy dissipation due to the interactions between the water dipoles and the field. The complex dielectric constant $\varepsilon(\omega)$ is given as

$$\varepsilon(\omega) = \varepsilon'(\omega) + i \, \varepsilon''(\omega),$$

where the real part represents the dielectric constant and the imaginary part, the dielectric loss factor of the system. The dielectric dispersion relation of the material is estimated from the frequency dependent behavior of the susceptibility, $\chi(\omega)$. The dielectric loss factor can be parameterized in terms of the corresponding loss tangent *tan* δ, where δ is the loss angle between the real part (represents the permittivity component quantifying the stored energy in the material) and the imaginary part (describes the part of the electric energy that is lost in the process) of the complex dielectric constant. The dielectric loss can be estimated by applying an oscillating electric field to the system and modelling the polarization response.

In the present study, we use classical molecular dynamics simulations using the SPC/E model to calculate the dielectric loss spectrum of heavy water.

A combination of Coulombic and Lennard-Jones potentials are used in describing the interactions in water from molecular dynamics simulations. The repulsion between the oxygen atoms are modeled using Lennard-Jones equation, and the pair-wise interactions between charged sites from Coulomb's law, following Ewald summation. The most widely used models of water are rigid, where the angle (H-O-H) between the covalent bonds are kept constant. The SPC/E model describes many of the bulk properties of water accurately such as diffusion constant and density. A water molecule possesses a net dipole moment (experimental - 2.95 D, SPC/E - 2.35 D). In a system of polar water molecules, the application of an external electric field ($\boldsymbol{E}$) results in a torque ($\boldsymbol{\tau}$) on the molecule to align it towards the direction of the field. The torque is given by

$$\boldsymbol{\tau} = \boldsymbol{\mu} \times \boldsymbol{E}.$$

An oscillating electric field was applied to determine the frequency response of heavy water. The sinusoidal electric field is of the form,

$$\boldsymbol{E}(t) = E_0 \cos \omega t \, \hat{\boldsymbol{z}}.$$

The polarization density of the system is analyzed as the response of the system and determined the phase-shift, δ. The classical MD simulations were performed using the Large-Scale Atomic/Molecular Massively Parallel Simulator (LAMMPS). The O-H bonds and the H-O-H angle were kept rigid using the 'shake' command. The temperature and pressure were kept at ambient values. The command 'efield' is used to simulate the

oscillating electric field, after equilibrating the system at ambient temperature for 2 ns. Periodic boundary conditions were imposed in all directions. A cutoff distance of 10 Å was used for the electrostatic and non-electrostatic interactions. The system consisted of 216 water molecules with the electric field amplitude set at 0.1 $V/\text{Å}$. It was previously shown from first principle calculations that 0.2 $V/\text{Å}$ should be enforced so as to not reach the dissociation threshold.[106] The frequency response across a wide frequency range were probed to determine the dielectric spectrum of water. The hysteresis curve can be found for the field of $\nu = 10$ GHz in **Figure 6.1**. The polarization lags behind the oscillating electric field due to the causal nature of the interaction, which is shown in **Figure 6.2**. The resulting polarization is fitted as a function of time with a sinusoidal function of the form $A(t) = A_0 \cos(2\pi\nu t - \delta)$, where the phase-shift (δ) describes the dielectric loss in the system. The dielectric loss spectrum is plotted in **Figure 6.3.** The fitting procedure is shown in **Figure 6.4** δ is used to estimate the loss tangent, which is plotted as the function of the frequency of the external electric field.

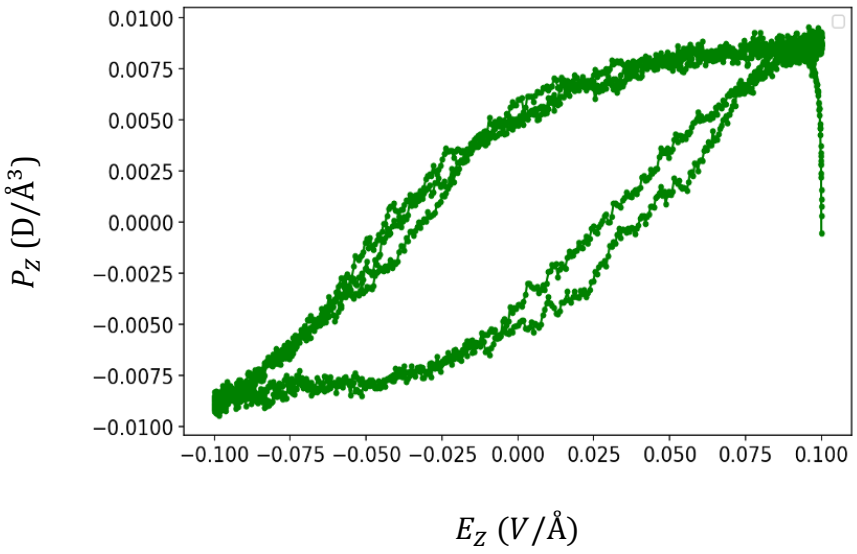

Figure 6.1 The hysteresis loop for $\boldsymbol{\nu}$=10 GHz, which describes the dielectric loss in D2O from classical MD simulations using SPC/E model.

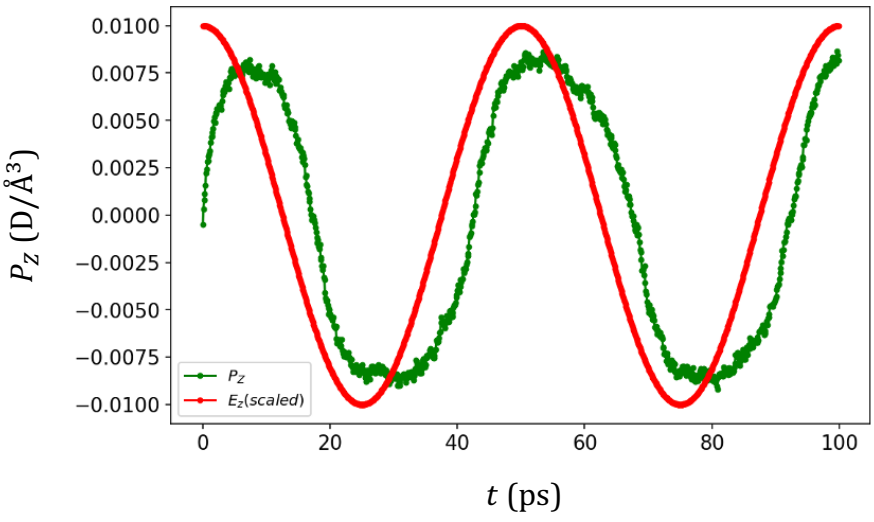

Figure 6.2 The polarization lags behind the electric field in MD simulations using SPC/E model for $\boldsymbol{\nu}$=20 GHz. The magnitude of electric field is scaled for a better comparison.

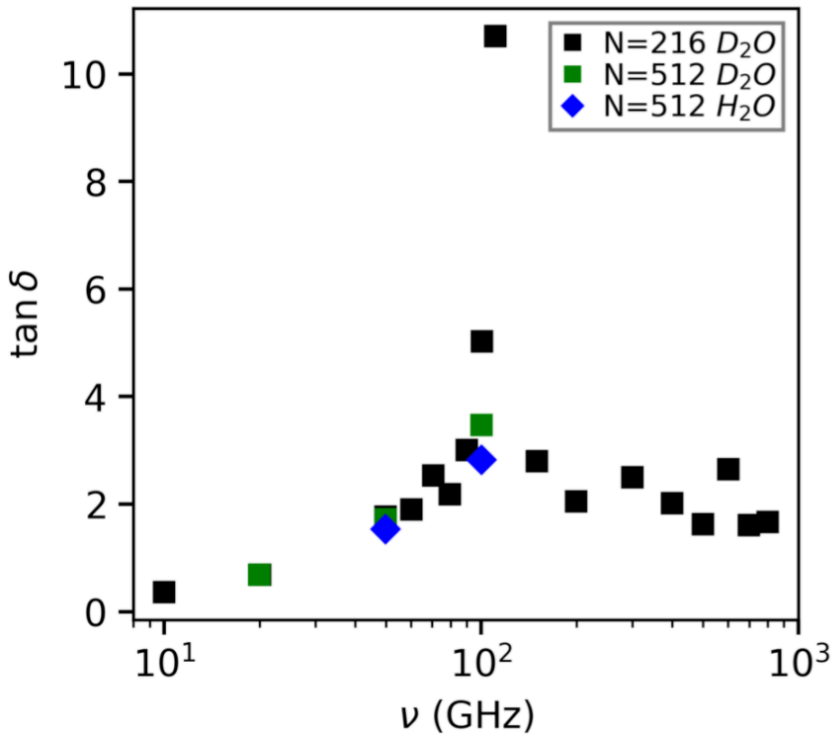

Figure 6.3 The loss tangent is shown for water and heavy water.

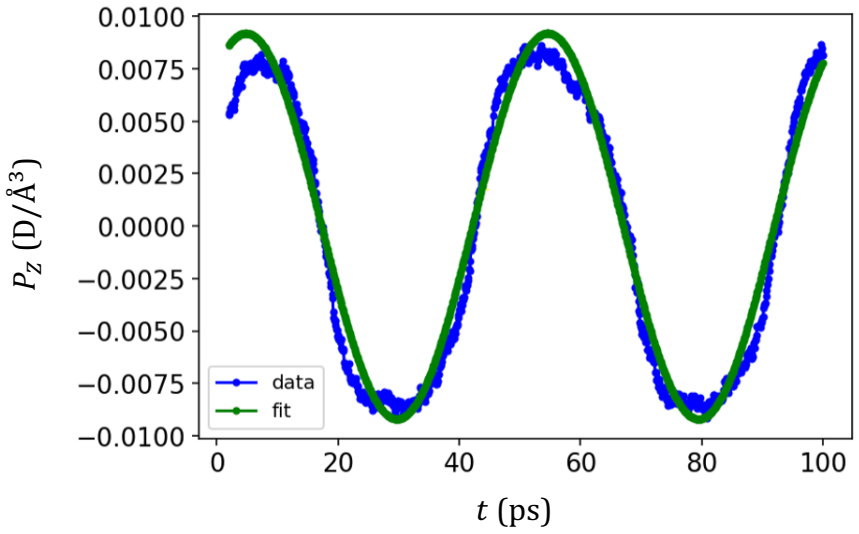

Figure 6.4 The polarization fitted using a sinusoidal function with a phase-shift $\boldsymbol{\delta}$.

APPENDIX B: The Resolution function from Neutron Spectrometers

The resolution functions provide the time-ranges available for a particular parameter setting in a neutron scattering instrument. The resolution function is de-convoluted from the total dynamic structure factor to provide the corrected dynamic structure factor. The resolution function from the BASIS and CNCS spectrometers can be seen in **Figure 6.5** and **Figure 6.6**.

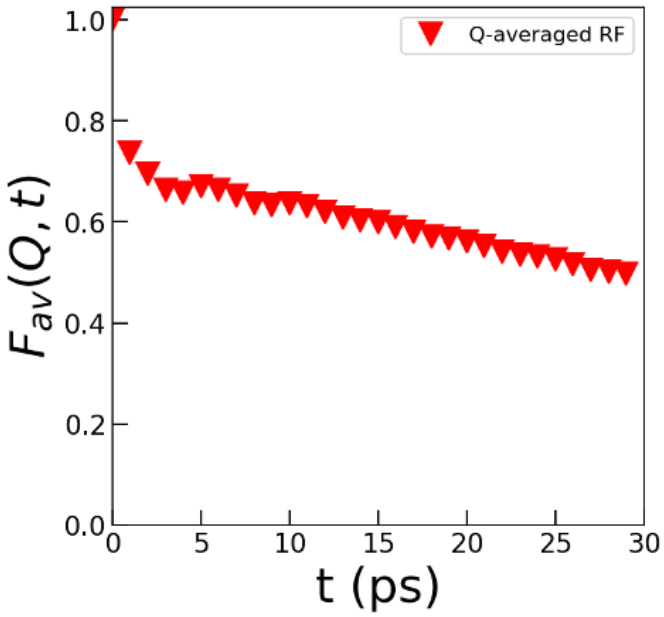

Figure 6.5 Resolution function, which determines the dynamic range of the instrument, from BASIS, SNS.

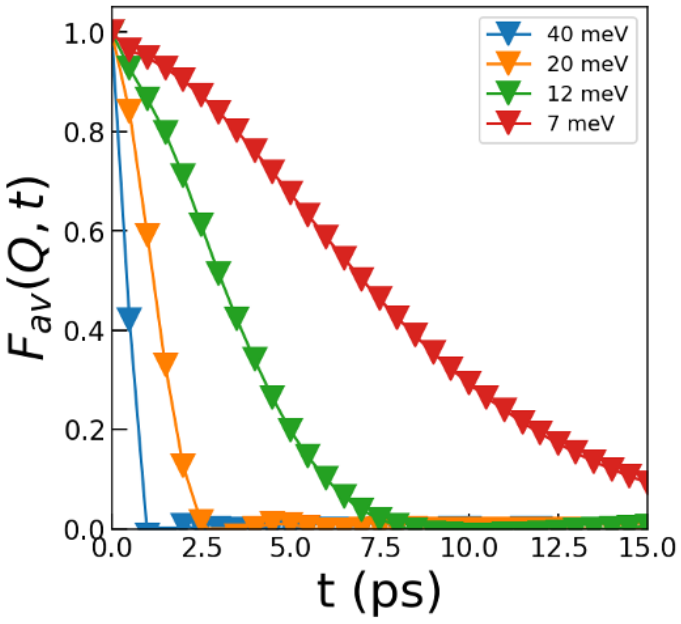

Figure 6.6 Resolution function, which determines the dynamic range of the instrument, from CNCS, SNS for a few incident energy values.

APPENDIX C: Codes for data analysis and simulations

1. Python code to calculate the Van Hove function from a LAMMPS output file (.dump)

```
import numpy as np
import matplotlib.pyplot as plt
import pandas as pd
import pylab as pl
from matplotlib.ticker import FormatStrFormatter
from matplotlib import rcParams
import matplotlib as mpl
from matplotlib import rc
# activate latex text rendering
rc('text', usetex=False)

# Helper function
def Nint(a):
    if a>=0.0:
        ans=int(a+0.5)
    else:
        ans=int(a-0.5)
    return ans

# Function for calculating VHF from LAMMPS dump files given number of s
napshots
# (f) and distance (R).
# The dump file ('VHF_OO_python_N1000_300K.dump') has 20 time-frames
# (0, 0.1, 0.2, ... 2.0 ps).

def VHF(filename, f=101, maxR=8):
    # Number of particles
    particles = np.int(pd.read_csv(filename, header=None).iloc[3][0])

    deltaR=0.1 # 0.1 Ang?
    deltaT=0.1 # 0.1 ps (This is controlled by the Lammps output dump r
ate)

    numR=np.int(maxR/deltaR)
    distance=np.arange(0, maxR, deltaR)

    x=np.zeros((f, particles)) # Initializing the zero arrays
    y=np.zeros((f, particles))
    z=np.zeros((f, particles))

    xlo = np.float(pd.read_csv(filename, header=None).iloc[5][0]
```

```
                                                    .split()[0])
xhi = np.float(pd.read_csv(filename, header=None).iloc[5][0]

                                                    .split()[1])
ylo = np.float(pd.read_csv(filename, header=None).iloc[6][0]

                                                    .split()[0])
yhi = np.float(pd.read_csv(filename, header=None).iloc[6][0]

                                                    .split()[1])
zlo = np.float(pd.read_csv(filename, header=None).iloc[7][0]

                                                    .split()[0])
zhi = np.float(pd.read_csv(filename, header=None).iloc[7][0]

                                                    .split()[1])

lx=xhi-xlo # Length of the sides of the simulation box
ly=yhi-ylo
lz=zhi-zlo

vol=lx*ly*lz # Volume of the NVT simulation box

period_skip=np.arange(8, 8+(particles+9)*f, (particles+9))

for i in range(f):
    pos_oo = pd.read_csv(filename, skiprows=period_skip[i]
                         , header=None, sep=None).iloc[1:]
                                                   .iloc[:particles]

    x[i]=np.array(pos_oo[2], dtype=float)
    y[i]=np.array(pos_oo[3], dtype=float)
    z[i]=np.array(pos_oo[4], dtype=float)

# VHF array initialization
VHF=np.zeros((f, numR))
VHF_norm=np.zeros((f, numR))

# Un-normalized VHF calculation
for i in range(f):
    for m in range(particles):
        for l in range(particles):
            dmy_rx=x[0,m]-x[i,l]
            dmy_ry=y[0,m]-y[i,l]
            dmy_rz=z[0,m]-z[i,l]

            dmy_rx-=Nint(dmy_rx/lx)*lx
            dmy_ry-=Nint(dmy_ry/ly)*ly
            dmy_rz-=Nint(dmy_rz/lz)*lz
```

```
                r=np.sqrt(dmy_rx**2+dmy_ry**2+dmy_rz**2)
                if r<maxR and m!=l:                 # For total VHF,
                    VHF[i][int(r*(1.0/deltaR))]+=1  # remove "m!=l"
                                                    # for VHF estimatio
n
    # Normalized VHF
    for i in range(f):
        for l in range(numR):
            coef = 1/np.square(l*deltaR)/(4*np.pi)/deltaR/particles
                                                          *vol/particles
            VHF_norm[i][l] = VHF[i][l]*coef

    return VHF_norm

# Visualization of the Van Hove function

time = np.linspace(0.0, 10.0, 101)

plt.figure(figsize=(12,5))

plt.subplot(121)
rv, tv = np.meshgrid(distance,time)
plt.pcolor(rv, tv, VHF_oo, cmap=plt.cm.get_cmap('inferno'), vmin=0.

                                                          , vmax=4.)
plt.colorbar()
plt.title("VHF O-O", fontsize=15, y=1.02)
plt.xlabel("r ($\AA$)", fontsize=15)
plt.ylabel("t (ps)", fontsize=15)

plt.subplot(122)
rv, tv = np.meshgrid(dist,time)
plt.pcolor(rv, tv, VHF_dd, cmap=plt.cm.get_cmap('inferno'), vmin=0.

                                                          , vmax=4.)
plt.colorbar()
plt.title("VHF D-D", fontsize=15, y=1.02)
plt.xlabel("r ($\AA$)", fontsize=15)
plt.ylabel("t (ps)", fontsize=15)

plt.tight_layout(pad=.3, w_pad=2.8, h_pad=2.)

plt.show()
```

2. **Python code to determine the number of rings from SPC/E simulation of water.**

```
%matplotlib inline
import numpy as np
import matplotlib.pyplot as plt
import pandas as pd
from scipy.optimize import curve_fit
```

Estimating the coordination number of the system (Water) as a fuction of cut-off distance between molecules.

```
# Calculating the adjacency matrix from LAMMPS trajectory file of water

# Number of vertices
V = np.int(pd.read_csv('spce_wat_Ox_280K_dt100fs_11frames.dump',
                       header=None).iloc[0][0])

# Positions of atoms
pos = pd.read_csv('spce_wat_Ox_280K_dt100fs_11frames.dump',
                  header=None, skiprows=2, delimiter=" ").iloc[:V]
x=np.array(pos[1], dtype=float)
y=np.array(pos[2], dtype=float)
z=np.array(pos[3], dtype=float)

# Distance calculation
dist=np.full((V,V),0.0)
for m in range(V):
    for l in range(V):
        dist[m][l]=(((x[m]-x[l])**2+(y[m]-y[l])**2+(z[m]-z[l])**2)**0.5
)

# main
# O-O bond length approximate value

with open("coord_vs_bondlen_spce_285K”, "w") as outfile:
    bond_dist=np.arange(2.7, 5, 0.1)
    for i in bond_dist:
        # Adjacency matrix creation
        adj=dist<=i
        adj=adj.astype(int)
        np.fill_diagonal(adj, 0)

        outstring = ''
        outstring += str(i) + ','
        outstring += str(np.mean(np.sum(adj, axis=0))) + '\n'
        outfile.write(outstring)
```

Coordination number visualization

```
coord_spce_300k=pd.read_csv('coord_vs_bondlen_spce_300k', header=None)
plt.plot(coord_spce_300k[0],   coord_spce_300k[1],'bd-', label='300K')

plt.title("Coordination Vs Cut-off (SPC/E)", fontsize=20, y=1.04)
plt.xlabel("Cut-off distance", fontsize=20, y=1.0)
plt.ylabel("Coordination \nNumber", fontsize=20)
plt.grid(True)
plt.tick_params(direction='in', length=8, width=1., labelsize=14)
plt.ticklabel_format(style='sci', scilimits=(-3,3), useMathText=True)
plt.legend(loc='best', fontsize=15, frameon=False)
plt.show()
```

Code to count the number of n-cycles in a graph using Depth First Search (DFS) algorithm

```
# Utility functions

def DepthFirstSearch(graph, visited, n, vertex, start_vertex
                     , count, path):

    visited[vertex] = True
    if n == 0:
        visited[vertex] = False
        if graph[vertex][start_vertex] == 1:
            count = count + 1
            paths.append(path)
            return count
        else:
            return count
    for i in range(V):
        if visited[i] == False and graph[vertex][i] == 1:
            next_path = path[:]
            next_path.append(i)
            count = DepthFirstSearch(graph, visited,
                                     n-1, i,
                                     start_vertex,
                                     count,
                                     next_path)
    visited[vertex] = False
    return count

def CountRings( graph, n):
    visited = [False] * V
    count = 0
    for i in range(V-(n-1)):
```

```
        count = DepthFirstSearch(graph, visited,
                                 n-1, i, i,
                                 count,[i])
        visited[i] = True
    return int(count/2)

def Nint(a):
    if a>=0.0:
        ans=int(a+0.5)
    else:
        ans=int(a-0.5)
    return ans

# Calculating the adjacency matrix from LAMMPS trajectory file of water

# Number of vertices
V = np.int  (pd.read_csv('spce_wat_OO_300K_atom_heavy.dump',
                         header=None).iloc[3][0])

# Total number of time-frames
f=5

distance_check_300k_oo=[]
adjacency_check_300k_oo=[]
n_paths_300k=[]
n_cycles_300k=[]

xlo = np.float(pd.read_csv('spce_wat_OO_300K_atom_heavy.dump',
                           header=None).iloc[5][0].split()[0])
xhi = np.float(pd.read_csv('spce_wat_OO_300K_atom_heavy.dump',
                           header=None).iloc[5][0].split()[1])
ylo = np.float(pd.read_csv('spce_wat_OO_300K_atom_heavy.dump',
                           header=None).iloc[6][0].split()[0])
yhi = np.float(pd.read_csv('spce_wat_OO_300K_atom_heavy.dump',
                           header=None).iloc[6][0].split()[1])
zlo = np.float(pd.read_csv('spce_wat_OO_300K_atom_heavy.dump',
                           header=None).iloc[7][0].split()[0])
zhi = np.float(pd.read_csv('spce_wat_OO_300K_atom_heavy.dump',
                           header=None).iloc[7][0].split()[1])

lx=xhi-xlo
ly=yhi-ylo
lz=zhi-zlo
vol=lx*ly*lz
period_skip=np.arange(8, 8+1009*f, 1009) # V = 1000 for O-O

for i in range(len(period_skip)):
    pos = pd.read_csv('spce_wat_OO_300K_atom_heavy.dump',
```

```
                    skiprows=period_skip[i],
                    header=None, delimiter=" ")
                              .iloc[1:].iloc[:V]

    x=np.array(pos[2], dtype=float)*lx
    y=np.array(pos[3], dtype=float)*ly
    z=np.array(pos[4], dtype=float)*lz

    # Distance calculation
    dist=np.full((V,V),0.0)
    for m in range(V):
        for l in range(V):
            dmy_rx=x[m]-x[l]
            dmy_ry=y[m]-y[l]
            dmy_rz=z[m]-z[l]

            dmy_rx-=Nint(dmy_rx/lx)*lx
            dmy_ry-=Nint(dmy_ry/ly)*ly
            dmy_rz-=Nint(dmy_rz/lz)*lz

            dist[m][l]=np.sqrt(dmy_rx**2+dmy_ry**2+dmy_rz**2)

    distance_check_300k_oo.append(dist)


    # O-O bond length approximate value
    bond_dist=3.4

    # Adjacency matrix creation
    adj=dist<bond_dist
    adj=adj.astype(int)
    adjacency_check_300k_oo.append(adj)
    np.fill_diagonal(adj, 0) # Filling 0s for the diagonal terms

    nmax=10 # Max sides of the polygon
    nmin=3  # Min sides of the polygon
    ndiff=nmax-nmin

    for i in np.arange(nmin, nmax, 1):
        paths=[]
        n_cycles_300k.append([i, CountRings(adj, i)])
    for i in np.arange(nmin, nmax, 1):
        paths=[]
        CountRings(adj, i)
        n_paths_300k.append([i, paths])

distance_check_300k_oo = np.array(distance_check_300k_oo)
adjacency_check_300k_oo = np.array(adjacency_check_300k_oo)
```

```
n_cycles_300k=np.array(n_cycles_300k)
n_paths_300k=np.array(n_paths_300k, dtype=object)
n_cycles_300k=n_cycles_300k.reshape(f, ndiff, 2)
n_paths_300k=n_paths_300k.reshape(f, ndiff, 2)

#-----------------------------------------------
n_cycles_300K_spce=n_cycles_300k
n_paths_300K_spce=n_paths_300k
```

VITA

Yadu Sarathchandran was born and raised in Kerala, India. Developed a keen interest in science from a small age, which lead him to pursue an undergraduate degree in physics at the Indian Institute of Science Education and Research, Thiruvananthapuram. Joined the University of Tennessee in the Fall of 2015 to pursue a Ph.D. in Physics. In his spare time, he enjoys watching movies, reading books, and playing Soccer. He also enjoys learning more about the history of the pale blue dot and the philosophy of living a full life.